



Università degli Studi di Roma Tre
Scuola Dottorale in Scienze Matematiche e Fisiche

Dottorato di ricerca in Fisica - XXV CICLO

**$\Lambda(1405)$ measurement through the decay to $\Sigma^0\pi^0$, resulting
from K^- meson absorption on ^4He and ^{12}C , with the KLOE
detector**

Thesis submitted to obtain the degree of

"Dottore di ricerca" - Doctor Philosophiae

PhD in Physics

Kristian Piscicchia

Tutors:

Dott.ssa Catalina Curceanu, Laboratori Nazionali di Frascati INFN
Prof. Filippo Ceradini, Università degli Studi di Roma Tre

A mia madre e mio padre

*anche nella piu' violenta bufera
continuando a tenerci per mano
non perderemo le orme dei passi percorsi.*

Contents

1	Theoretical and experimental status of the $\Lambda(1405)$ study	7
1.1	Introduction	7
1.2	Experimental results on the $\Lambda(1405)$ lineshape compared with theoretical calculations	10
1.3	K^- nuclear interaction studies in emulsion and Helium bubble chamber experiments	16
1.3.1	K^- nuclear interactions at rest in emulsion experiments . . .	16
1.3.2	Bubble chamber studies of K^- interactions at rest in helium	19
1.4	Summary	23
2	The KLOE detector at the DAΦNE collider	25
2.1	Introduction	25
2.2	The DAΦNE collider	25
2.3	The KLOE detector	27
2.3.1	The KLOE drift chamber	27
2.3.2	The KLOE calorimeter	29
2.4	Data reconstruction	33
2.4.1	Cluster reconstruction	33
2.4.2	Track reconstruction	34
2.4.3	Track to cluster association	35
3	The events selection	36
3.1	Introduction	36
3.2	The data sample	36
3.3	$\Lambda(1116)$ identification	37
3.4	Spatial distribution of the selected events	44

3.5	Extra p tracks and interaction vertex extrapolation	45
3.6	Photons cluster selection	48
3.7	Photons cluster identification	50
3.8	Cluster splitting and background rejection	51
3.9	$m_{\Lambda\gamma_3}$ invariant mass	53
4	Study of K^- absorption in the KLOE drift chamber entrance wall	56
4.1	Introduction	56
4.2	Composition of the drift chamber entrance wall	57
4.3	MC simulation of $\Sigma^0\pi^0$ production in the DC entrance wall	58
4.4	Resolution in ρ_Λ and p_Λ determination	60
4.5	Λ decay vertex selection	61
4.6	Missing mass distribution	64
4.7	$\Sigma^0\pi^0$ invariant mass and momentum distributions	68
4.8	Comparison of the $p_{\Sigma^0\pi^0}$ and T_{π^0} distributions with emulsion experiments	72
4.9	Analysis of K^- absorptions in pure Carbon target	77
4.10	Analysis of the background: $\Sigma(1385)$ and internal conversion events	80
4.10.1	γ_3 clusters characterisation	81
4.10.2	Study of the Λ momentum distribution	82
4.10.3	Estimate of the $\Sigma(1385)$ and internal conversion contribution to the final selected sample	85
5	Study of K^- absorption in the gas filling the KLOE drift chamber	88
5.1	Introduction	88
5.2	Composition of the gas filling the KLOE DC	88
5.3	MC simulation of $\Sigma^0\pi^0$ production in the DC gas	90
5.4	Resolution in ρ_Λ and p_Λ determination	92
5.5	$\Sigma^0\pi^0$ invariant mass and momentum distributions	93
5.6	Comparison of the observed spectra with Helium bubble chamber experiments	96
5.7	Search for an extra-track coming from the K^- interaction point . .	100
5.8	Analysis of the background: $\Sigma(1385)$ and internal conversion events	104
5.8.1	γ_3 clusters characterization	104

5.8.2	Study of the Λ momentum distribution.	105
5.8.3	Estimate of the $\Lambda\pi^0$ contribution to the final selected sample.	107
5.9	$m_{\Sigma^0\pi^0}$ spectrum obtained with mass hypothesis	108
6	Fit of the observed distributions	112
6.1	Introduction	112
6.2	The fitting algorithm	113
6.3	Single resonant pole component fits to the DC entrance wall events	114
6.4	Fits to events corresponding to K^- absorptions in the DC gas . . .	122

Introduction

This work is dealing with the study of the low-energy interactions of the negatively charged kaons with light nuclei. Such type of physics, extremely important for the understanding of the non-perturbative QCD in the strangeness sector, has important consequences, going from the particle and nuclear physics to astrophysics. We investigated the $\Sigma^0\pi^0$ channel, generated by K^- absorptions on bound protons in ${}^4\text{He}$ and ${}^{12}\text{C}$. $\Sigma^0\pi^0$ is the privileged, but still poorly explored, channel to explore the yet unsolved structure of the $\Lambda(1405)$ resonance, since it is free from the dominant $\Sigma(1385)$ background. The $\Lambda(1405)$ plays a central role in various aspects of hadron and nuclear strangeness physics. Due to its intimate connection with the strongly attractive $\bar{K}N$ channel, this state can be considered as the "key ingredient" for understanding the few body-antikaon systems and their possible exotic properties predicted in some theories, but non existent in others.

The quest for low-energy K^- hadronic interactions with KLOE detector at the DAΦNE collider is based on few, but essential features:

- the DAΦNE collider is a unique source of low-momentum monochromatic kaons produced in the ϕ decay almost at rest,
- the large acceptance of the KLOE detector, the excellent performances in charged particles detection, the high efficiency and resolution of the KLOE calorimeter for photons, render KLOE an ideal apparatus for the low-energy kaon-nucleon/nuclei research,
- dedicated studies were performed using the standard KLOE Monte Carlo simulation, GEANFI, for the conditions of the 2004-2005 runs, to which data presented in this work belong. A fraction of stopped K^- in the KLOE drift chamber entrance wall (mainly Carbon) of 2% was found and of 0.1% in the

drift chamber gas (mainly Helium). Apart this, there are kaons interacting in flight giving rise to the $\Sigma^0\pi^0$ final state.

The work is organized as follows. In Chapter 1 the scientific case of the $\Lambda(1405)$ is presented; the status of the theoretical and experimental search is outlined, with particular care to its implications in the strangeness nuclear physics. Chapter 2 is devoted to a brief description of the $DA\Phi NE$ collider and the KLOE detector. The details of particle identification and of the events selection procedure are given in Chapter 3. The core of the performed analysis of K^- absorptions in Carbon and Helium are reported in Chapters 4 and 5, respectively, with a similar structure to highlight the symmetries of the obtained results for the two target nuclei. In Chapter 6 the outcome of the performed fits will enable the comparison of the measured spectra with theoretical predictions and previous results from similar experimental conditions measurements.

Thanks to a careful comparative study of the relevant kinematical variables spectra with bubble chamber and emulsion experiments, a clear understanding of the different kinematical regimes contributing to the observed events will be achieved. The in flight K^- nuclear absorptions, accessing a higher invariant mass region above the threshold imposed by the proton binding energy, will be characterized in this study for the first time, shedding new light on the $\Lambda(1405)$ behaviour in nuclear environment.

A final Chapter 7, dedicated to conclusions, ends this work, showing how the KLOE detector at $DA\Phi NE$ can perform, with enormous success, first-class studies in the field of low energy QCD in the strangeness sector.

Chapter 1

Theoretical and experimental status of the $\Lambda(1405)$ study

1.1 Introduction

The $\Lambda(1405)$ is generally accepted to be a spin $1/2$, isospin $I = 0$ and strangeness $S = -1$ negative parity baryon resonance ($J^P = 1/2^-$). It is assigned to the lowest $L = 1$ supermultiplet of the three-quark system, together with its spin-orbit partner, the ($J^P = 3/2^-$) $\Lambda(1520)$.

The existence of the $\Lambda(1405)$ was first predicted by Dalitz and Tuan in 1959 [1; 2], they showed that the unitarity in the $\bar{K}N - \Sigma\pi$ coupled channel system leads to a resonance pole in the $\Sigma\pi$ amplitude. Such state only decays into $(\Sigma\pi)^0$ ($I = 0$) through the strong interaction. Due to the difficulty to perform scattering experiments directly in the $\Sigma\pi$ channel, the properties of the resonance can only be explored by studying the invariant mass spectrum of the $\Sigma\pi$ final state in production experiments. The first experimental evidence of this resonance dates back to 1961 [3] in the $K^-p \rightarrow \Sigma\pi\pi\pi$ reaction at $1.5\text{GeV}/c$. Despite the fact that the $\Lambda(1405)$ has since then been observed in many experiments, and is currently listed as a four-stars resonance in the table of the Particle Data Group (PDG) [4], its nature still remains unsettled.

The simple three quark picture (uds) meets some difficulties to explain the observed $\Lambda(1405)$ mass. A negative parity three quark baryon needs one of the quarks to be excited to the $l = 1$ orbit. A direct comparison with the nucleon sector

(where one of the lowest $P = -1$ baryons is the $N(1535)$) suggests an excitation energy of about 600MeV (above the $\Lambda(1116)$) as a consequence of the heavier strange quark. This would locate the Λ^* mass around $1700\text{MeV}/c^2$. Moreover, in the nucleon sector the lowest $J^P = 3/2^-$ state is the $N(1520)$ which is almost degenerate in mass with the $N(1535)$. If the $\Lambda(1520)$ is accepted as the $\Lambda(1405)$ spin-orbit partner, a mass splitting more than $100\text{MeV}/c^2$ remains unexplained. The low mass of the $\Lambda(1405)$ can be explained in a five quark picture (where $P = -1$ is obtained by putting four quarks and an antiquark in the $l = 0$ orbit) which, however, predicts more, unobserved, excited baryons.

In the meson-baryon picture the $\Lambda(1405)$ is viewed as a $\bar{K}N$ quasi-bound $I = 0$ state, embedded in the $\Sigma\pi$ continuum, emerging in coupled-channel meson-baryon scattering models [5].

In recent years, a renewed interest on the $\Lambda(1405)$ was triggered by the development of chiral unitary approaches. In this context, the structure of the resonance is investigated combining the low energy interaction, governed by chiral symmetry, and the unitarity condition for the coupled-channel scattering amplitude [6; 7; 8] (see also [9; 10] for a complete review on the chiral unitary approach).

Of particular interest, in the context of chiral theories, is the emergence of two poles in the scattering amplitude (with $S = -1$ and $I = 0$) in the neighborhood of the $\Lambda(1405)$ mass, both contributing to the final experimental invariant mass distribution [8; 11]. One pole is located at higher energy (around $1425\text{MeV}/c^2$) with a narrow width, the other pole is shifted at lower energies (around $1390\text{MeV}/c^2$) with a larger width. The most recent results reported in [12] from a coupled-channel calculation, based on the next-to-leading order chiral $\text{SU}(3)$ meson-baryon effective Lagrangian give:

$$(z_1 = 1424_{-23}^{+7} - i26_{-14}^{+3} \quad , \quad z_2 = 1381_{-6}^{+18} - i81_{-8}^{+19}) \text{ MeV}, \quad (1.1)$$

where the real and imaginary parts of the pole positions represent the mass and halfwidth of the resonance, respectively (in the following we will mean by Γ the full width of mass distributions). As a consequence, according to chiral theory, the nominal $\Lambda(1405)$ is not a single resonance, but instead the superposition of these two independent states having the same quantum numbers. Both poles locate below the $\bar{K}N$ threshold, so the $\Sigma\pi$ state ($I = 0$) is the only opened final state for the two poles. Moreover, the two poles are found to be differently coupled

to the $\bar{K}N$ and $\Sigma\pi$ channels. The higher mass pole results to be coupled mostly to the $\bar{K}N$ channel, while the lower mass pole is dominantly coupled to the $\Sigma\pi$ channel. Due to the different couplings of the two resonances, the shape of the $\Lambda(1405)$ strongly depends on the formation mechanism. Since the resonance is always seen in the invariant mass spectrum of the $\Sigma\pi$ strong decay channel, the only possibility to observe the higher mass pole is having a reaction in which the $\Lambda(1405)$ is produced from the $\bar{K}N$ channel.

The lineshape of the $\Lambda(1405)$ invariant mass spectrum also strongly depends on the observed decay channel [11] as a consequence of the isospin interference term. Neglecting the small $I = 2$ component, the $\Sigma\pi$ spectrum can be decomposed as

$$\frac{d\sigma(\Sigma^-\pi^+)}{dM} \propto \frac{1}{3}|T^0|^2 + \frac{1}{2}|T^1|^2 + \frac{2}{\sqrt{6}}\text{Re}(T^0T^{1*}) \quad (1.2)$$

$$\frac{d\sigma(\Sigma^+\pi^-)}{dM} \propto \frac{1}{3}|T^0|^2 + \frac{1}{2}|T^1|^2 - \frac{2}{\sqrt{6}}\text{Re}(T^0T^{1*}) \quad (1.3)$$

$$\frac{d\sigma(\Sigma^0\pi^0)}{dM} \propto \frac{1}{3}|T^0|^2 \quad (1.4)$$

Where T^I represents the amplitude in the isospin channel I , and M is the $\Sigma\pi$ invariant mass. The three spectra would coincide only if the $|T^0|^2$ term would dominate, but this is not the case, as demonstrated by the measured $\Lambda(1405)$ over $\Sigma(1385)$ (isospin $I = 1$) photoproduction ratio [13]. The third term in 1.2 and 1.3, the isospin interference term, causes the difference between the two invariant mass spectra.

From 1.4 we see that the $\Sigma^0\pi^0$ lineshape is free from the important $I = 1$ $\Sigma(1385)$ contamination, and from the isospin interference term. $\Sigma^0\pi^0$ turns then to be the privileged channel to investigate the nature of the $\Lambda(1405)$.

Both objectives, to produce the $\Lambda(1405)$ through the K^-p mechanism and to observe the resonance studying the clean $\Sigma^0\pi^0$ decay channel, can be achieved with the KLOE detector at DAΦNE. The strategy is to identify K^- nuclear absorptions (of the low momentum kaons from ϕ decay produced at the DAΦNE e^+e^- collider) in the KLOE detector materials (used as active targets) employing the excellent tracking resolution of the KLOE drift chamber and the calorimeter for detecting charged particles and photons.

The nature of the Λ^* resonance is not only a central issue for the role it plays in the spectrum of baryons. As the antikaons belong to the octet of Nambu-Goldstone bosons associated to the spontaneous breaking of chiral $SU(3)_R \times SU(3)_L$ symmetry of QCD, the Λ^* is fundamental in various aspects of non-perturbative QCD (due to the intimate connection with the strongly attractive $\bar{K}N$ channel). Understanding its structure can then shed light on interesting phenomena of the dynamics of \bar{K} in nuclear medium, such as the partial restoration of chiral symmetry, or the formation of deeply bound states of \bar{K} in nuclei. Deeply Bound Kaonic Nuclear States (DBKNS) were recently predicted in light nuclei [14], arising as a consequence of the strong attractive $\bar{K}N$ interaction in the $I = 0$ channel, based on the $\bar{K}N$ quasi-bound interpretation of the $\Lambda(1405)$.

1.2 Experimental results on the $\Lambda(1405)$ lineshape compared with theoretical calculations

We will describe in this section some of the most interesting experimental investigations of the Λ^* resonance performed with different techniques (a more comprehensive review can be found in [9]) starting from bubble chamber experiments up to the more recent findings.

The highest statistics Λ^* production in bubble chamber experiments was achieved by Hemingway [15], exposing a hydrogen bubble chamber to a $4.3 \text{ GeV}/c$ K^- beam and investigating the reaction

$$K^- p \rightarrow \Sigma^+(1660)\pi^-, \quad \Sigma^+(1660) \rightarrow \Lambda(1405)\pi^+, \quad \Lambda(1405) \rightarrow \Sigma^\pm\pi^\mp. \quad (1.5)$$

Both $\Sigma^\pm\pi^\mp$ distributions are shown in the paper for the events fulfilling the following selections on the momentum transfer and $\Sigma^+(1660)$ invariant mass:

$$t'(p \rightarrow \Sigma\pi\pi) < 1.0 (\text{GeV}/c)^2, \quad 1.60 \text{ GeV}/c^2 < M(\Sigma\pi\pi) < 1.72 \text{ GeV}/c^2. \quad (1.6)$$

As the $\Sigma^-\pi^+$ spectrum is expected to suffer a high nonresonant contamination (due to the ambiguity in the $\Sigma^-\pi^+$ pairing) only the $\Sigma^+\pi^-$ spectrum was used (applying

several fitting schemes) by Dalitz and Deloff [16] to obtain the resonance mass and width:

$$M = 1406.5 \pm 4.0 \text{ MeV}/c^2, \quad \Gamma = 50 \pm 2 \text{ MeV}/c^2. \quad (1.7)$$

It was nevertheless questioned [9] that the charged ($\Sigma^\pm \pi^\mp$) spectra should suffer a contamination of the $I = 1$ component (see equations 1.2 and 1.3). Moreover the energy cut effect ($1.60 \text{ GeV}/c^2 < M(\Sigma\pi\pi) < 1.72 \text{ GeV}/c^2$) on the $\Sigma^+ \pi^-$ phase space should be taken into account.

Of great importance, to be compared with the results of present analysis of the $\Sigma^0 \pi^0$ channel, generated in K^- interactions in the gas filling the KLOE drift chamber (mainly helium) (see chapter 5) is the bubble chamber study performed by Riley et al. [17] of the reaction

$$K^- {}^4\text{He} \rightarrow \Sigma^\pm \pi^\mp {}^3\text{H} \quad (1.8)$$

with K^- stop in a liquid target. In this work, the $\Sigma^\pm \pi^\mp$ invariant mass distributions were fitted with various impulse models, leaving as free parameters the relative amounts of captures from S , P and D orbital angular momentum states of the mesonic atom. The impulse approximation consists in assuming that the interaction proceeds as

$$K^- + p + (ppn)_s \rightarrow \Sigma^\pm \pi^\mp + (ppn)_s, \quad (1.9)$$

where $(ppn)_s$ behaves like a spectator in the process. The adopted fitting distributions do not take into account for final state interactions of the produced $\Sigma^\pm \pi^\mp$ with the residual nucleus. The best fit to the measured $\Sigma^\pm \pi^\mp$ invariant mass distributions implies predominantly S -state capture. The $m_{\Sigma^+ \pi^-}$ and $m_{\Sigma^- \pi^+}$ spectra are similar, both are peaked at $1405 \text{ MeV}/c^2$ and are sharply cut in correspondence of the kinematical limit for K^- absorption in ${}^4\text{He}$ at rest ($\sim 1412 \text{ MeV}/c^2$). The authors suggest to perform $K^- {}^4\text{He}$ absorption studies in flight, with low momentum kaons.

The Riley et al. [17] data were not used to deduce information about the $\Lambda(1405)$ till the analysis of Esmaili, Akaishi and Yamazaki [18], since the lineshape looks as being a consequence of a non resonant capture process. In [18] both K^- resonant and non-resonant capture at rest by a nuclear proton ("p") in ${}^4\text{He}$ are

calculated

$$K^- "p" \rightarrow \Sigma\pi \quad \text{direct non-resonant capture} \quad (1.10)$$

$$K^- "p" \rightarrow \Lambda^* \rightarrow \Sigma\pi \quad \text{resonant capture.} \quad (1.11)$$

The calculation was performed by a coupled-channel procedure, for a K^-p quasi-bound state of arbitrary mass and width. The $m_{\Sigma\pi}$ invariant mass spectra for two chosen Λ^* pole positions of $1405\text{MeV}/c^2$ and $1420\text{MeV}/c^2$, are found to be very similar and both peaked just below the kinematical limit (at rest). Also the shapes of the corresponding non-resonant capture spectra are comparable, and very close to the resonant spectra, but have much smaller intensities. As pointed in [18] the $m_{\Sigma\pi}$ invariant mass distribution could be considered a "projected spectrum" as it is strongly constrained by the kinematics. The performed χ^2 fit to the experimental distribution [17] confirms the much preferred S -orbit capture. The fit of the $K^- {}^4\text{He}$ data with theoretical $m_{\Sigma\pi}$ spectra of various resonance masses and widths (also considering small P -orbit capture and $\Sigma(1385)$ contributions) gives a minimum χ^2 corresponding to the values:

$$m = 1405.5^{+1.4}_{-1.0}\text{MeV}/c^2 \quad \text{and} \quad \Gamma = 23.6^{+4}_{-3}\text{MeV}/c^2. \quad (1.12)$$

Thanks to the kind interest of Professors Akaishi and Yamazaki to our $\Sigma^0\pi^0$ analysis we could take advantage of the results of their coupled-channel calculations, adapted to the DAΦNE/KLOE experimental situation. The calculated $m_{\Sigma\pi}$ invariant mass distribution for K^- absorption in ${}^4\text{He}$ is shown in figure 1.1. The $m_{\Sigma\pi}$ spectra were calculated, as described above, for three different Λ^* pole hypothesis ($1390\text{MeV}/c^2$, $1405\text{MeV}/c^2$ and $1420\text{MeV}/c^2$) and a common width of $\Gamma = 40\text{MeV}/c^2$. Both captures at rest and interactions in flight were calculated for a K^- momentum of $120\text{MeV}/c$. The K^\pm pairs are produced in DAΦNE by ϕ decay almost at rest with a momentum $p_k = 127\text{MeV}/c$, but then undergo some energy loss in crossing the beam pipe and the drift chamber entrance wall (see chapter 2).

The simulated $m_{\Sigma\pi}$ distributions for the same Λ^* poles, and a much narrower assumed width $\Gamma = 10\text{MeV}/c^2$ is shown in figure 1.2.

We will describe in the following some recent experiments rising an intense theoretical debate on the controversial features of the Λ^* lineshape.

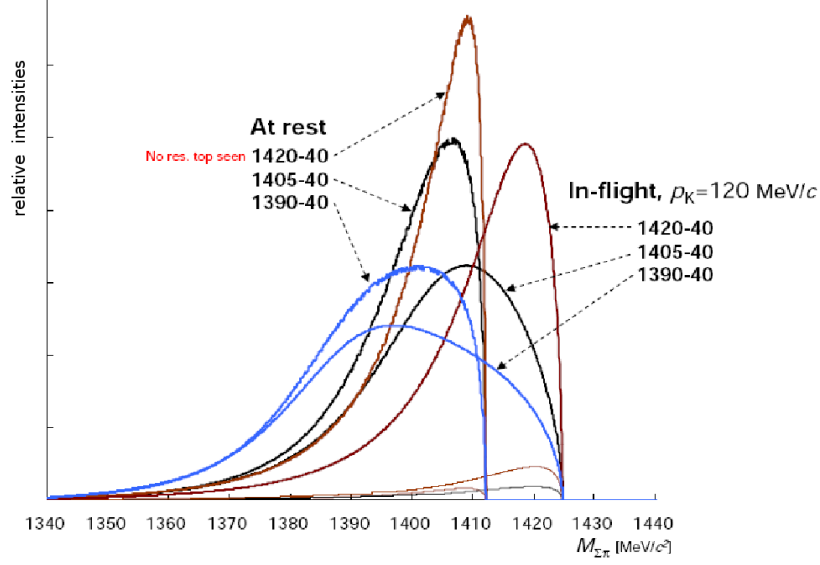


Figure 1.1: $m_{\Sigma\pi}$ distribution for various Λ^* pole hypothesis and a common width $\Gamma = 40 \text{ MeV}/c^2$, generated at rest and in flight ($p_k = 120 \text{ MeV}/c$). Kind courtesy of Professors Akaishi and Yamazaki.

In [19] the $\Sigma^0\pi^0$ spectrum was analyzed in pp collisions at a beam momentum of $3.65 \text{ GeV}/c$, the strategy consisting in the search for four-fold coincidence of two protons, one positive kaon and a negative pion, which could correspond to one of the following reaction chains:

$$pp \rightarrow pK^+\Sigma^0(1385) \rightarrow pK^+\Lambda\pi^0 \rightarrow pK^+p\pi^-\pi^0 \quad (1.13)$$

$$pp \rightarrow pK^+\Lambda(1405) \rightarrow pK^+\Sigma^0\pi^0 \rightarrow pK^+\Lambda\gamma\pi^0 \rightarrow pK^+p\pi^-\gamma\pi^0. \quad (1.14)$$

Forward and side-wall counters were used to identify protons. A cut on the invariant mass of the side-wall proton and pion is introduced to reduce the combinatorial background. Then the $\Sigma^0(1385)$ and $\Lambda(1405)$ events are discriminated by a cut on the missing mass $MM(pK^+p\pi^-)$, optimised on MC $\Sigma^0(1385)$ simulations ($MM(pK^+p\pi^-) > m(\pi^0 + 55 \text{ MeV}/c^2)$). The final statistics is limited. In [19] the obtained missing mass $MM(pK^+p\pi^-)$ spectrum is compared with the results of

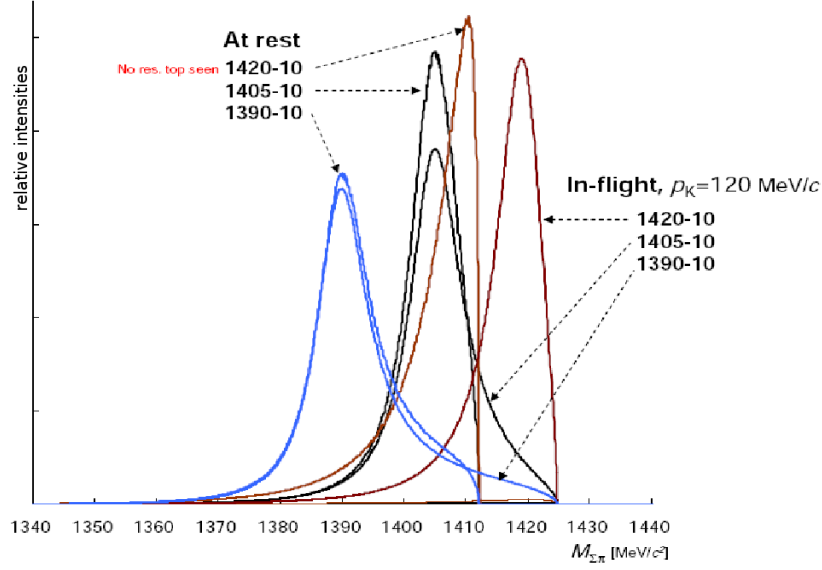


Figure 1.2: $m_{\Sigma\pi}$ distribution for various Λ^* pole hypothesis and a common width $\Gamma = 10\text{MeV}/c^2$, generated at rest and in flight ($p_k = 120\text{MeV}/c$). Kind courtesy of Professors Akaishi and Yamazaki.

[15] and, despite the very different production mechanisms, the shapes are found to be consistent.

The $\Sigma^0\pi^0$ distribution was also observed in the $K^-p \rightarrow \Sigma^0\pi^0\pi^0$ reaction with kaons in the momentum region $p_k = 514 - 750\text{MeV}/c$ in [20]. The $m_{\Sigma^0\pi^0}$ invariant mass distribution results peaked at $1420\text{MeV}/c$, with a narrower width with respect to the $50\text{MeV}/c^2$ PDG value, although not explicitly mentioned in [20]. The invariant mass spectrum was extensively studied in a following paper [21] within a chiral unitary approach. The $K^-p \rightarrow \Sigma^0\pi^0\pi^0$ reaction was investigated in [21] in the same K^- energy region and was found to be dominated by the emission of a π^0 prior to the K^-p interaction. This ensures a large contribution of the higher energy pole (predicted by chiral unitary models) to the final invariant mass spectrum. The calculated $m_{\Sigma^0\pi^0}$ invariant mass spectrum results to be peaked at $1420\text{MeV}/c^2$ with a width of $38\text{MeV}/c^2$ (after removing the non-resonant background coming from "wrong" $\Sigma^0\pi^0$ couples). The calculated $m_{\Sigma^0\pi^0}$ distribution accurately reproduces the experimental spectrum [20].

Recent results on Λ^* photoproduction through the reaction $\gamma p \rightarrow K^+\Sigma\pi$ where

reported in [22], where the Λ^* lineshape was studied for the first time over the three different $\Sigma\pi$ decay channels simultaneously. The three lineshapes are seen to be different from each other, as predicted by the chiral unitary model, with the $\Sigma^+\pi^-$ peaking at a higher mass ($\sim 1420\text{MeV}/c^2$) and having a narrower structure with respect to the $\Sigma^-\pi^+$. This is in contradiction with the theoretical prediction [11] which associates a higher mass peak to the narrower $\Sigma^-\pi^+$ distribution. It was however noticed [9] that such a discrepancy could be a consequence of the angular dependence of the detector acceptance, where the theoretical differential cross section was integrated over the final state angles.

In addition, the Λ^* electroproduction was recently observed [23], with an electron beam of $5.5\text{GeV}/c$ on a liquid hydrogen target. The $\Sigma^+\pi^-$ decay channel was chosen for the Λ^* and the $p\pi^0$ channel for the Σ^+ . The obtained missing mass spectrum $MM(e^-K^+)$ shows two peaks (besides the dominant $\Lambda(1520)$) for $1.5\text{GeV}^2 < Q^2 < 3.0\text{GeV}^2$, while they are not resolved in the lower Q^2 range ($1.0\text{GeV}^2 < Q^2 < 1.5\text{GeV}^2$). A fit performed to the $MM(e^-K^+)$ distribution (in the higher Q^2 region) gives the following values for the masses and widths of the two observed peaks:

$$m_1 = 1422\text{MeV}/c^2, \Gamma_1 = 16\text{MeV}/c^2 ; \quad m_2 = 1393\text{MeV}/c^2, \Gamma_2 = 100\text{MeV}/c^2. \quad (1.15)$$

The masses of the two components seem in agreement with chiral unitary two-poles predictions, while the widths are significantly narrower.

The $\Sigma\pi$ charged spectra in the pp collision at 3.5GeV was studied by the HADES collaboration at GSI [24].

A Carbon target was recently installed inside the KLOE detector by the AMADEUS / KLOE collaboration at DAΦNE [25], to perform an exclusive study of the Λ^* decay, produced in K^- absorption on bound protons. Preliminary results will be presented in section 4.9. New experiments are planned like E31 at J-PARC [26].

1.3 K^- nuclear interaction studies in emulsion and Helium bubble chamber experiments

A crucial aspect of the present analysis, is the performed comparative study of the obtained mass and momentum distributions with the higher resolution bubble chamber and emulsion results (see sections 4.8, 5.6). The comparison with older $K^-^{12}C$ and K^-^4He spectra produced in at rest reactions served us as a guide, enabling the identification of the in flight K^- interactions contribution, and therefore, to a deep understanding of the different kinematical regimes. In addition a careful investigation of the momentum spectra of the particles resulting from the decay process, enable a characterization of the $\Sigma(1385)$ background, which can not decay into the searched $\Sigma^0\pi^0$ channel for isospin conservation, but decays into $\Lambda\pi^0$.

1.3.1 K^- nuclear interactions at rest in emulsion experiments

We will report here some results obtained for K^- absorption studies in emulsion, with particular emphasis on the momentum and invariant mass distributions. Comparison with these results will turn to be extremely useful in the interpretation of the $\Sigma^0\pi^0$ spectra originated by K^- interaction in the KLOE drift chamber entrance wall (mainly Carbon) (see section 4.8). In the mentioned experiments K^- reactions in light emulsion nuclei (C, N, O) are investigated and compared to theoretical predictions.

The nuclear capture in Carbon of atomic K^- (of particular interest for us) is expected to occur in high angular momentum states [27]. Kaons are slowed down, captured in an atomic orbit, undergo the cascade process and are then absorbed by the nucleus from an atomic orbit. From kaonic x-ray measurements [28] absorptions from d states result to be predominant. As a consequence of the centrifugal barrier the reaction $K^-C \rightarrow \Sigma\pi^{11}B$ is confined to the low density surface region. Hence, the $\Sigma\pi$ production follows the quasi-free K^- interaction with a single proton in the nucleus. The surface confinement of the capture process is consistent with the experiment of Keane [29], in which the residual ^{11}B nucleus is found in a not excited state. It is then natural to assume the absorption occurring

on the last bound $p_{3/2}$ proton. Considering the separation energy of the $p_{3/2}$ proton ($\sim 16\text{MeV}$) the kinematical threshold for K^- absorption at rest in Carbon corresponds to an invariant mass $\sim 1416\text{MeV}/c^2$.

In [30] a total sample of 128 K^- interactions at rest in emulsion with a charged Σ hyperon, a pion and a recoiling nucleus is selected, retaining only events in which Σ^+ decays at rest to a proton and Σ^- interacts at rest. The pion kinetic energy distribution (which was determined with a relative error of 1.5% for stopping pions, up to about 10%) is shown in figure 1.3 and exhibits a peak at 50-60 MeV; the hyperon kinetic energy was determined with a relative error of 1-2%.

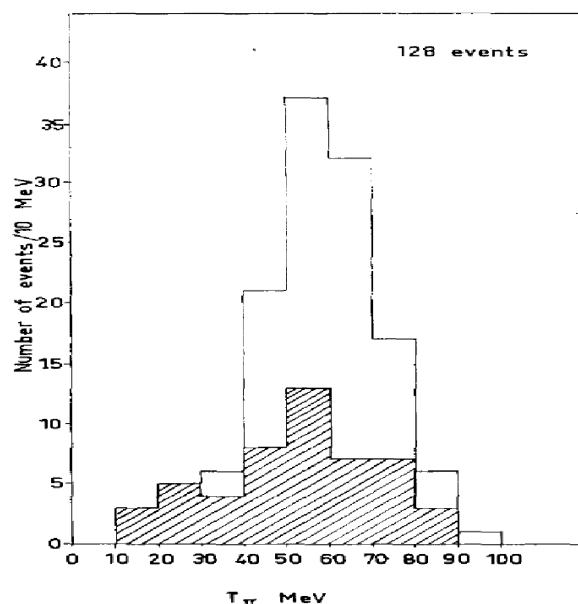


Figure 1.3: Pions kinetic energy distribution from [30], the hatched area represents stopping pions.

The momentum distribution of the $\Sigma\pi$ system was also studied in [30]. The maximum of the $p_{\Sigma\pi}$ spectrum occurs in the momentum interval 180-200 MeV/c and the full width is about 100 MeV/c. In [30] a compilation of precedent experiments with similar selection criteria was also made and the corresponding $p_{\Sigma\pi}$ distribution is shown in figure 1.4. The solid curve in figure 1.4 represents Adair's calculation [31] of the $\Sigma\pi$ momentum distribution, for K^- atomic capture in Carbon according to the reaction:

$$K^- C \rightarrow \Sigma\pi^{11}B. \quad (1.16)$$

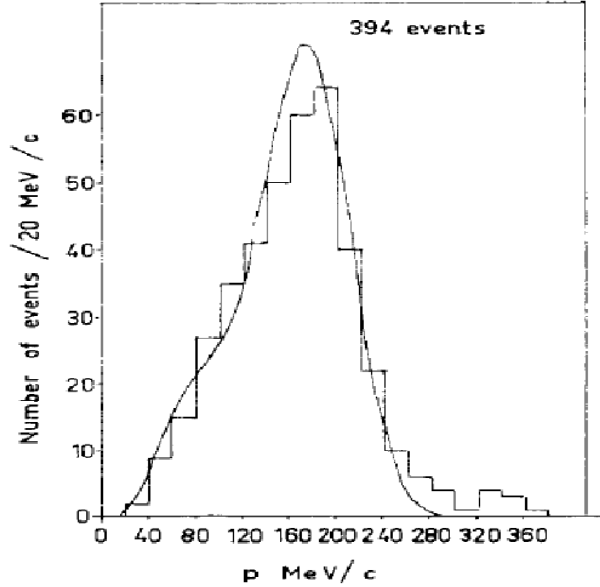


Figure 1.4: Momentum distribution of the $\Sigma\pi$ couples from [30] comprehensive of all the statistics from similar experiments with analogous selection criteria for $\Sigma\pi$. The solid curve represents the momentum distribution calculated by Adair.

The resolution in the $\Sigma\pi$ invariant mass is about $4 \text{ MeV}/c^2$. The $m_{\Sigma\pi}$ spectrum shows a clear similarity with the spectrum obtained in [17] for K^- interactions at rest in helium. The $m_{\Sigma\pi}$ distribution is peaked at $1405 \text{ MeV}/c^2$ with a sharp cut around the kinematical limit for K^- absorption in carbon at rest ($\sim 1416 \text{ MeV}/c^2$).

Figure 1.4 contains in particular the selected $\Sigma\pi$ events by Barbaro-Galtieri et al. [32] representing, together with [30], the highest statistics emulsion experiment. In [32] a detailed analysis of the scatter diagram $p_{\Sigma\pm\pi\mp}^2$ over $m_{\Sigma\pm\pi\mp}^2$, compared with the kinematical relations of the same variables for different nuclei, is performed for the recoil events. This is enabled by the small average errors on $p_{\Sigma\pm\pi\mp}^2$ and $m_{\Sigma\pm\pi\mp}^2$ ($1.9 \text{ MeV}/c$ and $1.0 \text{ MeV}/c^2$ respectively). Such study leads to the identification of the $K^- C \rightarrow \Sigma\pi^{11}B$ recoil events. In [32] an a posteriori selection was also adopted to avoid the bias introduced by low momentum recoiling nuclei (which are not expected to have a detectable range). The invariant mass distribution $m_{\Sigma\pm\pi\mp}$ reported in [32] is shown in figure 1.5.

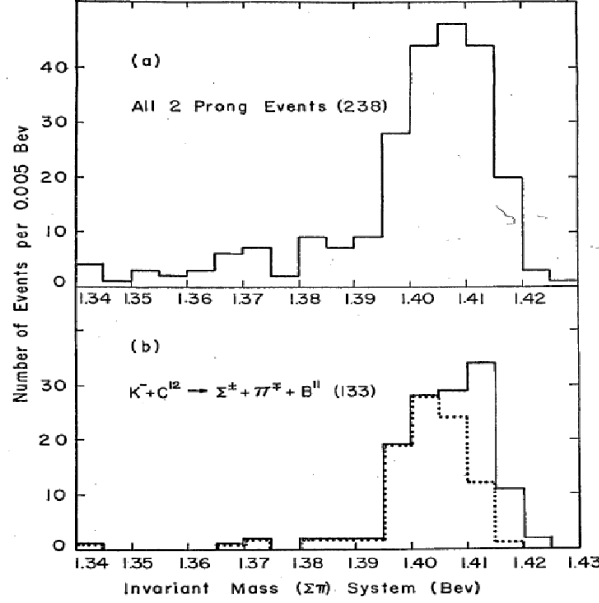


Figure 1.5: $m_{\Sigma^\pm\pi^\mp}$ spectrum from [32], the dotted line represents the invariant mass distribution of the subsample with $p_{\Sigma^\pm\pi^\mp} > 100 \text{ MeV}/c$.

1.3.2 Bubble chamber studies of K^- interactions at rest in helium

In this section we will quote some results from K^- absorption in Helium bubble chamber experiments, which served as a reference to the study of K^- interaction in the gas filling the KLOE drift chamber, whose main component is ^4He (see chapter 5).

In [33] Katz et al. performed a complete analysis of negative kaons nuclear absorption in Helium bubble chamber, with the aim of identifying each event with a particular reaction, and measure the branching ratios of the possible final states. Particularly interesting for our purposes is the branching fraction for $\pi^0 \Lambda(pnn) + \pi^0 \Sigma^0(pnn)$ production (where (pnn) indicates a bound or an unbound combination of the three nucleons):

$$K^- {}^4\text{He} \rightarrow \pi^0 \Lambda / \Sigma^0(pnn) = (22.5 \pm 4.2)\%. \quad (1.17)$$

The $\Lambda\pi^0$ and $\Sigma^0\pi^0$ branching fractions are then obtained using the information of the corresponding $\Lambda\pi^\pm$ production fractions, by means of isospin invariance:

$$BR(\Lambda\pi^0) = \frac{1}{2} [BR(\Lambda\pi^-) + BR(\Lambda\pi^+)] = (16.3 \pm 2.3)\%, \quad (1.18)$$

which yields $BR(\Sigma^0\pi^0) = (6.2 \pm 4.8)\%$. It is important to stress that the branching ratios for $\Lambda\pi^\pm$ production also include the internal conversion mechanism, in which a Σ converts into a Λ through the reaction

$$\Sigma N \rightarrow \Lambda N. \quad (1.19)$$

The average percentage of $\Sigma - \Lambda$ conversion quoted in [33] is $(50 \pm 10)\%$.

Also of great interest for our study is the momentum distribution of the emerging pions. In figure 1.6 from [33] is represented the fitted π^0 momentum spectrum for $\pi^0 \Lambda^3 H$ events compared to the π^- spectrum from $\pi^- \Lambda^3 He$ events. An enhancement of events around $240 MeV/c$ appears. This finds a clear interpretation by comparing with the π^- momentum spectrum for all the $\pi^- \Lambda(ppn)$ events (figure 1.7 from [33]) where the higher momentum peak (around $240 MeV/c$) is associated to direct Λ production, while the lower momentum peak (around $160 MeV/c$) represents the Σ production followed by the subsequent internal conversion.

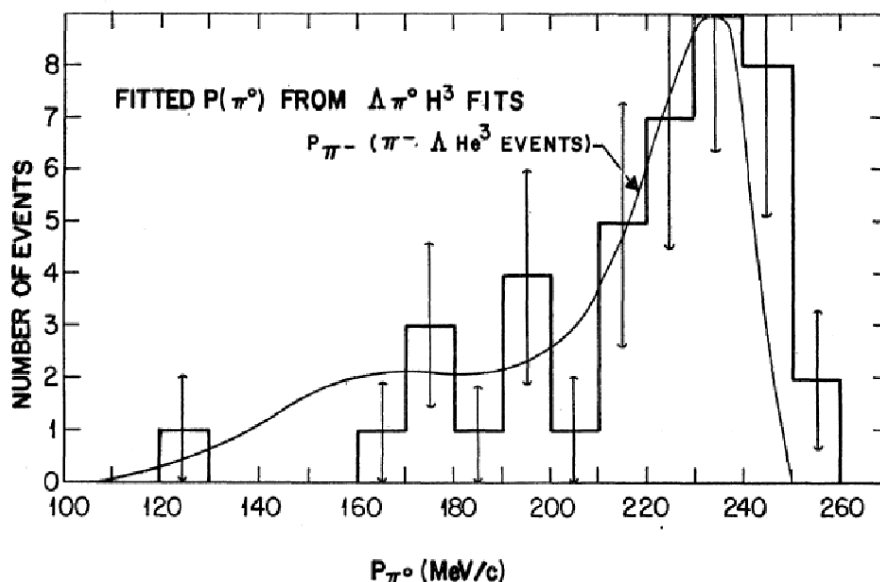


Figure 1.6: π^0 momentum spectrum for $\pi^0 \Lambda^3 H$ events, compared to the π^- spectrum from $\pi^- \Lambda^3 He$ events, from [33].

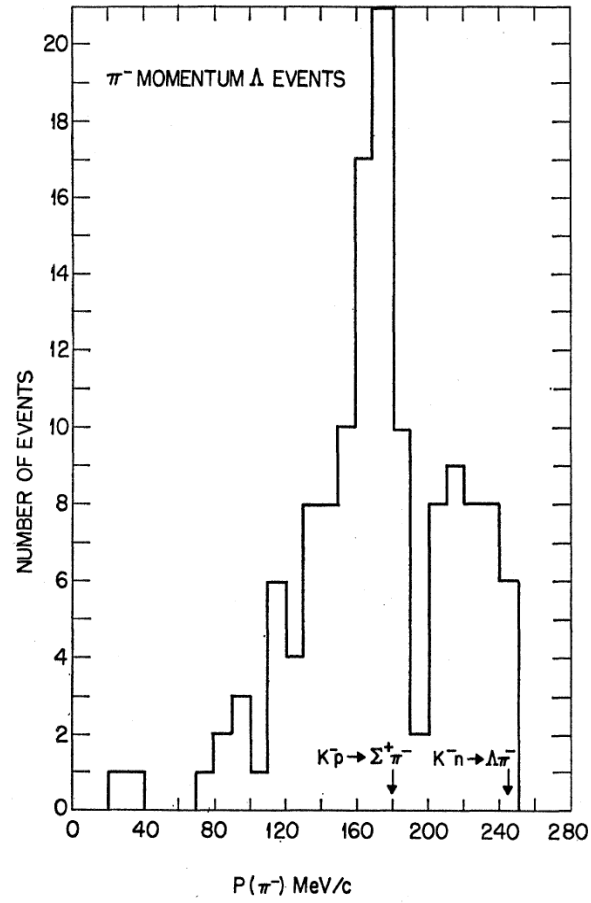


Figure 1.7: π^- momentum spectrum for all the $\pi^- \Lambda$ (ppn) events from [33]. The arrows indicate the kinematical limits for free Σ and Λ production.

In this context, a very useful and detailed analysis is performed in [34] where the interaction of negative kaons in a Helium bubble chamber is presented, yielding $\Lambda\pi^-$ and $\Sigma^0\pi^-$ in the final state, for both low momentum kaons and kaons at rest. In [34] Σ -conversion events (at rest) are found to be associated to π^- kinetic energies around $T_{\pi^-} \sim 70\text{MeV}$, while a higher kinetic energy component $T_{\pi^-} \sim 130\text{MeV}$ is interpreted as originating from direct $\Lambda\pi^-$ production at rest. As a further confirmation figure 1.8 from [34] shows that indeed the pion kinetic energy is distributed between 50MeV and 70MeV for $\Sigma^0\pi^-$ production at rest, with a sharp cut at about 80MeV , corresponding to the kinematical limit for $\Sigma^0\pi^-$ production at rest in Helium.

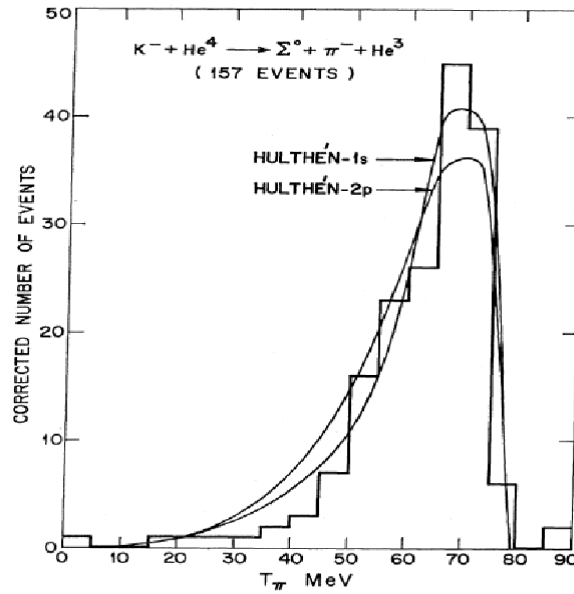


Figure 1.8: T_{π^-} distribution for $\pi^- \Sigma^0 {}^3\text{He}$ events, produced by K^- absorptions at rest, from [34]. The normalized impulse curves are calculated with the Kim matrix elements.

When considering K^- absorptions in-flight in Helium the sample was divided into two subsamples, according to kaons momenta in the ranges $160 - 280\text{MeV}/c$ and $280 - 360\text{MeV}/c$. We will refer here to the results obtained with the first subsample, as the p_k range is nearer to the kaons produced in DAΦNE ($p_k \sim 127\text{MeV}/c$). For this sample the region of T_{π^-} corresponding to Σ -conversion events is recognized between 60MeV and 140MeV . Few $\pi^- \Sigma^0 {}^3\text{He}$ productions in flight are reconstructed, whose kinetic energy (shown in figure 1.9 from [34]) is

distributed around $T_{\pi^-} \sim 110 \text{ MeV}$. The kinetic energy T_{π^0} for $\Sigma^0 \pi^0$ production in flight in ${}^4\text{He}$ filling the drift chamber of KLOE is expected slightly lower, due to the smaller K^- momentum.

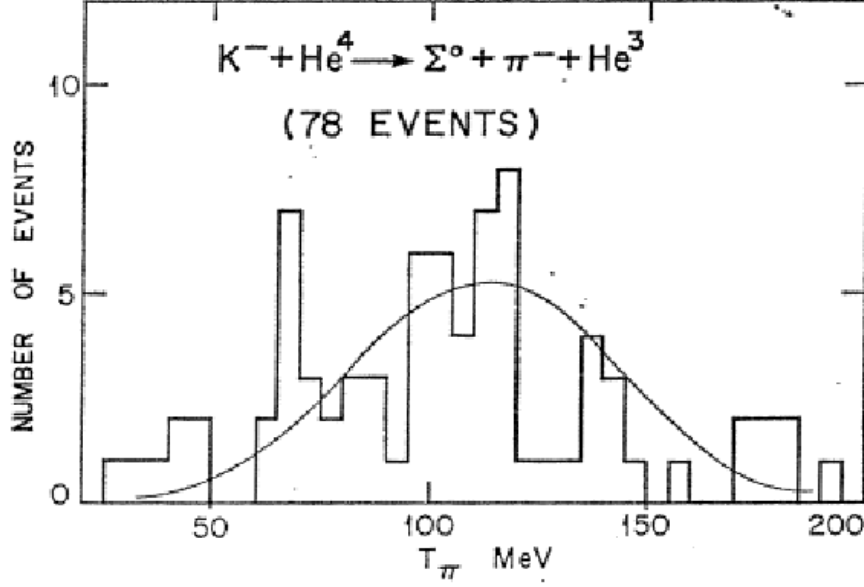


Figure 1.9: T_{π^-} spectrum for $\pi^- \Sigma^0 {}^3\text{He}$ events [34] (in the $K^- {}^4\text{He}$ C.M. frame), compared to the prediction of the impulse model using the Kim parameters.

In [34] also the $\Sigma^0 - \Lambda$ conversion fraction was estimated, comparing the relative branching ratios with predictions of different models. The internal conversion probability was found to range from 0.70 ± 0.04 for events at rest to 0.41 ± 0.15 for events in flight (at the higher beam momentum).

1.4 Summary

The scientific case of the $\Lambda(1405)$ nature is thoroughly topical, considered the outstanding role that the resonance plays in various aspects of hadron and nuclear physics. The structure of the resonance is closely related to the strongly attractive $\bar{K}N$ interaction, which is the fundamental ingredient for few body-antikaon systems study. Of particular interest is the investigation of the Λ^* in $\bar{K}N$ production experiments, to test the existence of a high mass pole, predicted by chiral unitary models [8; 11] to be coupled mostly to the $\bar{K}N$ channel.

The K^- nuclear absorption *at rest* on light nuclei was explored, through the $\Sigma^\pm\pi^\mp$ channel, in many bubble chamber and emulsion experiments, for which we can not complete the list of references. Some key results of emulsion experiments [30; 32] are:

- the pion kinetic energy distribution is peaked at 50-60 MeV ,
- the $p_{\Sigma\pi}$ spectrum is peaked at 180-200 MeV/c ,
- the $m_{\Sigma\pi}$ spectrum peaks at 1405 MeV/c^2 with a sharp cut corresponding to the kinematical limit ($\sim 1416MeV/c^2$).

Analogously from helium bubble chamber experiments [33; 34] we learn:

- the pion kinetic energy distribution for $K^- {}^4He$ absorptions at rest, exhibits a sharp cut in correspondence of the kinematical threshold $\sim 74MeV$,
- direct $\Lambda\pi$ production events are characterized by higher energy pions $T_\pi \sim 130MeV$,
- the $m_{\Sigma\pi}$ spectrum peaks at 1405 MeV/c^2 with a sharp cut corresponding to the kinematical limit ($\sim 1412MeV/c^2$).

Despite the $m_{\Sigma^\pm\pi^\mp}$ spectrum from $K^- {}^4He$ interactions at rest is well fitted by a ($m = 1405.5_{-1.0}^{+1.4}MeV/c^2$, $\Gamma = 23.6_{-3}^{+4}MeV/c^2$) resonance [18], the demand for investigating the higher mass kinematical region, accessed by in flight absorptions, was only accomplished by the present analysis of the $K^- {}^4He/K^- {}^{12}C$ interaction data collected by KLOE. Moreover, the following exclusive analysis of $\Sigma^0\pi^0$ channel, free from the main $I = 1$, $\Sigma(1385)$ background, allows a characterization of the Λ^* nature and it's behaviour in nuclear environment.

The $\Sigma^0\pi^0$ channel was only investigated in three experiments [19; 20; 22] up to now, with different results for the $\Lambda(1405)$ lineshape. Among these only in [20] the $\bar{K}N$ production mechanism was adopted. Although it was not explicitly mentioned in [20], the peak of the $m_{\Sigma^0\pi^0}$ invariant mass spectrum locates at 1420 MeV/c^2 [21].

Chapter 2

The KLOE detector at the DAΦNE collider

2.1 Introduction

The KLOE (KLong Experiment) experiment at DAΦNE was mainly conceived to measure direct CP violation in the $K^0 \bar{K}^0$ system produced in ϕ decay $\text{BR}(K_L^0 K_S^0) = 34.2 \pm 0.4\%$.

The ϕ meson decays also copiously produce charged kaons with $\text{BR}(K^+ K^-) = 48.9 \pm 0.5\%$. For this reason, the KLOE detector offers, through the study of the strong K^- nuclear interactions, a unique opportunity to explore the still open sector of low-energy strangeness nuclear physics.

2.2 The DAΦNE collider

DAΦNE [35] (Double Anular Φ -factory for Nice Experiments) is a double ring $e^+ e^-$ collider, designed to work at the center of mass energy of the ϕ particle $m_\phi = (1019.456 \pm 0.020) \text{MeV}$. The whole complex consists of a linear accelerator (LINAC), a damping ring (Accumulator) and the main DAΦNE rings, one for e^- one for e^+ , having in common the Interaction Region (IR). The beam pipe at the interaction region is made of 0.5mm beryllium-aluminium alloy, with a beam sphere (10 cm radius) around the interaction point. Fig. 2.1 shows the schematic layout of the DAΦNE complex.

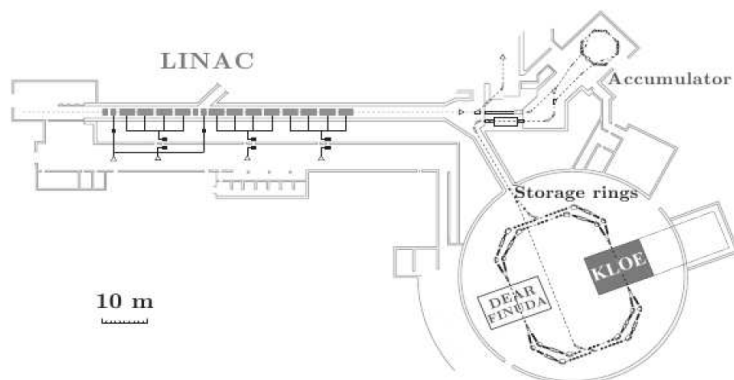


Figure 2.1: Layout of the DAΦNE accelerator complex

In the storage ring, ϕ mesons are produced in annihilation of electrons and positrons with a luminosity of $\sim 10^{32} \text{ cm}^{-2} \text{ s}^{-1}$. As the beam energies are tuned to 510 MeV, within $\pm 0.5\%$ for electrons and $\pm 1\%$ for positrons, ϕ mesons are produced almost at rest in the laboratory frame and decay in $K^+ K^-$ pairs, with a momentum of $\sim 127 \text{ MeV}$. The two rings cross at the interaction point with an angle of 25 mrad in the horizontal plane (x-z), as shown in the schematic representation 2.2, resulting in an average momentum along the x-axis $\langle p_{x,e^+e^-} \rangle \sim -12.7 \text{ MeV}$.

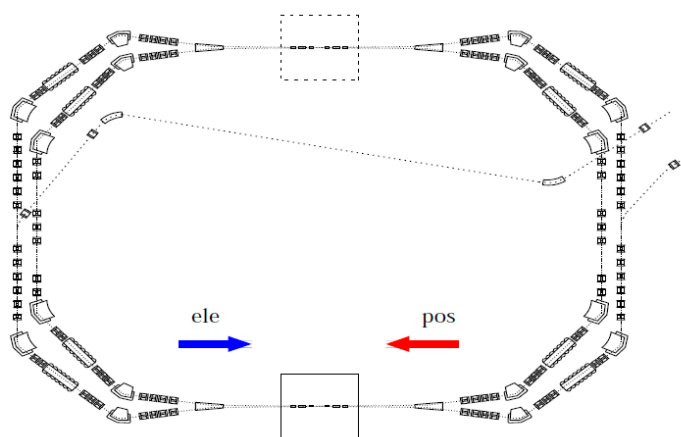


Figure 2.2: Schematic view of the DAΦNE collider. Boxes indicate the IRs, KLOE is located at the continuous line box position.

Considered a cross section $e^+ e^- \rightarrow \phi$ of about $3 \mu\text{b}$, the DAΦNE luminosity translates into hundreds of charged kaons produced per second. Kaons are char-

acterized by a low momentum which is ideal either to stop them in the materials of the KLOE detector, or to explore the products of the low energy nuclear absorptions of K^- . Also the back-to-back topology of the produced $K^+ K^-$ pairs is of extreme importance, given the possibility offered by the backwards K^+ extrapolation, as a powerful analysis tool.

2.3 The KLOE detector

The KLOE detector was designed for a completely different purpose than the present investigation of strangeness nuclear physics; its size and characteristics are optimized to reveal neutral kaons from ϕ decay. Nevertheless, we will show that the special features of KLOE turn to be ideal for our physical case, in terms of resolution and efficiency, enabling a unique investigation of the $\Sigma^0 \pi^0$ channel.

KLOE has a $\sim 4\pi$ geometry and an acceptance of 98%, as shown in figure 2.3, and is containing a large cylindrical Drift Chamber (DC) and a fine sampling lead-scintillating fibers calorimeter, all immersed in an axial magnetic field of $0.52T$ provided by a superconducting solenoid.

2.3.1 The KLOE drift chamber

The DC [36] has an inner radius of $0.25m$, an outer radius of $2m$, a length of $3.3m$ and is centered around the interaction point. The whole DC mechanics is made of carbon fiber. The two spherical end-plates have a curvature radius of $\sim 9,7m$ and a thickness of $8mm$. The gas sealing of the chamber is ensured by an inner aluminated carbon fiber cylinder and 12 external panels. The carbon layer is $750 \mu m$ thick and is composed 60% fiber ($\rho = 1.72g/cm^3$, $A = 12g$) and 40% epoxy ($\rho = 1.25g/cm^3$, $A = 12g$). The aluminium foil is $150 \mu m$ thick.

The chamber is uniformly filled with 12582 drift cells, organized in coaxial layers (12 inner and 46 outer), with alternating stereo angles. The stereo angles (see figure 2.4) are the angles comprised between the wires and the z -axis, the axes of the cylinder, and increase approximately with the square root of the radius of the layer, from $\pm 60 mrad$ to $\pm 150 mrad$. The resulting cell areas are $(2 \times 2) cm^2$ for the inners and $(3 \times 3) cm^2$ for the outer cells.

The gas mixture selected to fill the chamber is composed 90% in volume of 4He

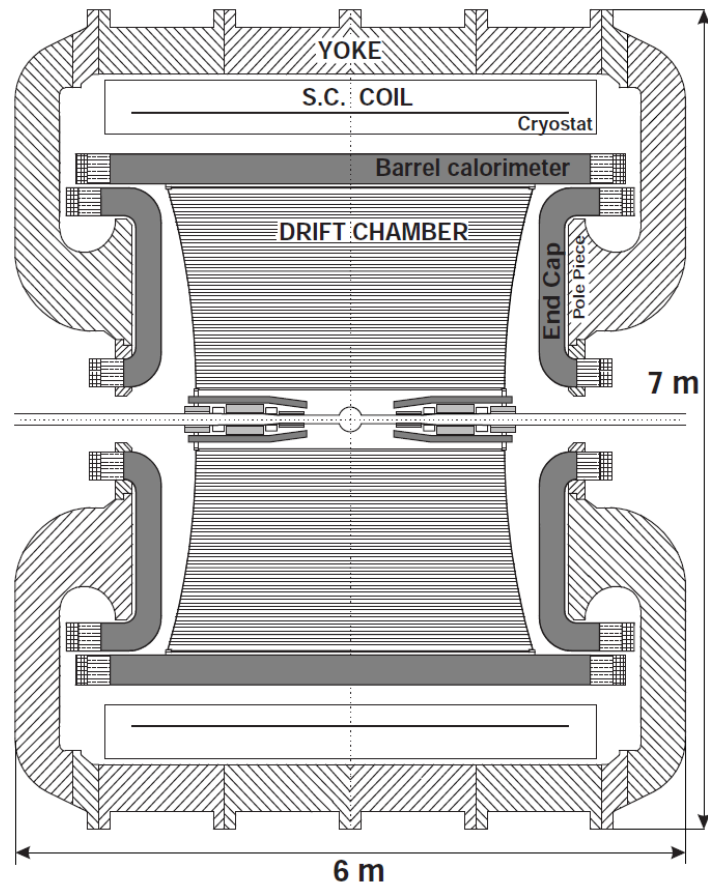


Figure 2.3: Section of the KLOE detector along the $x - z$ plane.

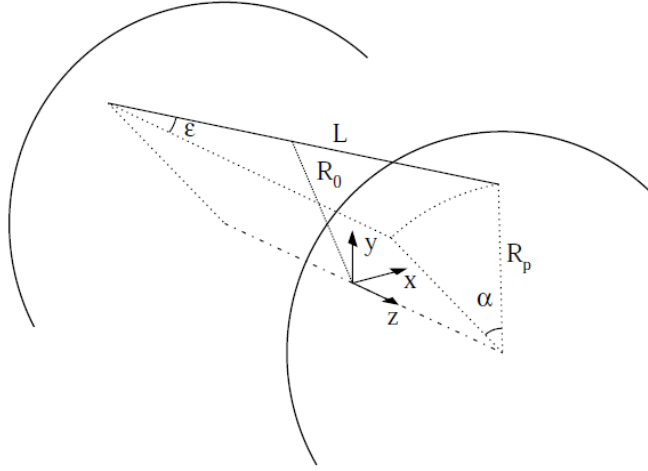


Figure 2.4: Stereo angle geometry for the drift cells of the KLOE DC.

and 10% of Isobutane C_4H_{10} . Helium is optimal to reduce multiple scattering, while Isobutane acts as quencer.

The signal coming from sense wires is sent to amplifiers and discriminators and then to the read-out system. The DC is instrumented with ADCs which give information about dE/dx and TDC for time measurements.

The chamber is characterized by excellent position and momentum resolutions. Tracks are reconstructed with a resolution in the transverse $R - \phi$ plane $\sigma_{R\phi} \sim 200\mu m$ and a resolution along the z -axis $\sigma_z \sim 2mm$. The vertex position is determined within $\sigma_{vtx} \sim 2mm$ over the whole sensitive volume. The transverse momentum resolution for low momentum tracks ($(50 < p < 300) MeV/c$) is $\frac{\delta p_T}{p_T} \sim 0.4\%$. Bhabha-scattering events were used to estimate the momentum resolution for $510 MeV e^\pm$, with a result of $\frac{\sigma_p}{p} \sim 0.25\%$ for polar angles in the interval $50^\circ < \theta < 130^\circ$. A further information, of particular interest for charged particles identification, is the dE/dx . dE/dx represents the truncated mean of the ADC collected counts due to the ionization in the DC gas.

2.3.2 The KLOE calorimeter

The KLOE calorimeter [37] is composed of a cylindrical barrel and two endcaps, providing a solid angle coverage of 98%. The barrel is divided in 24 trapezoidal section modules, $4.3m$ long and $23cm$ thick. The endcaps consist of 32 similar

modules with lengths ranging from $0.7m$ to $3.9m$ and $23cm$ thick. Each module is made of layers of grooved lead ($0.5mm$ thick) glued to scintillating fibers, with a diameter of $1mm$. The volume ratio (lead/fibers/glue=42:48:10) is optimized for a high light yield:

$$l.y. = \frac{1p.e.}{1MeV \cdot (\text{side at } 2m)} \quad (2.1)$$

and a high efficiency for photons in the range $(20 - 300)MeV$. The average density is $5 g/cm^3$ and the radiation length is $X_0 \sim 1.5cm$. Light pipes are used to connect both ends of the fibers to Photo-Multiplier (PM) tubes and the readout is divided into plans and columns with a granularity of about $((4.4 \times 4.4) cm)$. The signal from PM tubes is sent to trigger, to ADC for amplitude analysis and TDC for time measurements.

The position of the cluster along the fibers can be obtained, using the time difference measured by TDCs at the ends, with a resolution $\sigma_{\parallel} \sim 1.4cm/\sqrt{E(GeV)}$. The resolution in the orthogonal direction is $\sigma_{\perp} \sim 1.3cm$.

The response and resolution in the determination of the cluster energy (E_{cl}) were studied using $e^+e^- \rightarrow e^+e^-\gamma$ events. The photon energies are evaluated with high precision by the e^+e^- momenta and then compared with the reconstructed cluster energies. The calorimeter response, shown in figure 2.5 top as a function of the photons energy, is linear at better than 2% for photons with energy $E_{\gamma} > 75MeV$. The energy resolution is given by:

$$\frac{\sigma_E}{E_{\gamma}} = \frac{0.057}{\sqrt{E_{\gamma}(GeV)}}. \quad (2.2)$$

The time resolution for photon clusters t_{cl} is:

$$\sigma_t = \frac{57ps}{\sqrt{E_{\gamma}(GeV)}} \oplus 100ps. \quad (2.3)$$

As will be described in Chapter 3 the good time and energy resolutions, together with the high efficiency for photons detection, is mandatory for the present analysis of $K^-p \rightarrow \Sigma^0\pi^0$ events. It is worthwhile to spend few words on the possibility offered by the KLOE calorimeter to also detect neutrons. The efficiency of the KLOE detector for neutrons was tested by the KLOE group [38], on a prototype of the KLOE calorimeter at The Svedberg Laboratory (TSL) of Uppsala, with

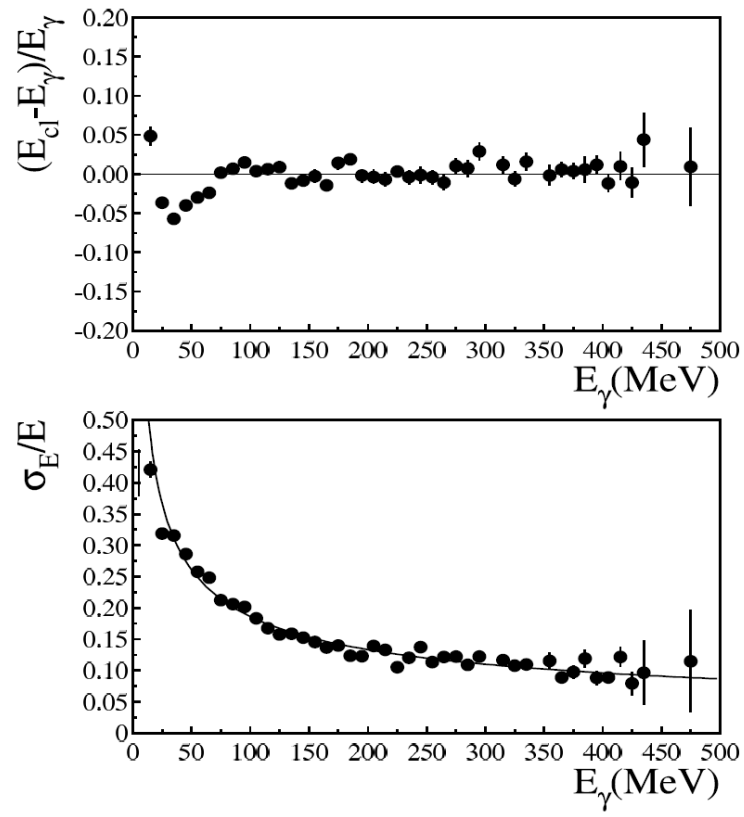


Figure 2.5: Linear response and energy resolution of the KLOE calorimeter.

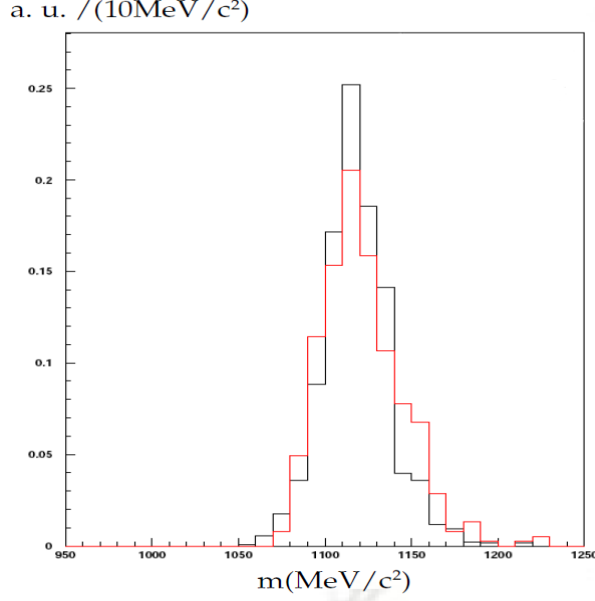


Figure 2.6: $m_{n\pi^0}$ invariant mass spectrum, black: data, red: simulated MC events.

neutron beams of energy 21, 46 and 174 MeV . A detection efficiency of about 35% was obtained for the higher energy beam.

Motivated by this study and supported by MC simulations of the KLOE calorimeter efficiency for neutrons detection (with neutrons energy-momentum distribution characteristic of K^-p nuclear absorptions) we explored the possibility to perform invariant mass spectroscopy for channels containing neutrons. The reactions $K^-p \rightarrow \Sigma^0\pi^0$ and $K^-p \rightarrow \Lambda\pi^0$ in the KLOE DC entrance wall were investigated, searching for $\Sigma^0 \rightarrow \Lambda\gamma$ and $\Lambda \rightarrow n\pi^0$ decays. The characterization of the neutron clusters time and energy distribution, and the obtained $m_{n\pi^0}$ (figure 2.6) invariant mass spectrum revealed promising perspectives, of particular interest for the study of the $\Lambda(1405)$ decay in channels containing neutrons, as an example:

$$\Lambda(1405) \rightarrow \Sigma^-\pi^+ \rightarrow n\pi^-\pi^+. \quad (2.4)$$

The neutron detection is also crucial to perform missing mass spectroscopy, in multinucleon K^-^4He absorption studies, using the DC gas as an active target.

2.4 Data reconstruction

The data acquisition is started by the two level KLOE trigger system [39], employing both energy deposits in the calorimeter and the multiplicity of hit wires. The data reconstruction program, DATAREC [40], starts immediately after the calibration procedure, and provides reconstruction of the calorimeter clusters, of tracks and association of tracks to clusters.

2.4.1 Cluster reconstruction

The energy response of the calorimeter is calibrated in different steps before and during the data taking. Before a stable data taking period cosmic rays are collected for one-two days, a sample of Minimum Ionizing Particles (MIP), crossing each calorimeter cell, is used to determine both the average MIP response and the fibre attenuation length. Run by run PM gain variations and the absolute energy scale are recalibrated by using $e^+e^- \rightarrow e^+e^-$ and $e^+e^- \rightarrow \gamma\gamma$ events respectively.

The calorimeter is divided into 2440 cells, read at both ends (A and B sides), providing information about the position of the energy deposit in the $r - \phi$ plane for the barrel and $x - y$ plane for the endcaps, together with the collected charge $Q_{A,B}^{ADC}$ and time $t_{A,B}^{TDC}$. The time and position along the fibre (the zero being taken at the fibre center) are then given by:

$$t(ns) = \frac{t_A + t_B}{2} - \frac{t_A^0 + t_B^0}{2} - \frac{L}{2v}, \quad (2.5)$$

$$s(cm) = \frac{v}{2} [(t_A - t_A^0) - (t_B - t_B^0)], \quad (2.6)$$

where $t_{A,B} = c_{A,B} \cdot t_{A,B}^{TDC}$, $c_{A,B}$ are the TDC calibration constants, $t_{A,B}^0$ are the time offsets, L and v are the length crossed by the photons and the light speed in the fibers respectively. The energy of the cell is taken as the mean of the energies measured at each end:

$$E_i(MeV) = \frac{E_{i,A} + E_{i,B}}{2}, \quad (2.7)$$

and the energy measured at one side is given by:

$$E_{i,AB}(MeV) = k_E \cdot g_i(s) \cdot \frac{S_{i,AB}}{S_{i,AB}^{MIP}}, \quad (2.8)$$

in 2.8 k_E is the calibration scale factor, $g_i(s)$ takes into account for the light attenuation along the fibre and is a function of the impact point position, $S = Q^{ADC} - Q^{0,ADC}$ represents the collected charge subtracted by the ADC zero offset. The cluster reconstruction algorithm first proceeds to group into pre-clusters contiguous cells into $r - \phi$ or $x - y$ planes, then cluster recognition is completed based on the t and s information. The cluster energy is

$$E_{cl} = \sum_{i=1}^{N_{cell}} E_i, \quad (2.9)$$

N_{cell} being the number of cells associated to the cluster. The cluster time t_{cl} and position \mathbf{r}_{cl} , are determined as energy-weighted averages over the involved cells.

2.4.2 Track reconstruction

The event reconstruction in the DC is performed in three steps: pattern recognition, track fit and vertex fit. Each step is handled separately and produces the information for the subsequent step.

- The first step of the pattern recognition algorithm is the hit association, inward from the outermost layer. By hit is meant a wire signal and the related information. Track segments and approximate parameters of their trajectories are obtained. Track segments are first searched in the $x - y$ plane, then the z coordinates are determined from a three-dimensional fit to all the associated hits.
- The track fit is obtained by minimizing a χ^2 function, employing estimates of the hit resolutions. Since the space-time relations depend upon the track parameters, the tracking procedure is iterative. At each step the position of successive hits is determined from the space time-relations and the track incident angle, estimating the energy loss and multiple scattering effects. After the first iteration some procedures are applied to check the sign assignment, to add or discard hits and to identify and join splitted tracks.

- Primary and secondary vertex positions are searched for by using the track parameters. The minimization of a χ^2 function, evaluated from the distances of closest approach between tracks and from the extrapolation errors, is performed.

2.4.3 Track to cluster association

The last step of data reconstruction consists in the association between tracks in the DC and clusters in the calorimeter. The method starts with the identification of decay chains based on primary and secondary vertices connection with tracks. The tracks at the end of the chains are then extrapolated to the inner calorimeter surface. Let us call \mathbf{r}_{ex} and \mathbf{p}_{ex} the position and the momentum of the particle at the extrapolated point. The cluster is considered to originate from the charged particle if the distance to the cluster centroid, in the plane orthogonal to the particle momentum, fulfill the condition

$$l = \left| (\mathbf{r}_{ex} - \mathbf{r}_{cl}) \cdot \frac{\mathbf{p}_{ex}}{|\mathbf{p}_{ex}|} \right| < 60cm. \quad (2.10)$$

Chapter 3

The events selection

3.1 Introduction

This chapter is devoted to the description of the events selection procedure, starting from the $\Lambda(1116)$ decay vertex reconstruction and proceeding through the identification and distinction of three photon clusters in the KLOE calorimeter.

3.2 The data sample

The analysis was performed on a sample of about 1 fb^{-1} integrated luminosity from the 2004-2005 KLOE data campaign.

Dedicated Ntuples were produced for the presented studies, in which charged kaons are identified using two-body decay ($K^\pm \rightarrow \mu^\pm \nu$ or $K^\pm \rightarrow \pi^\pm \pi^0$) and/or the dE/dx (the kaon identification is made by means of the ionization in the drift chamber gas) TAG mechanisms.

All the available information, about each event contained in the Ntuples, comes from the KLOE standard reconstruction software [40] and is organized in blocks, namely vertices and tracks (TRK, TRKV, VTX), dE/dx (DEID and DEDX), the calorimeter block (CLU), the information relative to the tagging (DESEL and TAG blocks).

Monte Carlo (MC) simulations of different physical processes involved in the observed events, with K^- absorption occurring on Carbon and Helium in different volumes of the KLOE apparatus were performed, with the aim of optimizing the

analysis cuts, for data interpretation and fitting purposes. The details of the calculations and of the simulation procedure will be described case by case, see sections 4.3 and 5.3. MC Ntuples contain the same blocks listened for data, together with the TRUE MC block which proved to be extremely useful. The true MC block contains geometric and kinematical information about all the particles originally generated in the event (Σ^0 , π^0 and their decay products for signal simulated events) not affected by the KLOE reconstruction procedure.

Motivated by requirements of CPU time, smaller size data Ntuples were created to shorten the analysis jobs, containing only pre-selected events. Each event of the final selected Ntuples is required to contain an identified Λ decay vertex, as will be specified in the following sections, together with at least three neutral clusters.

After the Ntuples were created, the refined event selection procedure started. In the following sections the selection criteria are reported.

3.3 $\Lambda(1116)$ identification

The presence of a $\Lambda(1116)$ hyperon always represents, for the $\Sigma^0\pi^0$ channel under consideration, the signature of K^- hadronic interaction.

In order to identify Λ s produced in the DC volume and DC entrance wall, we used the KLOE standard software to reconstruct the vertex for the Λ decaying into charged particles:

$$\Lambda \rightarrow p + \pi^- \quad (BR = 63.9 \pm 0.5)\%$$

KLOE uses a coordinate system where z is the bisector of the electron and positron beams, x and y define the transverse plane, ρ is the radial distance.

The lambda vertex candidate is requested to fulfill the following conditions:

- vertex with at least two opposite curvature tracks,
- the spatial position of the vertex must be inside the DC volume or in the DC entrance wall,
- the negative track (π^- candidate) is required to have $dE/dx < 95$ ADC counts.

These requirements are easily fulfilled by a large number of events, mostly because we deal with a copious background from the three-body decay of K^\pm ($K^\pm \rightarrow \pi^\pm \pi^\pm \pi^\mp$).

In order to reduce this background and to remain with a clean sample we had to refine the search criteria for the proton. We then looked for positive tracks with an associated cluster in the calorimeter. The signature of a proton in the calorimeter is then cleanly identified, since the corresponding signal is well-separated by the signal generated by the pions. As an example in figures 3.1 and 3.2 are represented the relationships between the momentum of a positive particle and the energy deposited in the associated calorimeter cluster, for clusters in the calorimeter barrel and endcaps respectively. Most of the minimum ionizing particles were removed from figures 3.1 and 3.2 by requiring $dE/dx > 95$ ADC counts, in order to be able to observe more clearly the proton signal and to tune our selection criteria.

Taking into account the signature of protons in this plot, we included in our selection an additional requirement for the positive track, that must have an associated cluster in the calorimeter with an energy such as to fulfill the criteria:

- if the track of momentum p_{tr} (in MeV/c) has an associated cluster of energy E_{cl} (in MeV) in the barrel:
 1. $E_{cl} < 150$
 2. $E_{cl} < 0.714(p_{tr} - 150)$
 3. $E_{cl} > 0.833(p_{tr} - 350)$
- for clusters in the endcaps:
 1. $E_{cl} < 150$
 2. $E_{cl} < 0.714(p_{tr} - 250)$
 3. $E_{cl} > 0.833(p_{tr} - 400)$

The momentum spectrum of the selected protons is shown in figure 3.3 (left), together with their dE/dx distribution. A lack of low momentum protons is evident (for momenta lower than $p \sim 250 MeV/c$) due to the lower efficiency of the calorimeter for low kinetic energy protons. Low momentum protons are absorbed in lead before interacting, and producing secondaries, their signal is then too small to be observed.

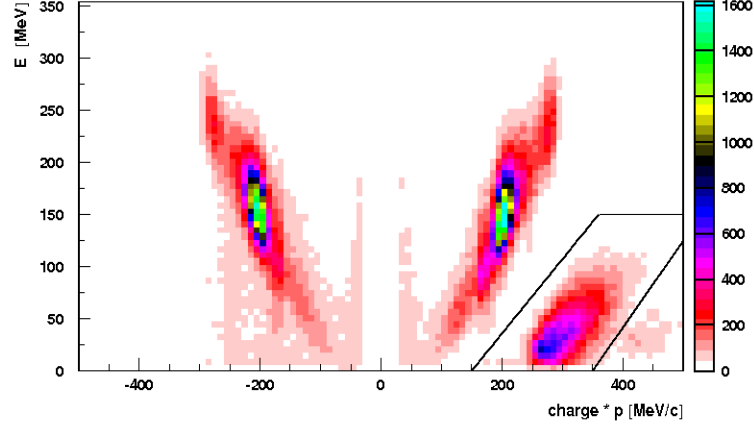


Figure 3.1: Bidimensional plot showing the energy of the cluster in the EMC barrel vs. the momentum of the associated track (multiplied by its charge). The signature of a proton candidate in this plot is contained in the region delimited by the black lines, parametrized in the text. Minimum ionization particles (with dE/dx in DC < 95 ADC counts) have been excluded from the plot.

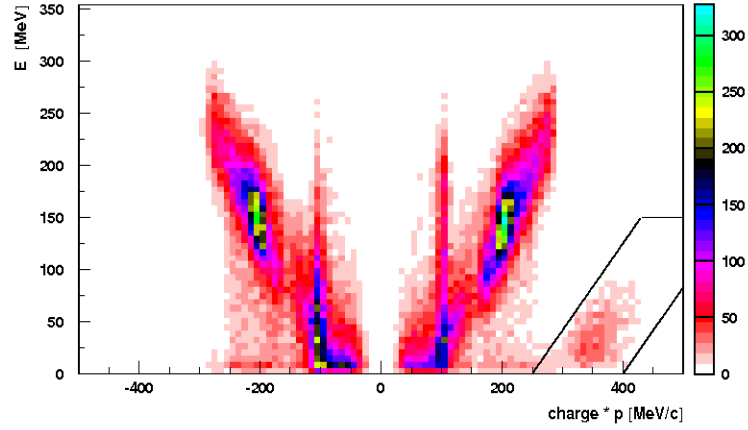


Figure 3.2: The same plot as in Fig. 1, but for clusters in the EMC endcaps.

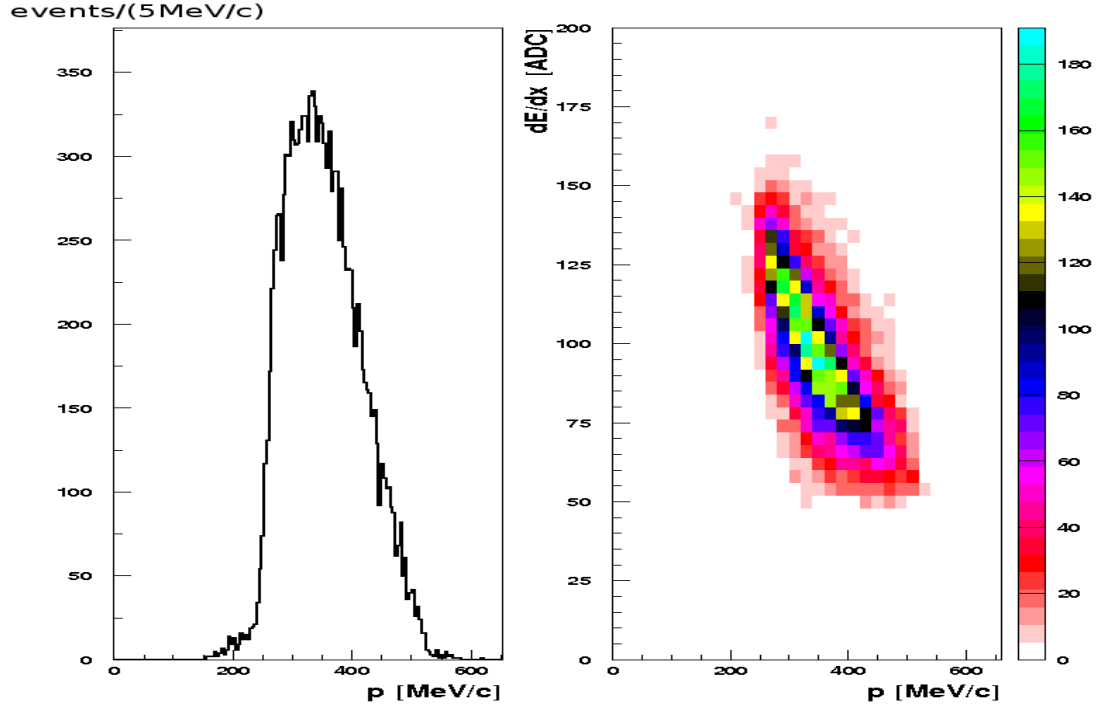


Figure 3.3: Momentum spectrum of the selected proton candidates with a cluster in the EMC associated to the track (left), also viewed vs. the dE/dx in the DC (right).

In order to correct for this effect, we had to retain those positive tracks which have the last DC measurement “near” the calorimeter (reaching it) but do not have an associated cluster. To this end we used the information provided by the DC itself, i.e. the energy loss in the DC, to separate the protons with low momenta from pions, optimizing a cut on dE/dx using the identified protons with signature in the calorimeter (see Fig. 3.3). We were tuning the cut on these protons and then applied the cut to all protons, i.e. including those which have no associated cluster in the calorimeter. The cut is shown in Fig. 3.4, in which the momentum and dE/dx of the finally selected protons are plotted.

The black function in the bidimensional plot shows the selection criteria, dE/dx for proton candidates must satisfy the relation

$$dE/dx > A - Bx + Cx^2$$

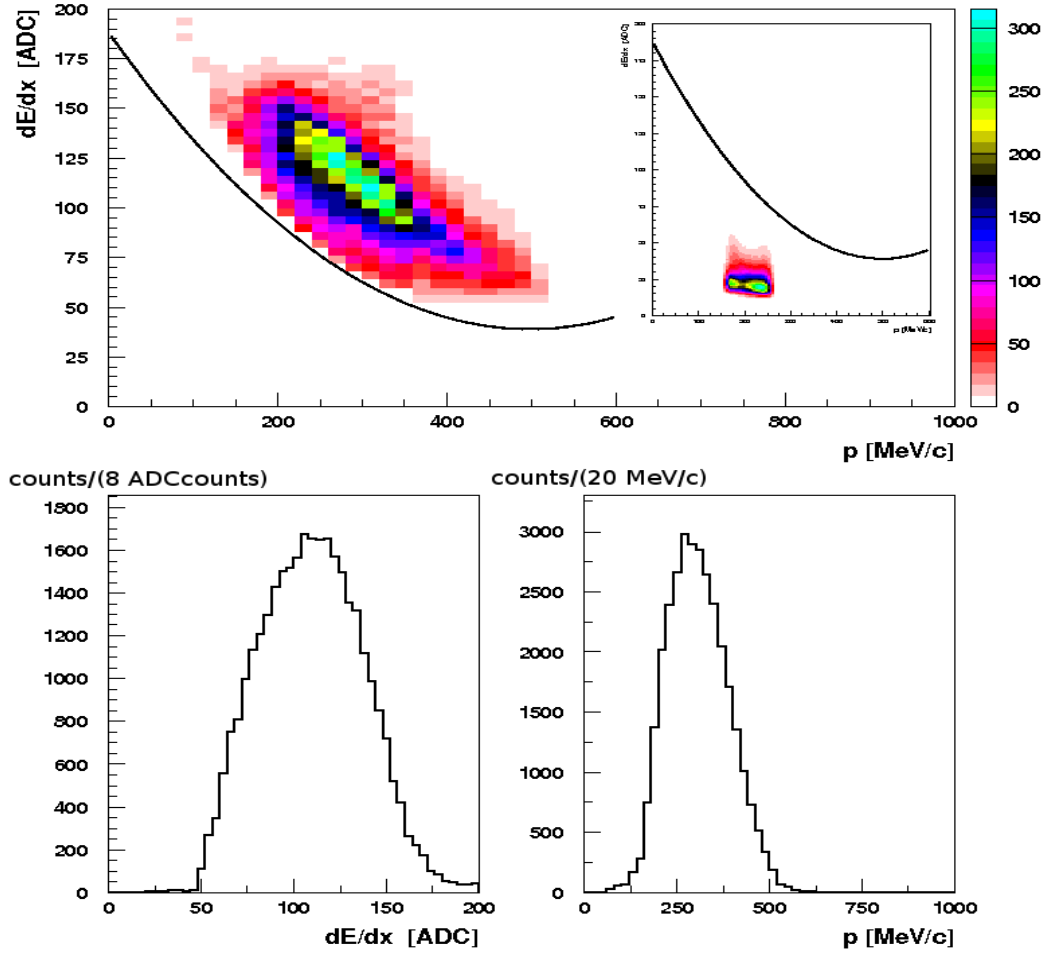


Figure 3.4: Bidimensional plot (top) of the momentum of the protons (x) vs. dE/dx (y) in the DC for the final selection (protons with + protons without associated cluster). The bottom plots shows the corresponding projections (left: dE/dx , right: momentum). In the top right part, pions from 2-Body decay are shown for comparison.

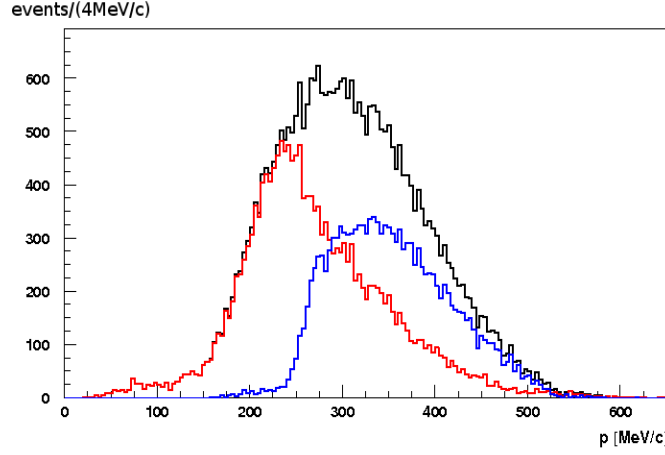


Figure 3.5: Momentum spectra of selected positive tracks with (blue) and without (red) cluster associated in the EMC. Also the total momentum distribution is shown in black.

with:

$$dE/dx \text{ [ADC]}$$

$$x = \frac{p}{MeV} - 40$$

$$A = 165 \text{ [ADC]}$$

$$B = 0.55 \text{ [ADC]}$$

$$C = 0.0006 \text{ [ADC]}$$

This cut was optimized in order to reject positive pions contamination. Inserted in the top right part of the same picture (Fig. 3.4) we see the typical signature of pions in dE/dx and momentum. In this case we plotted those π^+ which come from the 2-body decay $K^+ \rightarrow \pi^+\pi^0$. This illustrates how the chosen cut is enough for rejecting π^+ in a wide range of momentum.

We show in Fig. 3.5 the difference in the momentum spectra between the protons not having an associated calorimeter cluster (red line) and those who do (blue line). Notice that these two distributions are not normalized, so we finally select $\sim 56\%$ of pairs without a cluster assigned to the proton. As clearly resulting

from the figure, the spectrum of positive tracks identified as protons extends now to lower momenta - as low as 25 MeV/c.

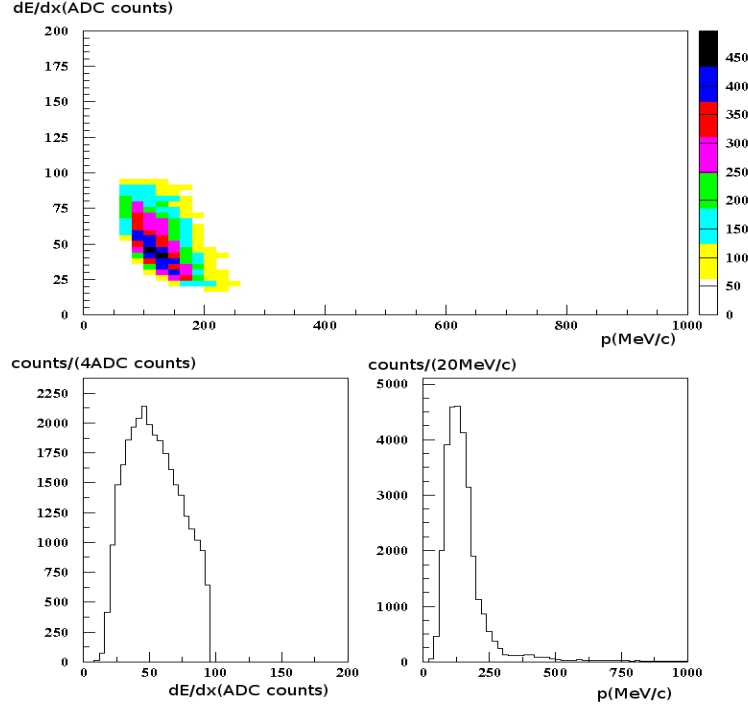


Figure 3.6: Bidimensional plot of the momentum (x) vs. dE/dx (y) and corresponding projections as in Fig. 3.4, for the selected negative pions.

In Fig. 3.6 also the characteristics of the negative particle (pions) of the vertices included in the final selection are shown.

As a final step for the identification of true Λ decays the vertices are cross checked with quality cuts, using the minimum distance between tracks and the chi-square of the vertex fit as well.

The invariant mass of the $\Lambda(1116)$ is finally calculated under the p and π^- mass hypothesis

$$m_{p\pi^-} = \left[\left(\sqrt{m_p^2 + p_p^2} + \sqrt{m_\pi^2 + p_\pi^2} \right)^2 - (\mathbf{p}_p + \mathbf{p}_\pi)^2 \right]^{\frac{1}{2}}. \quad (3.1)$$

In figure 3.7 the $m_{p\pi^-}$ invariant mass spectrum for the selected vertices is shown.

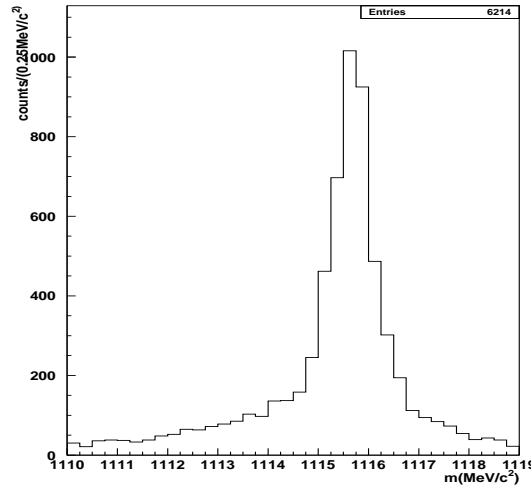


Figure 3.7: $m_{p\pi^-}$ invariant mass spectrum.

The following cut is finally applied on $m_{p\pi^-}$

- $m_{p\pi^-}$ must lie between 1114 and 1117 MeV/c^2 .

Even if the introduced background of accidental pairs lying under the lambda invariant mass is still considerable, we keep these events in the analysis chain since the additional requirements that will be introduced and explained in the next sections (namely the presence of a photon and a π^0 in time from the Λ decay vertex) eliminates the background events almost completely.

3.4 Spatial distribution of the selected events

The spatial distribution of the vertices for the Λ -candidate events selected by the procedure explained in 3.3 is shown in two bidimensional plots (radial position vs. Z and projections X vs. Y) in Fig. 3.8. As it can be noticed in both distributions, a big number of events is coming from the DC entrance wall.

Originally, our aim was to look for Λ s coming exclusively from K^- absorptions in the gas filling the Drift Chamber volume (we refer to section 4.1 for motiva-

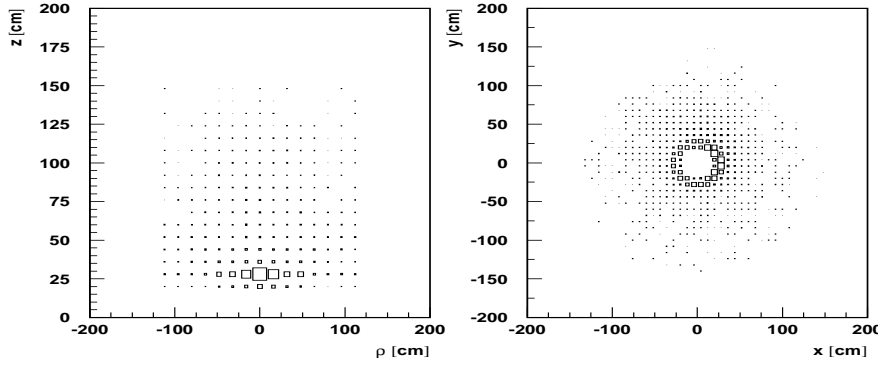


Figure 3.8: Spatial distribution of selected events' vertices. Radial position vs. Z (left) and X projections vs. Y (right)

tions). Nevertheless, taking into account for the very good and important first hand physics which might be done with kaons absorbed in Carbon (main component of DC entrance wall) and the importance of the physical case of the $\Lambda(1405)$, we enlarged our acceptance in ρ_Λ down to a lower value of $\sim 23\text{cm}$. In this way the DC entrance wall is included in our fiducial volume.

The effect of energy loss suffered by charged particles when crossing the wall material, and its consequences on the resolution and shape of the corresponding invariant mass and momentum distributions will be described case by case, based on dedicated MC simulations.

3.5 Extra p tracks and interaction vertex extrapolation

We will describe in section 5.7 the search for an extratrack associated to the $K^- "p"$ hadronic interaction vertex, when a $\Sigma^0\pi^0$ event is identified. The interaction vertex coincides with the $\Sigma^0\pi^0$ production vertex. In what follows the extrapolation

procedure for the hadronic interaction vertex will be shown, performed searching for an extra proton related to the Λ decay vertex. The probability of the presence of an extra proton is high, as a consequence of the Σ internal conversion and K^- multinucleon absorption processes, whose consequence is a partial, or total, fragmentation of the target nucleus. In Helium the Σ internal conversion probability is $\sim 50\%$, the multinucleon absorption accounts for $\sim 20\%$ of all the absorptions.

Once the Lambda decay vertex has been reconstructed, another proton (correlated with the Λ vertex) is searched among the other positive tracks in the chamber. Protons identified by the dE/dx (following the same selection criteria as for the protons from the lambda decay, and the extra requirement for the length of the track to be higher than $50cm$) are kept for further analysis. The point of closest approach between the backwards extrapolation of the selected track and a straight line corresponding to the Lambda is searched for.

In this way an interaction vertex is defined when the minimum distance between the track and lambda extrapolations is smaller than $2cm$, and the found decay path of the lambda is less than $7cm$. The distance between the lambda decay vertex and the interaction vertex reflects correctly the exponential lambda decay pattern, within the expected resolution, as can be seen in the figure 3.9.

In figure 3.10 (left) the radial position ρ_Λ of the Λ decay vertex is shown. Starting from 30 cm of ρ_Λ , taking into account for the Λ decay path, interactions are considered to occur in the gas filling the DC volume (plotted in red). This is confirmed in the figure on the right, representing the radial position of the interaction vertex for events with ρ_Λ lower (black) or higher (red) than 30 cm . The former presents the expected Gaussian shape as should correspond to events coming from interactions in the DC wall. Both figures can be seen in more detail in the insets.

The cut at 30 cm was checked with a Monte Carlo in which interactions only inside the DC wall were generated. For this simulation only a small number of events (0.4%) was reconstructed with $\rho_\Lambda > 30cm$, while in the real data this fraction accounts for more than 10% .

For the selected Λp events, a check in the mass of the proton track can be done if it is associated with a cluster in the calorimeter, and one of the two particles from the lambda decay has an associated cluster as well. For the selected protons (either for protons from the lambda decay or protons created in the original interaction),

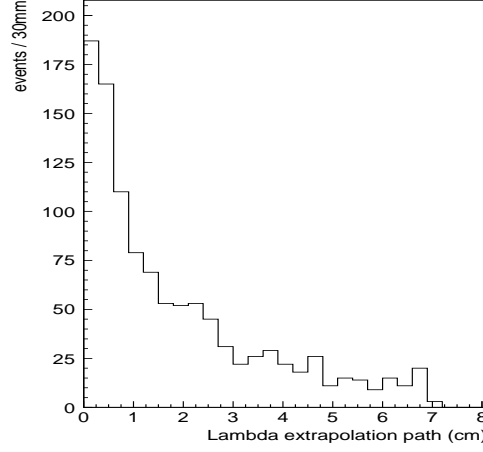


Figure 3.9: Lambda decay path for Λp events in the DC volume (see definition in the text).

a cluster is found in about 50% of the cases. To calculate their mass by time of flight, since we did not require the presence of the track of the interacting K^- , we use the time of the cluster (t_{cl}) of the lambda decay product, and define the interaction time (t_i) as:

$$t_i = t_{cl} - \frac{path_t}{v_t} - \frac{path_l}{v_l}, \quad (3.2)$$

with $path_t$ being the total length of the particle track (taking into account the extrapolations backward to the lambda decay vertex and forward to the cluster centroid), $path_l$ is the extrapolated path for the lambda, and v_t and v_l the corresponding velocities. With this interaction time t_i , and knowing the $path_p$ for the proton track, and the time of its associated cluster t_p , the mass of the particle can be calculated with the information of the proton momentum p_p and its velocity v_p :

$$m = p_p \cdot \sqrt{\frac{1}{v_p^2} - \frac{1}{c^2}} \quad (3.3)$$

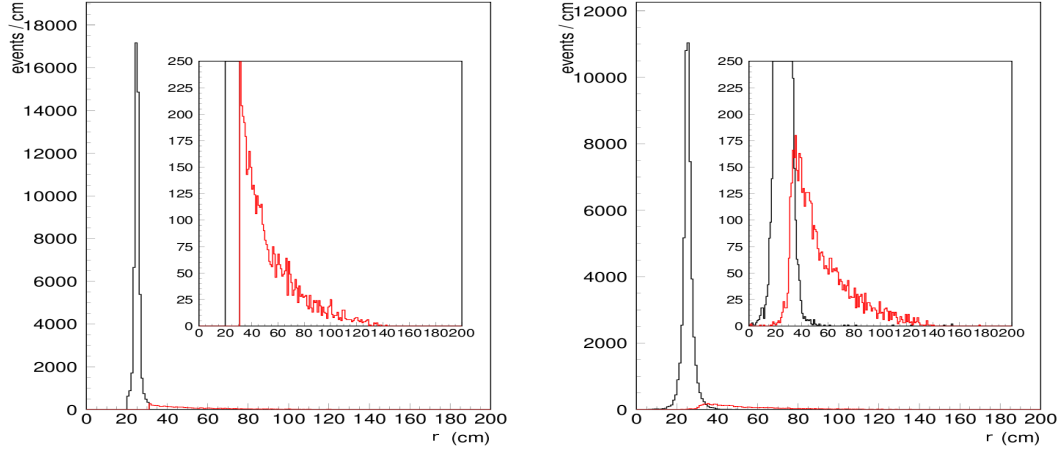


Figure 3.10: Radial position distributions of ρ_Λ (left) and of the interaction vertexes (right). The inserted pictures show the detail of the events produced inside the DC volume.

This mass distribution is shown in figure 3.11, where a clear enhancement at the proton mass value is seen, almost background free.

Next step of the $\Sigma^0\pi^0$ events selection will be the identification of three photon clusters in the KLOE calorimeter.

3.6 Photons cluster selection

The selection of $\Sigma^0\pi^0$ events proceeds, after the $\Lambda(1116)$ identification, with the selection of three photon clusters. We will indicate as γ_3 the photon coming from the Σ^0 decay, γ_1 and γ_2 will represent photons from π^0 decay according to the reaction

$$K^-p \rightarrow \Sigma^0\pi^0 \rightarrow (\Lambda\gamma_3)(\gamma_1\gamma_2) \rightarrow (p\pi^-)\gamma_1\gamma_2\gamma_3 \quad (3.4)$$

where " p " represents a bound proton in a nucleus.

First a cycle over all neutral clusters (clusters with no associated tracks in the

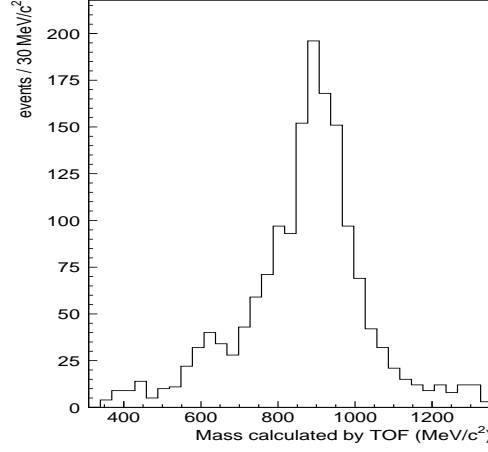


Figure 3.11: Mass calculated by time of flight for the proton tracks.

DC) is performed. We define the variable N_n which represents the number of neutral clusters in the calorimeter whose energy E_{cl} is greater than 20MeV . The clusters are discarded if they are associated to photons from K^+ two body decay ($K^+ \rightarrow \pi^+\pi^0$) (events in which a K^- is tagged by two body decay are of course excluded). The event is rejected if $N_n < 3$.

Three photon clusters are identified among the N_n s by time of flight. At this end a pseudo chi-square variable was calculated for each couple of clusters (among the N_n s) $\chi_t^2 = t^2/\sigma_t^2$ searching for three photons in time from the decay vertex position of the $\Lambda(1116)$ (\mathbf{r}_Λ). We introduced the quantity $t = t_i - t_j$, where the interaction times (t_i, t_j) are defined as the difference between the cluster time, and the time-of-flight in the hypothesis that the particle is a photon ($v = c$), in formulae

$$t_i = t_{cli} - \frac{r_i}{c} \quad (3.5)$$

$$r_i = \sqrt{(x_\Lambda - x_{cli})^2 + (y_\Lambda - y_{cli})^2 + (z_\Lambda - z_{cli})^2}. \quad (3.6)$$

The standard uncertainties reported in 2.3.2 and 2.3.1 on the measured positions

and times were used for the σ_t calculation.

The three couples are selected among N_n which minimize χ_t^2 and a check is made that each selected cluster appears two times in the three couples. According to dedicated pure signal MC simulations (see sections 4.3 and 5.3 for details on the simulation procedure) a cut was optimized on this first chi square variable, the event is only retained if $\chi_t^2 \leq 20$.

3.7 Photons cluster identification

Once the three candidate photon clusters are chosen we must assign them to the triple of photons $(\gamma_1, \gamma_2, \gamma_3)$. To this end a new pseudo chi-square variable $\chi_{\pi\Sigma}^2$ is calculated, based, for a better distinction power, on the combined invariant masses of Σ^0 and π^0 . $\chi_{\pi\Sigma}^2$ is defined as follows:

$$\chi_{\pi\Sigma}^2 = \frac{(m_{\pi^0} - m_{ij})^2}{\sigma_{ij}^2} + \frac{(m_{\Sigma^0} - m_{k\Lambda})^2}{\sigma_{k\Lambda}^2} \quad (3.7)$$

where the index $(i, j$ and $k)$ represents one of the previously selected candidate photon clusters. With m_{ij} and $m_{k\Lambda}$ we mean the invariant mass of two photon clusters, and the invariant mass of the third photon with the $\Lambda(1116)$ respectively. σ_{ij} is the resolution on the invariant mass of two photons m_{ij} :

$$\sigma_{ij} = \frac{m_{ij}}{2} \left[\frac{\sigma_{Ecli}}{E_{cli}} \oplus \frac{\sigma_{Eclj}}{E_{clj}} \right] \quad (3.8)$$

The two photons invariant mass is dominated by the calorimeter energy resolution (given in in 2.3.2) while the angle measurement gives a negligible contribution. $\sigma_{k\Lambda}$ represents the analogous resolution for the invariant mass of the third photon with the $\Lambda(1116)$, whose more complicated expression also involves the resolution of the KLOE DC for the momentum of the charged particles (see section 2.3.1).

$\chi_{\pi\Sigma}^2$ is calculated for each possible combination and the minimizing triple is selected. An optimized cut based on pure signal MC simulations was also applied on this second pseudo chi-square, the event is retained if $\chi_{\pi\Sigma}^2 \leq 45$.

By employing the true MC information about the three identified photons, it was found that the algorithm has an efficiency of $(98 \pm 1)\%$ in recognizing photon clusters and an efficiency of $(78 \pm 1)\%$ in distinguishing the right $\gamma_1\gamma_2$ couple (from

π^0 decay) from γ_3 , both for K^- absorptions in the DC wall and the DC gas. The good resolution power of the algorithm is pictorially represented in figure 3.12 (pure signal $\Sigma^0\pi^0$ MC events left and data right) with the following colour legend:

- in black the invariant mass m_{ij} for each couple of clusters selected by χ_t^2 ,
- in green the invariant mass m_{12} of the photons $\gamma_1 - \gamma_2$ selected by $\chi_{\pi\Sigma}^2$,
- in red the invariant masses m_{13} and m_{23} of the "wrong" couples.

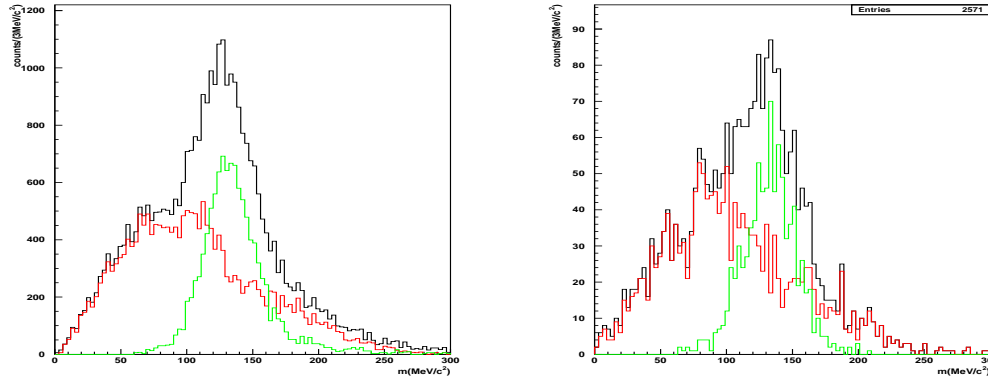


Figure 3.12: The plot illustrates the invariant mass of various combinations of three photons, as explained in the text, for pure signal MC events left and data right.

The data sample used in 3.12 refers to K^- absorptions in gas. A good agreement of data with simulation appears and a clean separation of the green π^0 peak.

3.8 Cluster splitting and background rejection

A usual background source in KLOE data analysis when treating π^0 s is the cluster splitting, namely single clusters in the calorimeter are erroneously recognized as two clusters. Such clusters, if present, would certainly pass the χ_t^2 test as they would be identified as two photons in time from \mathbf{r}_Λ . To explore this possible background we followed a standard procedure and represented for each couple $\gamma_1 - \gamma_2$ the distance R between the clusters as a function of the sum of their

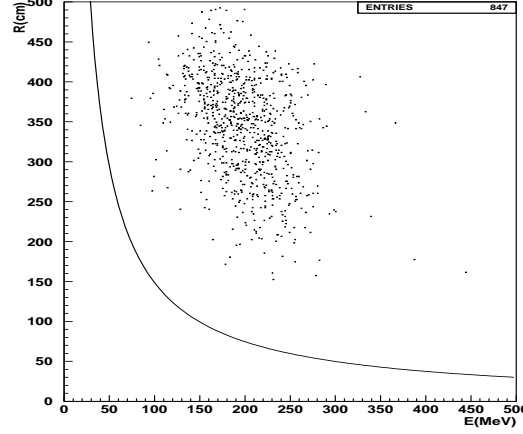


Figure 3.13: Plot representing R as a function of E as described in the text.

energy $E = E_{\gamma_1} + E_{\gamma_2}$. The resulting distribution is shown in figure 3.13 for the selected sample of $\Sigma^0\pi^0$ events, following K^- absorption in the DC entrance wall, together with the relation $R(E)$ which is usually used to distinguish splitted clusters (or machine background), the acceptable clusters lying above the curve. As clearly shown by figure 3.13 this background does not affects the sample of selected π^0 s. The cut corresponding to the continuous line in figure 3.13:

$$R \geq \frac{a}{E_{\gamma_1} + E_{\gamma_2} + b} \quad \text{where } a = 15000 \text{ MeV cm and } b = 1 \text{ MeV} \quad (3.9)$$

is nevertheless also applied to the final selected π^0 samples.

A last cut is performed based on the $m_{\Sigma^0} - m_{\pi^0}$ scatterplot. The pion and sigma invariant masses are calculated as follows:

$$m_{\gamma_1\gamma_2} = \sqrt{2 E_{\gamma_1} E_{\gamma_2} (1 - \cos\theta_{\gamma_1\gamma_2})} \quad (3.10)$$

where $\cos\theta_{\gamma_1\gamma_2} = (\mathbf{p}_{\gamma_1} \cdot \mathbf{p}_{\gamma_2}) / (p_{\gamma_1} p_{\gamma_2})$

$$m_{\Lambda\gamma_3} = \sqrt{m_{\Lambda}^2 + 2 E_{\gamma_3} E_{\Lambda} - 2 p_{\Lambda} p_{\gamma_3} (1 - \cos\theta_{\Lambda\gamma_3})} \quad (3.11)$$

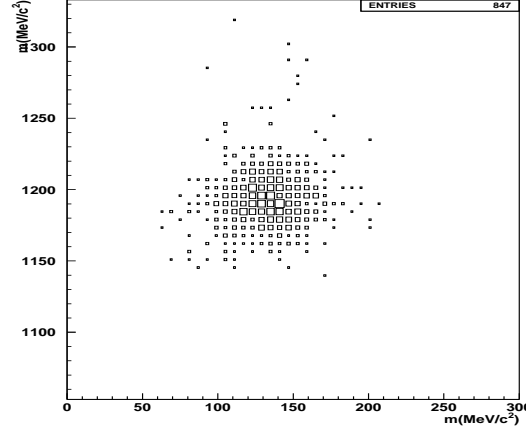


Figure 3.14: Plot representing $m_{\Lambda\gamma_3}$ as a function of $m_{\gamma_1\gamma_2}$.

where $\cos\theta_{\Lambda\gamma_3}$ is the angle between the Λ momentum and the γ_3 momentum in the laboratory frame. E_Λ and \mathbf{p}_Λ are obtained from energy and momentum conservation, m_Λ is the obtained proton pion invariant mass as described in equation 3.1. The $m_{\Lambda\gamma_3} - m_{\gamma_1\gamma_2}$ scatterplot is shown in figure 3.14

To conclude the following cut is imposed on the combined Σ^0 and π^0 invariant masses:

$$(m_{\Lambda\gamma_3} - m_{\Sigma^0})^2 + (m_{\gamma_1\gamma_2} - m_{\pi^0})^2 < (60\text{MeV}/c)^2 \quad (3.12)$$

3.9 $m_{\Lambda\gamma_3}$ invariant mass

At this stage the identification of each particle is completed. The invariant mass of the Σ^0 is obtained combining the information (energy and position) of the cluster associated to γ_3 with the momentum of the $\Lambda(1116)$ as described in section 3.8. In figure 3.15 is shown the obtained invariant mass $m_{\Lambda\gamma_3}$ in black with error bars (for absorptions in the gas), together with a Gaussian fit. The fit gives a mean mass $m_{\Lambda\gamma_3} = 1192.8 \pm 0.6\text{MeV}/c^2$ where the PDG value is $m_{\Sigma^0} = 1192.642 \pm 0.024\text{MeV}/c^2$. The resolution in the $m_{\Lambda\gamma_3}$ invariant mass is $\sigma_{m_{\Lambda\gamma_3}} \sim 15\text{MeV}/c^2$,

the enlargement is not due to a misidentification of the neutral clusters, but to the calorimeter resolution. This clearly results from figure 3.16 representing the $m_{\Lambda\gamma 3}$ distribution for a sample of pure signal $\Sigma^0\pi^0$ MC events, following K^- absorptions in Helium, as will be described in 5.3:

$$K^- He \rightarrow \Sigma^0 \pi^0 {}^3H. \quad (3.13)$$

The tracks and clusters selection follows the procedure described in this chapter, but true MC information is employed for the momentum of the photon $\mathbf{p}_{\gamma 3}$. Figure 3.16 shows that the observed resolution in the $m_{\Lambda\gamma 3}$ spectrum is mainly influenced by the calorimeter resolution. Resolution studies on the final $\Sigma^0\pi^0$ mass and momentum, described in section 5.5, will confirm such result.

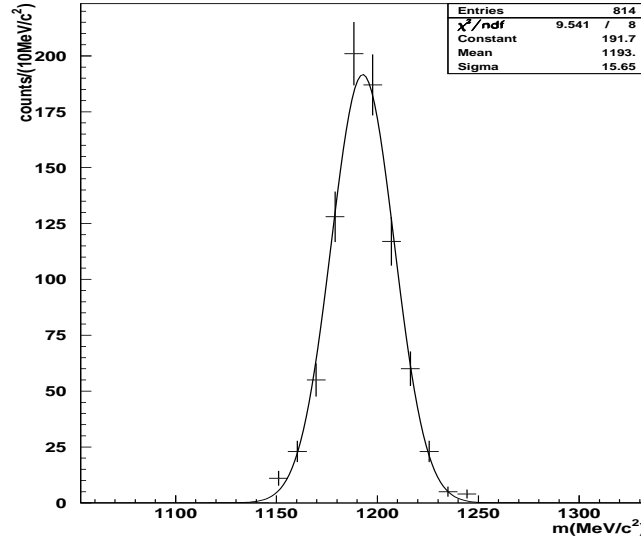


Figure 3.15: Plot representing the $m_{\Lambda\gamma 3}$ invariant mass distribution with error bars, together with a Gaussian fit.

It is important to stress that when the photon identification algorithm (χ_t^2 and $\chi_{\pi\Sigma}^2$) is applied to simulated events, employing the true MC information on photons' energy, the discrimination efficiency between the photons of the triple

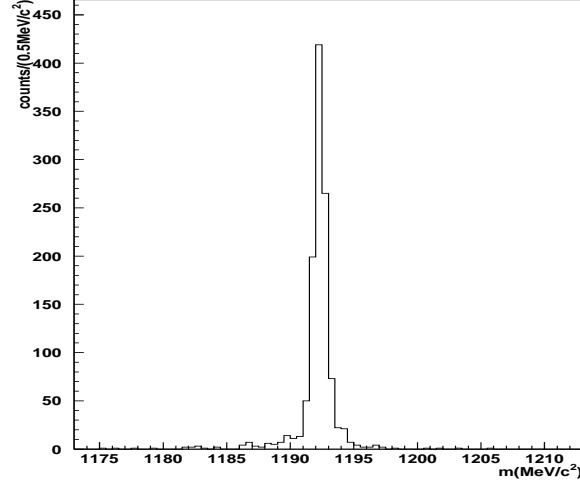


Figure 3.16: Plot representing the $m_{\Lambda\gamma_3}$ invariant mass spectrum obtained with true MC information on \mathbf{p}_{γ_3} .

$(\gamma_1, \gamma_2, \gamma_3)$ is $\sim 100\%$. The small misidentification source is then to be ascribed to the calorimeter energy resolution and to the overlap of the photons energy in a wide energy range (see section 5.8.1).

Chapter 4

Study of K^- absorption in the KLOE drift chamber entrance wall

4.1 Introduction

In this section it will be described the analysis of K^- nuclear interactions in the DC entrance wall, giving rise to a $\Sigma^0\pi^0$ pair in the final state. The analysis of K^- absorptions in the material of the DC entrance wall was treated with care, because of the lower expected resolution in p_p and p_{π^-} , as a consequence of the charged particles energy loss in crossing the wall. The degrading in invariant mass and momentum resolution (and the shift) will be described in this chapter and turns out to be not prohibitive for our purposes (being the broadening in $m_{\Sigma^0\pi^0}$ and $p_{\Sigma^0\pi^0}$ mainly dominated by the resolution of the calorimeter). On the other side the study of K^- absorptions in Carbon (main component of the wall) turned to be fundamental for the following reasons:

- As described in section 1.3.1 both theoretical calculations [27] and experiments [28; 29] suggest that atomic K^- nuclear capture on Carbon is likely to occur on a single proton at the surface of the nucleus. In this chapter a missing mass study will be presented whose results are in agreement with this picture.
- Analyzing K^- capture on Carbon we have the possibility to compare our results to analogous emulsion experiments (described in section 1.3.1, char-

acterized by higher resolution for the $\Sigma^\pm\pi^\mp$ invariant mass and momentum distribution, but lower statistics) in which the reported $p_{\Sigma^\pm\pi^\mp}$ and p_{π^\mp} distributions helped us in understanding the peculiar structure of our $p_{\Sigma^0\pi^0}$ spectrum and to roughly distinguish events in flight from captures at rest.

- The gas filling the KLOE DC is a mixture (10% in volume C_4H_{10} , 90% in volume ^4He) so that the "contamination" of absorptions in Carbon (with respect to Helium) can not be neglected. The knowledge of the spectral shapes for Carbon events turns then to be fundamental to the aim of a clear understanding of K^- nuclear interactions in the DC gas.

4.2 Composition of the drift chamber entrance wall

The KLOE DC is internally delimited by an aluminated fiber cylinder with a radius of 25cm. The DC entrance wall composition is 750 μm of Carbon fibre and 150 μm of aluminium foil.

Dedicated GEANT MC simulations of the KLOE apparatus (taking realistically into account for each material: beryllium beam sphere, air, DC entrance wall, gas filling the DC and DC wires) were performed to estimate the percentages of K^- absorptions in various materials (the K^- absorption physics treated by the GHEISHA package). For what concerns K^- captures in the DC entrance wall, according to the MC simulations, out of the total captured kaons, about 81% are captured in the Carbon fibre component and the residual 19% in the aluminium foil.

As will be described in section 4.4 the resolution in the r_Λ position determination (together with the decay path of the $\Lambda(1116)$) makes impossible to distinguish absorptions in the Al foils from captures in Carbon fibre. As a consequence, also considering the low percentage of Al expected events, we will be forced to neglect such contamination when treating absorptions in the DC entrance wall.

Pushed by the interesting results outlined in this Chapter, and the opportunity offered to the AMADEUS/KLOE collaboration of two months beam time on DAΦNE (November-December 2012) a high purity Carbon target (graphite) was realized in summer 2012 and installed inside the KLOE DC. The results of preliminary analysis on part of this data set will be presented in section 4.9.

Before turning to the details of the geometrical cuts introduced for the selection of absorptions in the wall, we will spend some words on the MC simulation of quasi-free $\Sigma^0\pi^0$ events, whose true MC related information was used for resolution estimates.

4.3 MC simulation of $\Sigma^0\pi^0$ production in the DC entrance wall

The resolution studies for the various kinematical variables were performed employing the true MC routine. As already mentioned, the true MC routine contains geometric and kinematical information about all the particles originally generated in the event (in this case Σ^0 and π^0 and their decay products) not affected by the KLOE reconstruction procedure. In order to obtain model independent estimates of the available resolution, quasi-free (non-resonant) $\Sigma^0\pi^0$ production, following K^- absorptions in the different nuclear targets and various materials of the KLOE setup, were simulated. In particular, for what concerns the present study of K^- interaction in the DC entrance wall, we will describe the adopted procedure for K^- capture in Carbon from the DC wall.

The first step of the simulation is the calculation of Σ^0 and π^0 momenta. In this case a non-resonant quasi-free reaction is taken into account, in which K^- interacts with a single bound proton and the residual ^{11}B is left in its ground state, behaving like a spectator. Final state interaction was neglected:

$$K^- C \rightarrow \Sigma^0 \pi^0 {}^{11}B. \quad (4.1)$$

The momentum of each particle in the final state is simply obtained by imposing momentum conservation. For reactions at rest the initial momenta are given by:

$$\mathbf{p}_k = \mathbf{0}$$

$$\mathbf{p}_p = \mathbf{p}_F$$

$$\mathbf{p}_B = -\mathbf{p}_F$$

where \mathbf{p}_F represents the Fermi momentum of the bound proton in the nucleus. Then momentum conservation imposes

$$\mathbf{p}_{\Sigma^0\pi^0} = \mathbf{p}_{\Sigma^0} + \mathbf{p}_{\pi^0} = -\mathbf{p}_B. \quad (4.2)$$

The mass distribution $m_{\Sigma^0\pi^0}$ of the non-resonant event is then obtained by energy conservation:

$$m_k + m_{He} = \sqrt{m_{\Sigma^0\pi^0}^2 + p_{\Sigma^0\pi^0}^2} + \sqrt{m_B^2 + p_B^2} \quad (4.3)$$

that is

$$m_{\Sigma^0\pi^0} = \sqrt{(m_k + m_{He})^2 + m_B^2 - 2(m_k + m_{He})\sqrt{m_B^2 + p_B^2}} \quad (4.4)$$

with analogous generalizations for the case of capture in flight $\mathbf{p}_k \neq \mathbf{0}$. As the interaction is assumed to occur on the last bound proton $p_{\frac{3}{2}}$, the Fermi momentum distribution that competes to the $1p$ orbital of the ^{12}C nucleus (as reported in [41]) was adopted.

The kinematics of the events is then saved in a file which represents the input for the hadronic interaction (masses and momenta of the $\Sigma^0\pi^0$ couples to be generated). Only charged kaon events are generated for our purposes (similarly only K charged Ntuples of data are considered). The K^- is "killed" in the DC entrance wall, for our purposes in this chapter, and a $\Sigma^0\pi^0$ pair is generated with the momenta assigned by the input kinematics file. The influence of the energy loss on the helix described by the charged particles trajectory (from Σ^0 decay) in crossing various materials of the KLOE setup is taken into account. Next steps of the simulation are the reconstruction of the generated event in KLOE, and, finally, the creation of the Ntuple.

As an example in figure 4.1 is shown the invariant mass $m_{\Sigma^0\pi^0}$ for simulated quasi-free non resonant events, generated at rest (left) and in flight (right). The black curve is MC true while the red curve represents the distribution corresponding to reconstructed events (the green curve represents the $m_{\Sigma^0\pi^0}$ distribution obtained with the mass hypothesis for the identified Σ^0 and π^0) according to the specifications given in chapter 3.

Let us notice in particular the sharp cut of the black distribution (left) in correspondence of the kinematical limit for K^- absorptions at rest in Carbon ($\sim 1416 \text{ MeV}/c^2$). The kinematical limit is shifted to higher values when the interaction occurs in flight ($\sim 1433 \text{ MeV}/c^2$) (see figure 4.1 right).

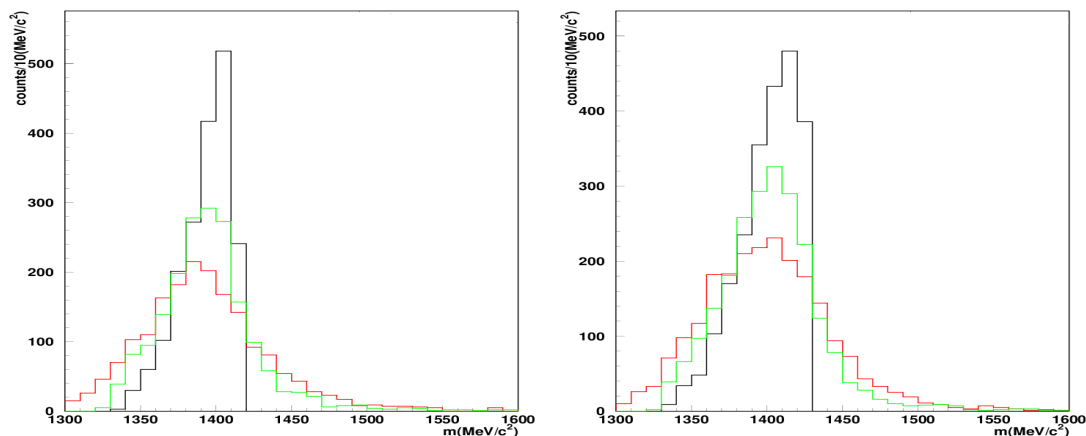


Figure 4.1: $m_{\Sigma^0\pi^0}$ spectrum for simulated quasi-free non resonant events generated at rest (left) and in flight (right), black curve is MC true while the red curve corresponds to reconstructed events (the green curve represents the $m_{\Sigma^0\pi^0}$ distribution obtained with the mass hypothesis for the identified Σ^0 and π^0).

4.4 Resolution in ρ_Λ and p_Λ determination

Applying the same event selection described in Chapter 3 for data to the non-resonant quasi-free MC generated events, we can estimate the resolution in the momentum and radial decay vertex position of the reconstructed Λ s. The results are summarized in table 4.1 where the numbers correspond to simple Gaussian fits to the distributions of the originally generated true-MC quantities subtracted by the reconstructed ones, event by event, leaving the tails due to energy loss out of the fit. The corresponding distributions used for the fits are shown in figure 4.2 ($\rho_{\Lambda MC} - \rho_\Lambda$ left, $p_{\Lambda MC} - p_\Lambda$ right)

Table 4.1 is to be compared with the corresponding table 5.1 for $\Sigma^0\pi^0$ events, generated by hadronic interactions of K^- in the gas filling the KLOE DC. The long tail for positive values of $p_{\Lambda MC} - p_\Lambda$ in figure 4.2 (right) is due to the charged particles energy loss, mainly in the material of the DC entrance wall, particularly important for protons. This makes the momentum resolution more degraded for events in the wall respect to absorptions in the gas, and causes a systematic shift of the final $m_{\Sigma^0\pi^0}$ and $p_{\Sigma^0\pi^0}$ distributions of few MeV . Nevertheless, such an effect

Table 4.1: Resolutions calculated with MC. Values indicates the sigma of a Gaussian fit on the MC-REC distribution, as explained in the text.

σ_{p_Λ}	$4.49 \pm 0.04 \text{ MeV}/c$
σ_{ρ_Λ}	$0.20 \pm 0.01 \text{ cm}$

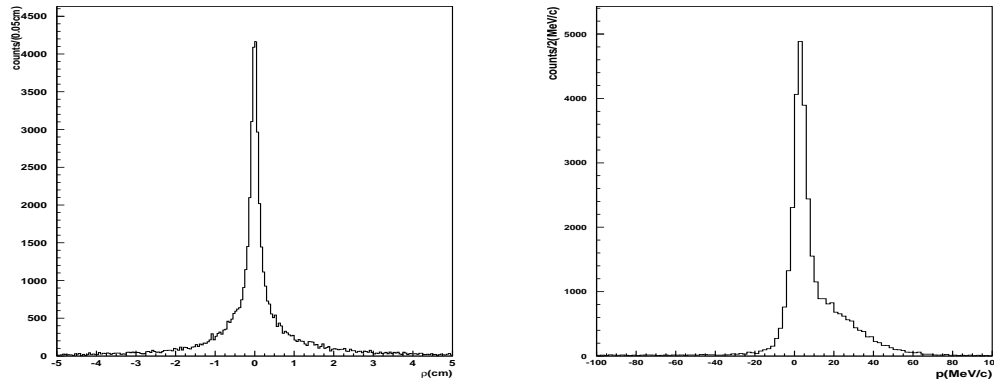


Figure 4.2: Resolutions calculated with MC, $\rho_{\Lambda MC} - \rho_\Lambda$ left, $p_{\Lambda MC} - p_\Lambda$ right.

is completely overwhelmed by the corresponding $m_{\Sigma^0\pi^0}$ and $p_{\Sigma^0\pi^0}$ resolutions (see section 4.7) which are dominated by the calorimeter resolution for neutral clusters.

4.5 Λ decay vertex selection

In figure 4.3 is represented the radial decay vertex position ρ_Λ of the $\Lambda(1116)$, for a subsample of the total events for which no previous cuts were applied on the $\Lambda(1116)$ decay vertex position.

The lower bump (for $\rho_\Lambda \sim 10 \text{ cm}$) corresponds to hadronic interactions of K^- in the beryllium sphere surrounding the interaction point. The second higher peak located at $\rho_\Lambda \sim 25 \text{ cm}$ represents hadronic interactions of K^- inside the DC entrance wall. The two peaks are separated by the tails of the distributions, together with the contribution of K^- absorptions in air. The long tail for higher

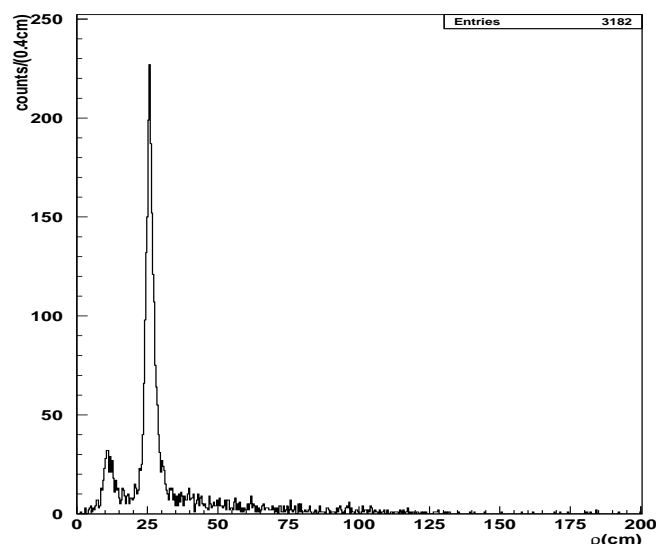


Figure 4.3: Plot representing the ρ_Λ distribution.

ρ_Λ values corresponds to interactions occurring in the gas filling the DC. The asymmetric right tail of the $\rho_\Lambda \sim 25\text{ cm}$ peak is due to the decay path of the $\Lambda(1116)$ (see figure 3.9).

When optimizing the acceptance criterion of ρ_Λ for K^- absorption in the DC entrance wall, we were driven by the necessity to maintain the highest statistics, minimizing the contribution of K^- interactions in the gas. This is motivated by the fact that events in the wall served as a guide to understand the kinematics of the K^- nuclear absorptions, as described in the following.

First a simple Gaussian plus linear background fit was performed to the $\rho_\Lambda \sim 25\text{ cm}$ peak in the interval $16\text{ cm} < \rho_\Lambda < 50\text{ cm}$, the lower limit taking into account for the decay path of the Λ s produced in the beryllium beam sphere. The result of the fit is shown in figure 4.4 left.

In order to better describe the right tail of the distribution we then repeated the fit by using a linear background plus a sum of Gaussians:

$$f(x) = \sum_{i=1}^{30} A_i e^{-\frac{(x-x_{0i})^2}{2p_3^2}} + p_4 + p_5 x, \quad (4.5)$$

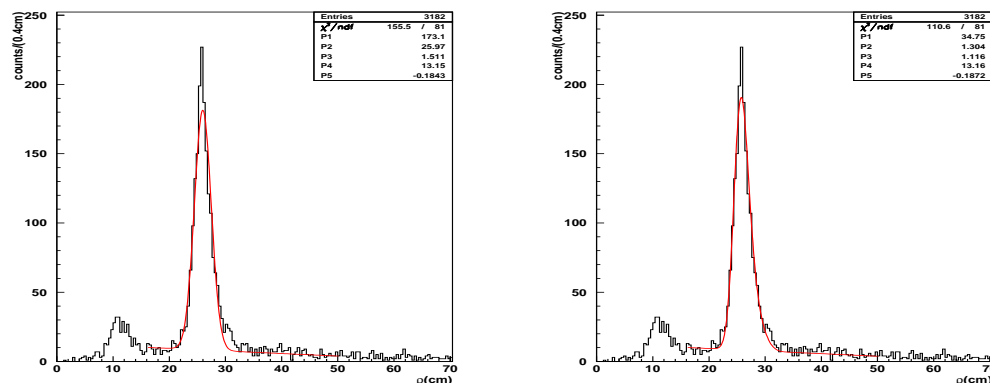


Figure 4.4: Gaussian plus linear background fit to the ρ_Λ distribution (left), multi-Gaussian plus linear background fit to the ρ_Λ distribution (right).

with central values (x_{0i}) ranging from 25 cm to 31 cm (the maximum observed decay path). The step between the centers corresponds to the resolution $\sigma_{\rho_\Lambda} = 0.2$ cm in the vertex position. The amplitudes of the Gaussians follow an exponential law

$$A_i = p_1 e^{-\frac{0.2(i-1)}{p_2}}, \quad (4.6)$$

with p_1 , p_2 , p_3 , p_4 and p_5 free parameters of the fit. The results of the fit are shown in figure 4.4 right. The second fit gives a better χ^2/ndf , nevertheless the parameters p_4 and p_5 , describing the gas absorptions contamination, are not substantially modified. According to MC simulations of K^- absorptions in the wall and to the performed fit, the best compromise between statistics and background rejection is given by the choice

$$\rho_\Lambda = 25 \pm 1.2 \text{ cm} \quad (4.7)$$

corresponding to a contamination of K^- interactions in gas ($5.5^{+1.3}_{-1.8}\%$), the errors given by the uncertainties on p_4 and p_5 .

4.6 Missing mass distribution

As described in section 1.3.1 atomic K^- nuclear captures are expected to occur on a single proton at the surface of the nucleus, leaving the residual boron as a spectator of the quasi-free process. In this section a missing mass study will be described, whose results are in agreement with this picture. Under the assumption that the contamination from absorptions in Aluminium can be neglected and kaons are mainly absorbed in Carbon, the missing mass of the residual nucleus in the reaction

$$K^- C \rightarrow \Sigma^0 \pi^0 R. \quad (4.8)$$

can be calculated (here R represents the residual nucleus). In order to calculate the missing mass we will assume K^- absorptions at rest, so that the missing mass is given by:

$$mm = \sqrt{\left[m_k + m_C - \sqrt{m_{\Sigma^0 \pi^0}^2 + p_{\Sigma^0 \pi^0}^2} \right]^2 - p_{\Sigma^0 \pi^0}^2}. \quad (4.9)$$

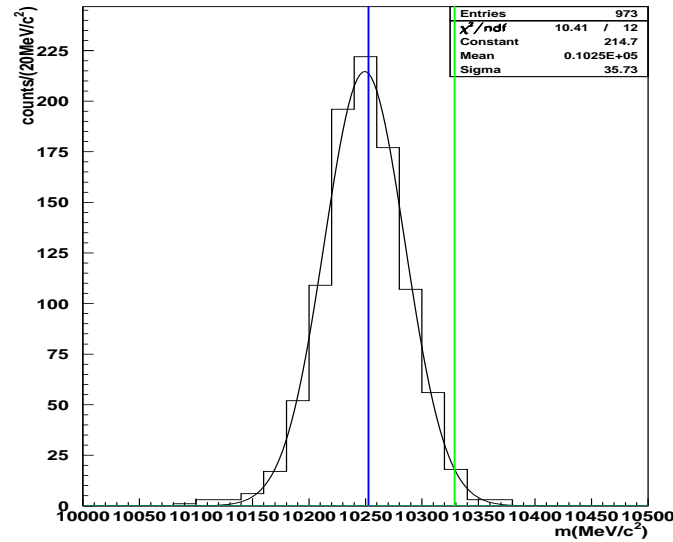


Figure 4.5: Plot representing the mm spectrum.

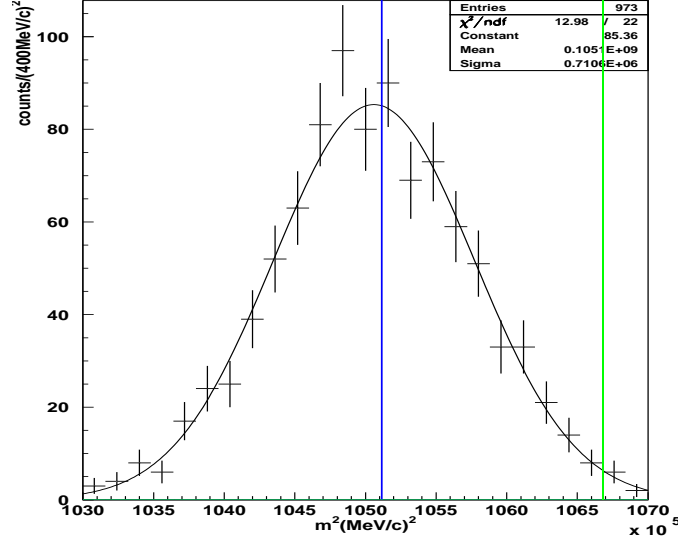


Figure 4.6: Plot representing the mm^2 spectrum.

In figures [4.5, 4.6] the obtained missing mass and missing mass squared (mm^2) are represented. The blue line represents the mass of the ^{11}B , while the green line indicates the sum of the masses of five unbound protons and six unbound neutrons. The mm distribution is peaked around the ^{11}B mass, in agreement with the hypothesis that K^- interacts with a proton at the surface of the nucleus, leaving a boron as spectator. Nevertheless, a small shift to lower missing mass is also evident, especially in the mm^2 distribution. This shift could be explained by considering that part of the absorptions do not occur at-rest, but in-flight, in this case the missing mass turns to be:

$$mm_{if} = \sqrt{\left[\sqrt{m_k^2 + p_k^2} + m_C - \sqrt{m_{\Sigma^0\pi^0}^2 + p_{\Sigma^0\pi^0}^2} \right]^2} - p_R^2, \quad (4.10)$$

p_R representing the momentum of the residual nucleus. In the case of absorptions in-flight our previous estimated mm (formula 4.9) turns to be lower than the actual value mm_{if} , due to the kaon momentum. Negative kaons starting with a momentum of $127\text{MeV}/c$ lose few energy in crossing the DC wall before interacting. According to MC simulations the mean K^- momentum at the interaction

point, for absorptions in flight, is $p_k \sim 120 \text{ MeV}/c$). To test this hypothesis two subsamples of the reconstructed events were chosen, according to a z coordinate of the $\Lambda(1116)$ decay vertex position (z_Λ) less than 10 cm or greater than 20 cm . The distribution of z_Λ for the whole sample is shown in figure [4.7].

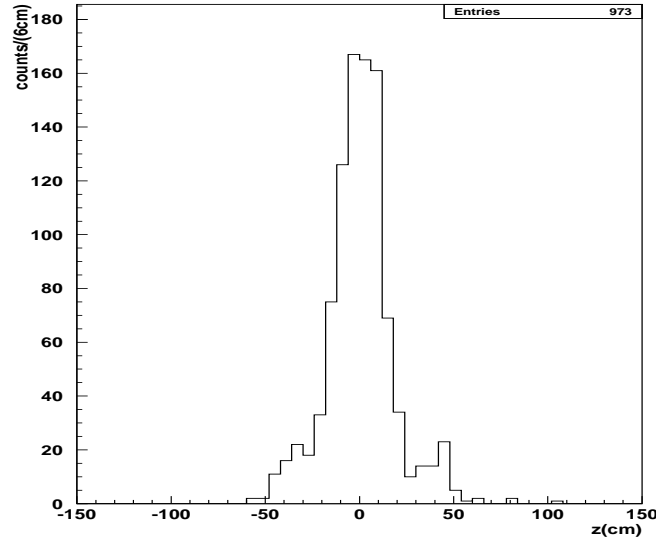
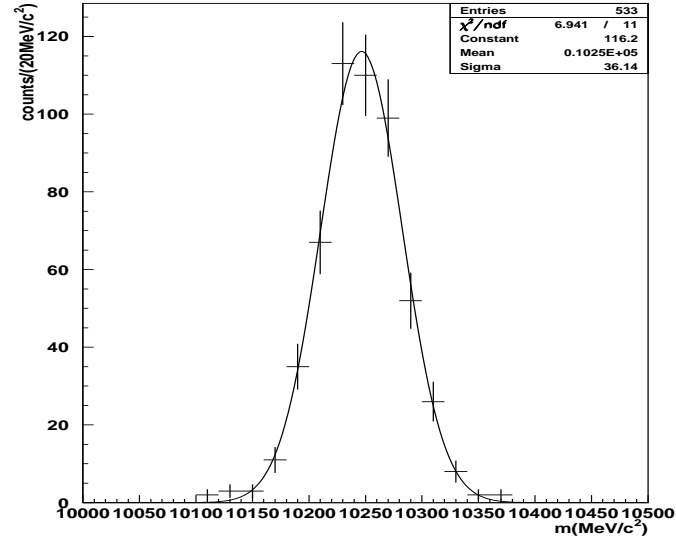
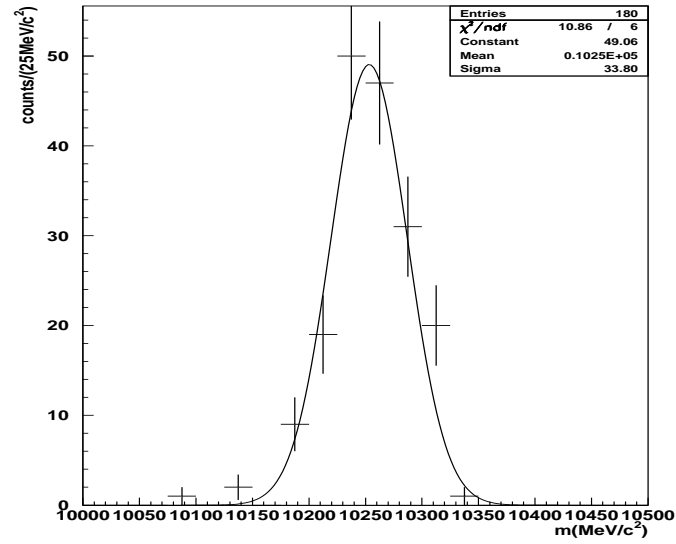


Figure 4.7: Plot representing the z_Λ distribution.

Considering that the thickness crossed by a kaon penetrating the wall at $z_\Lambda = 40 \text{ cm}$ is 1.7 cm (with respect to the 0.9 cm thickness of the wall for $z_\Lambda = 0 \text{ cm}$), we expect that a greater number of stopped kaons should be found at high z_Λ values. Plots [4.8, 4.9] show the mm distribution for the selected subsamples.

A Gaussian fit was performed to both mm distributions and the following mean values were found ($mm_0 = 10253 \pm 2 \text{ MeV}/c^2$) for $z_\Lambda > 20 \text{ cm}$, ($mm_0 = 10246 \pm 1 \text{ MeV}/c^2$) for $z_\Lambda < 10 \text{ cm}$. The fit to the $z_\Lambda > 20 \text{ cm}$ sample gives a mean missing mass value which better agrees with the ^{11}B mass, respect to the fit to the $z_\Lambda < 10 \text{ cm}$ which is shifted to lower masses of about $7 \text{ MeV}/c^2$.

Figure 4.8: mm distribution for $z_\Lambda < 10$ cm.Figure 4.9: mm distribution for $z_\Lambda > 20$ cm.

4.7 $\Sigma^0\pi^0$ invariant mass and momentum distributions

Once the identification of each particle of the event is completed, as described in Chapter 3, the momentum and invariant mass distributions of $\Sigma^0\pi^0$ are obtained, we will use the following notation:

$$m_{\Sigma^0\pi^0} = \sqrt{E_{\Sigma^0\pi^0}^2 + p_{\Sigma^0\pi^0}^2} \quad (4.11)$$

$$E_{\Sigma^0\pi^0} = E_{\Sigma^0} + E_{\pi^0} \quad (4.12)$$

$$\mathbf{p}_{\Sigma^0\pi^0} = \mathbf{p}_{\Sigma^0} + \mathbf{p}_{\pi^0}. \quad (4.13)$$

The $m_{\Sigma^0\pi^0}$ and $p_{\Sigma^0\pi^0}$ distributions are shown in figures [4.10, 4.11] respectively

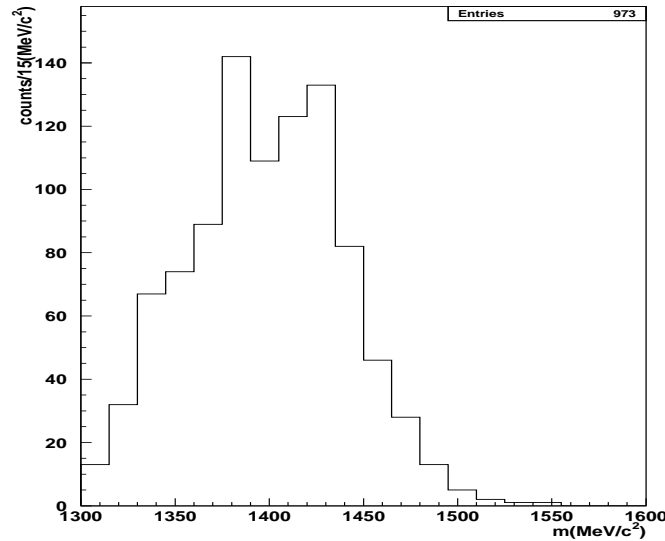
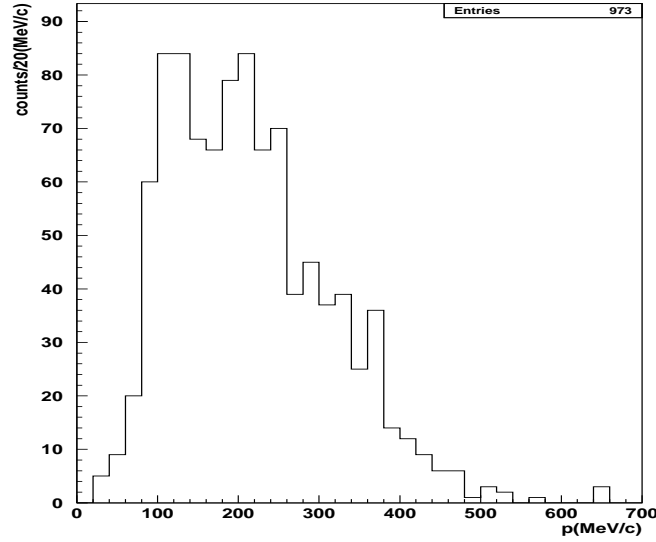


Figure 4.10: $m_{\Sigma^0\pi^0}$ distribution.

The invariant mass and momentum resolutions were studied by means of MC simulations, in which K^- interacts with Carbon nuclei in the DC entrance wall, following the quasi-free reaction

$$K^- C \rightarrow \Sigma^0 \pi^0 {}^{11}B. \quad (4.14)$$

Figure 4.11: $p_{\Sigma^0\pi^0}$ distribution.

K^- interacts with a proton of the Carbon nucleus, while the residual boron behaves as a spectator. The Gaussian fits to the distributions $(m_{\Sigma^0\pi^0 TRU EMC} - m_{\Sigma^0\pi^0})$ and $(p_{\Sigma^0\pi^0 TRU EMC} - p_{\Sigma^0\pi^0})$ return the following standard deviations:

$$\sigma_m \sim 32 MeV/c^2 \quad ; \quad \sigma_p \sim 20 MeV/c^2, \quad (4.15)$$

as expected each photon cluster introduces an enlargement of about $10 MeV/c^2$ in the invariant mass distribution. The $m_{\Sigma^0\pi^0}$ distribution is very broad, and shows an excess of events above the kinematic limit for K^- absorptions on Carbon nuclei at rest ($m_{lim} = 1415.9 MeV/c^2$). The $p_{\Sigma^0\pi^0}$ distribution shows a structure, with a lower momentum component (LM) at around 100 MeV/c and a higher momentum component (HM) around 200 MeV/c (distinguishable within the $p_{\Sigma^0\pi^0}$ resolution) together with a high momentum tail for $p_{\Sigma^0\pi^0} > 250 MeV/c$.

The nature of such structuring in the momentum distribution was explored by investigating the scatterplots of the relevant kinematic variables. In figure 4.12 are shown the correlations of $m_{\Sigma^0\pi^0}$ with $p_{\Sigma^0\pi^0}$ and $\theta_{\Sigma^0\pi^0}$ with $p_{\Sigma^0\pi^0}$; here we mean by $\theta_{\Sigma^0\pi^0}$ the angle between \mathbf{p}_{Σ^0} and \mathbf{p}_{π^0} in the laboratory reference frame.

Both scatterplots in figure 4.12 show two enhancements, the LM component

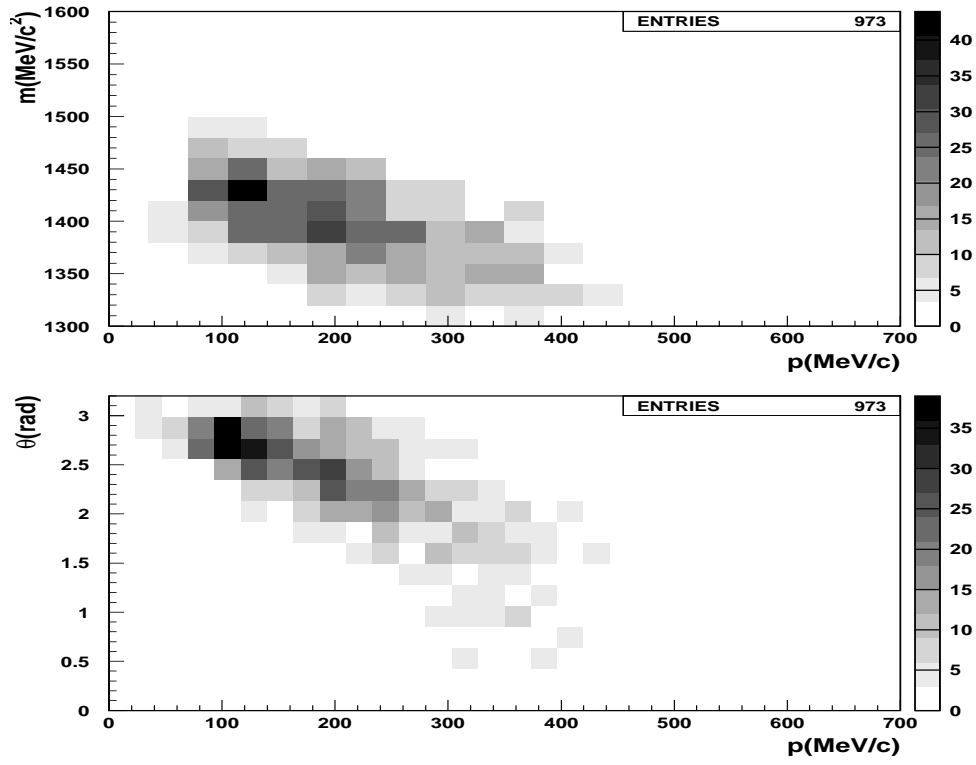


Figure 4.12: Top $m_{\Sigma^0\pi^0}$ vs $p_{\Sigma^0\pi^0}$, bottom $\theta_{\Sigma^0\pi^0}$ vs $p_{\Sigma^0\pi^0}$.

is correlated with masses above the kinematical limit m_{lim} (around $1430 \text{ MeV}/c^2$ i.e. few MeV below the kinematical limit in flight) and greater angles, the HM component is correlated with lower masses and smaller angles. This can be kinematically interpreted as a lower mass object corresponding to the production of higher momentum $\Sigma^0\pi^0$ couples with smaller $\theta_{\Sigma^0\pi^0}$ angles, together with a higher mass low momentum object. Similar correlations appear when representing $p_{\Sigma^0\pi^0}$ and $m_{\Sigma^0\pi^0}$ as a function of the pion kinetic energy T_{π^0} , as shown in figure 4.13.

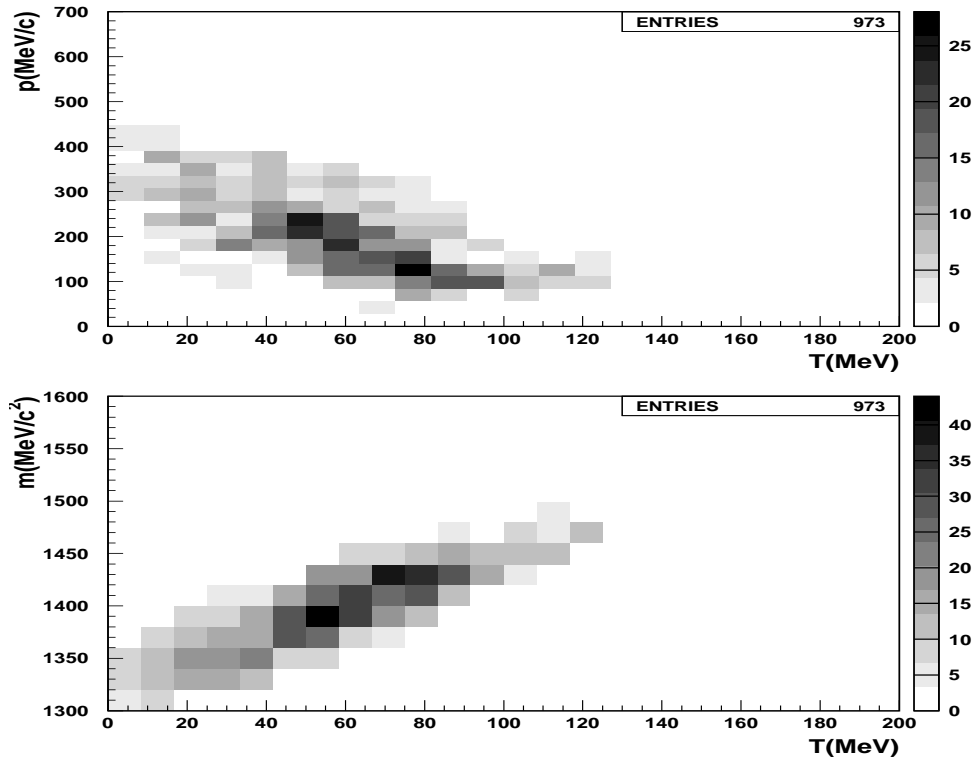


Figure 4.13: Top $p_{\Sigma^0\pi^0}$ vs T_{π^0} , bottom $m_{\Sigma^0\pi^0}$ vs T_{π^0} .

The LM $p_{\Sigma^0\pi^0}$ component is associated with an enhancement at $T_{\pi^0} \sim 70 - 80 \text{ MeV}$, corresponding to higher $m_{\Sigma^0\pi^0}$ values, while the HM $p_{\Sigma^0\pi^0}$ component is associated with $T_{\pi^0} \sim 50 - 60 \text{ MeV}$ and lower $m_{\Sigma^0\pi^0}$ values. The resolution in the kinetic energy of the pion $\sigma_{T_{\pi^0}}$ was checked by means of MC true information, and turns to be about 12 MeV .

4.8 Comparison of the $p_{\Sigma^0\pi^0}$ and T_{π^0} distributions with emulsion experiments

In section 1.3.1 we summarized the results obtained from the analysis of $\Sigma^\pm\pi^\mp$ production for K^- absorption in emulsion. We will compare in this section our observed distributions with the corresponding distributions reported in [30]. In figure 1.4 is represented the $p_{\Sigma^\pm\pi^\mp}$ distribution for a compilation of various experiments studying K^- absorption *at rest* in emulsion, with similar angular cuts for the final selected recoil events. As observed by the authors, $p_{\Sigma^\pm\pi^\mp}$ results clearly peaked around 200 MeV/c , in good agreement with Adair's calculation for the $K^- C \rightarrow \Sigma\pi \text{ } ^{11}\text{B}$ reaction at rest. If we compare this plot with figure 4.11 we could argue that such structure seems to be reproduced by the HM peak located around 200 MeV/c (taking into account for the $p_{\Sigma^0\pi^0}$ distribution greater enlargement).

We then tried to separate in our sample K^- absorptions in flight, by applying a rough cut on $m_{\Sigma^0\pi^0}$, selecting those events in which the measured invariant mass is greater than the kinematical limit for K^- absorption at rest in Carbon ($m_{lim} \sim 1416 \text{ MeV}/c^2$). Figure 4.14 represents $p_{\Sigma^0\pi^0}$ for: the whole sample (black), the events corresponding to $m_{\Sigma^0\pi^0} > m_{lim}$ (in green) and the events for which $m_{\Sigma^0\pi^0} < m_{lim}$ (in red). Of course, our invariant mass resolution prevents us from a definite identification of the events in flight, moreover the $m_{\Sigma^0\pi^0} < m_{lim}$ condition is not sufficient for an event to be at rest. Nevertheless, the LM and HM components result clearly splitted in figure 4.14, so that the higher mass object correlated to the LM component seems to originate from in flight absorptions. Moreover the red $p_{\Sigma^0\pi^0}$ distribution (of events not in flight according to our rough cut) is peaked around 200 MeV/c , similar to figure 1.4 (with a greater full width due to σ_p).

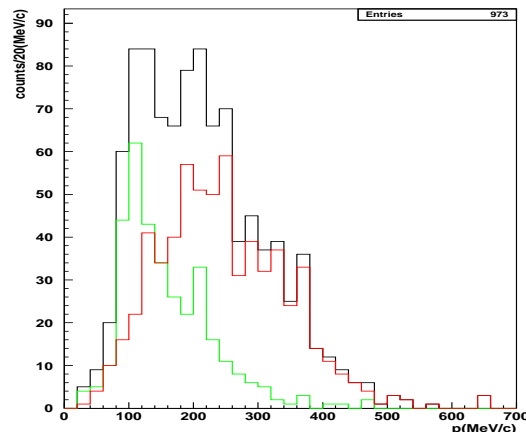


Figure 4.14: $p_{\Sigma^0\pi^0}$ for the whole sample (black), events "in flight" (green) and non "in flight" (red), according to the criterion explained in the text.

When describing figure 4.13 we already stressed that two regions are distinguishable, for π^0 kinetic energies around 50-60 MeV and 80 MeV, which correspond respectively to the HM and LM $p_{\Sigma^0\pi^0}$ momentum components. In figure 4.15 the pion kinetic energy T_{π^0} is plotted for the whole sample (black), for the events fulfilling the $m_{\Sigma^0\pi^0} > m_{lim}$ condition (in green) and the events for which $m_{\Sigma^0\pi^0} < m_{lim}$ (in red), together with the same correlation plot as in figure 4.13.

Again in plot 4.15 the red T_{π^0} component, correlated to the HM $p_{\Sigma^0\pi^0}$ component, is nicely separated from the green one associated to LM. The red distribution is peaked at around 50 MeV according to the results of [30] (1.3) for K^- absorption at rest.

By comparing our observed distributions with the corresponding results in [30] we then arrive to the following conclusion: the HM $p_{\Sigma^0\pi^0}$ component, which is correlated to lower $m_{\Sigma^0\pi^0}$ invariant masses, is consistent with the $p_{\Sigma^\pm\pi^\mp}$ distribution observed in K^- absorption at rest in emulsion, also the corresponding T_{π^0} distribution seems to originate from interactions at rest. The raw cut $m_{\Sigma^0\pi^0} > m_{lim}$, applied to isolate events in flight, clearly selects the LM $p_{\Sigma^0\pi^0}$ sample (which is correlated to $m_{\Sigma^0\pi^0}$ invariant masses predominantly above the kinematic limit for K^- absorption at rest in carbon), also the corresponding enhancement in the $p_{\Sigma^0\pi^0}$ vs

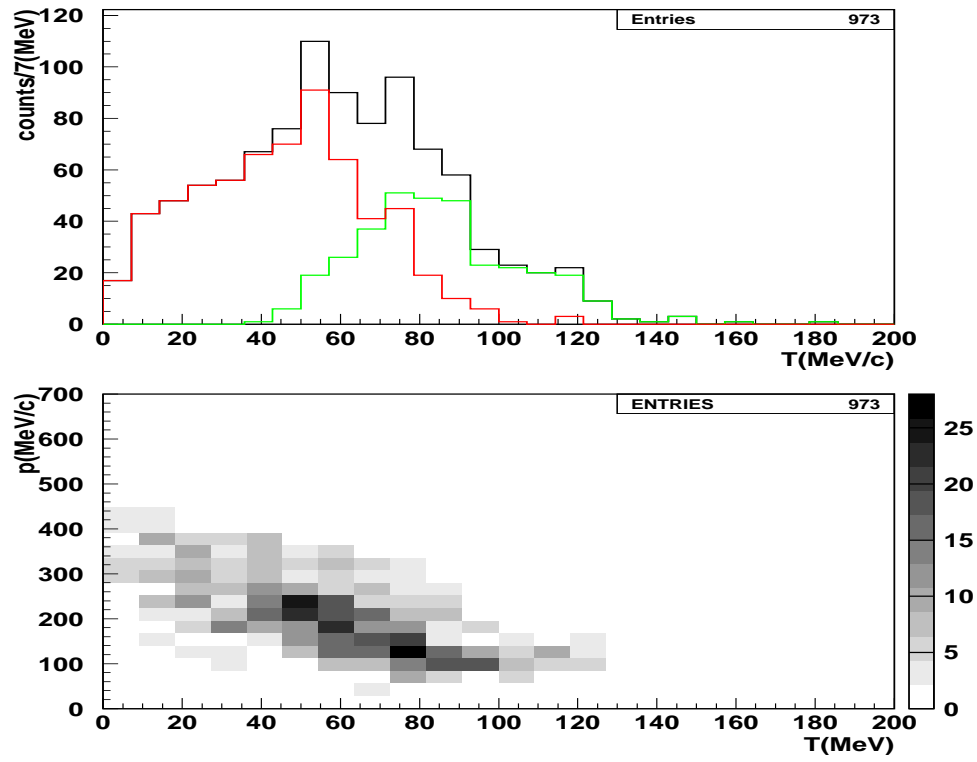


Figure 4.15: Top T_{π^0} for the whole sample (black), events "in flight" (green) and non "in flight" (red), according to the criterion explained in the text, bottom $p_{\Sigma^0\pi^0}$ vs T_{π^0} .

T_{π^0} is separated (green curve in figure 4.13) thanks to the sufficient resolution in π^0 kinetic energy. The LM component turns then naturally interpreted as originating from K^- absorptions in flight.

A further confirmation of this hypothesis comes from MC simulations of K^- absorption in Carbon occurring in the entrance wall of the KLOE DC. The reconstructed π^0 kinetic energy is shown in figure 4.16 for MC events calculated at rest (green) compared with data (black), the cut $m_{\Sigma^0\pi^0} < m_{lim}$ was applied to both samples (the distributions are normalized to one). In figure 4.17 the same T_{π^0} distribution is plotted for MC events calculated in flight (green) compared with data (black) (both normalized to unity), the cut $m_{\Sigma^0\pi^0} > m_{lim}$ was applied to both samples.

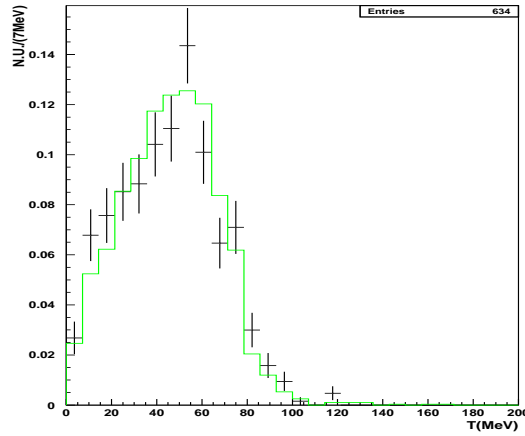


Figure 4.16: T_{π^0} for MC events calculated at rest (green), compared with data (black) the cut $m_{\Sigma^0\pi^0} < m_{lim}$ was applied to both samples.

A reasonable agreement is found between data and MC. As a comparison, in figure 4.18 the T_{π^0} distribution is plotted for MC events calculated in flight (green) compared with data (black), when the $m_{\Sigma^0\pi^0} < m_{lim}$ is applied to both samples, the two distributions are clearly shifted.

A lower limit for the ratio of in flight over at rest events can be evaluated:

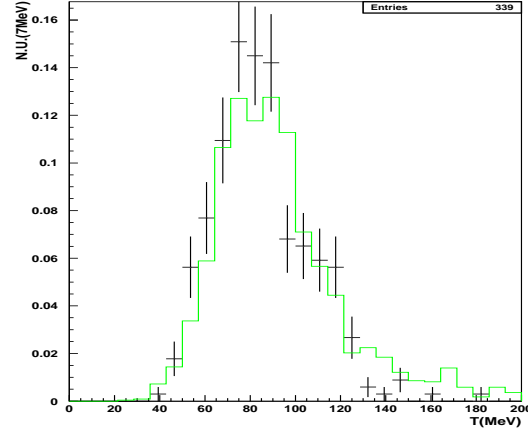


Figure 4.17: T_{π^0} for MC events calculated in flight (green), compared with data (black) the cut $m_{\Sigma^0\pi^0} > m_{lim}$ was applied to both samples.

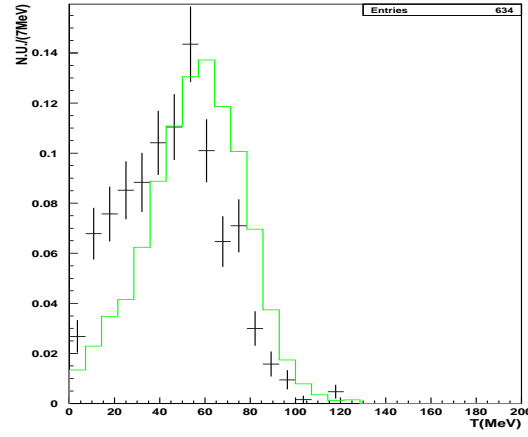


Figure 4.18: T_{π^0} for MC events calculated in flight (green), compared with data (black) the cut $m_{\Sigma^0\pi^0} < m_{lim}$ was applied to both samples.

$$\frac{n_{>m_{lim}}}{n_{<m_{lim}}} \sim 0.53 \pm 0.04. \quad (4.16)$$

4.9 Analysis of K^- absorptions in pure Carbon target

As mentioned in section 4.2, pushed by the obtained results, outlined in this Chapter, a high purity Carbon target (graphite) was realized in summer 2012 and installed inside the KLOE DC, between the beam pipe and the DC entrance wall.

The target was realized with the main aim to test the hypothesis that we put forward in the present analysis, and to collect a higher statistics for the study of the low energy K^-C hadronic interaction in different channels. To this and the target must satisfy two main requests, first a pure composition is mandatory to eliminate the influence of the presently unavoidable aluminium contamination, accounting for 19% of the total absorptions. Second we should select a clean sample of absorptions at rest, this is simple and relatively cheap to be realized by stopping K^- in a thick solid target.

The geometry of the target was optimized by means of GEANT3 MC simulations. The final configuration consists of three half-cylindrical graphite segments ($\rho = 0.95g/cm^3$) supported by an aluminium frame, for a total length of 600mm and a radius of 24,7mm. The half-cylindrical configuration was chosen in order to take advantage of the K^+ tagging. The segmentation of the target is required by the fragility of the chosen material, while the angular opening was set by testing the target insertion procedure inside the KLOE DC with aluminium prototypes. The thickness of the target, 6mm in the boost direction and 4mm in the anti-boost direction, was chosen to balance a high K^- stopping probability with the lowest possible energy loss, suffered by the charged decay products, inside the target material itself and the DC entrance wall. The final project of the realized target is shown in figure 4.19

According to MC simulations an integrated luminosity of $100pb^{-1}$ will translate in a gain factor ~ 3 , with respect to the already analysed statistics in the DC wall. Moreover, the contamination from absorptions in aluminium will be reduced from 19% to 7%.

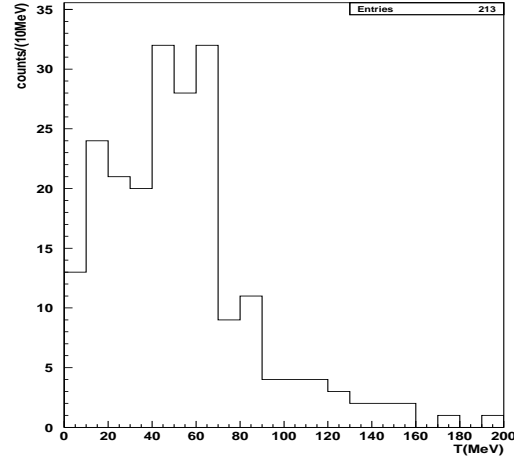


Figure 4.20: T_{π^0} for K^- absorptions in Carbon target.

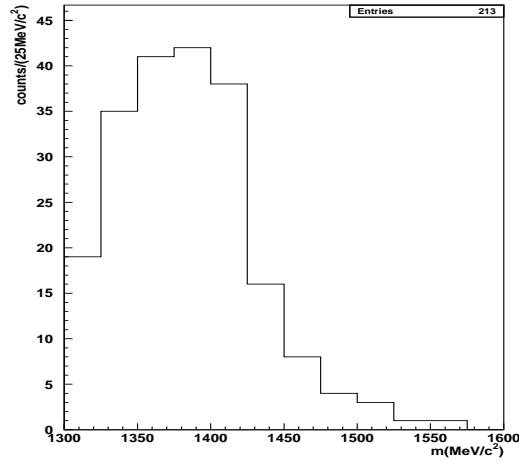


Figure 4.21: $m_{\Sigma^0\pi^0}$ spectrum for K^- absorptions in Carbon target.

the $m < m_{lim}$ events were selected. The HM $p_{\Sigma^0\pi^0}$ component, around $200 \text{ MeV}/c$, then confirms to be originated in at rest absorptions.

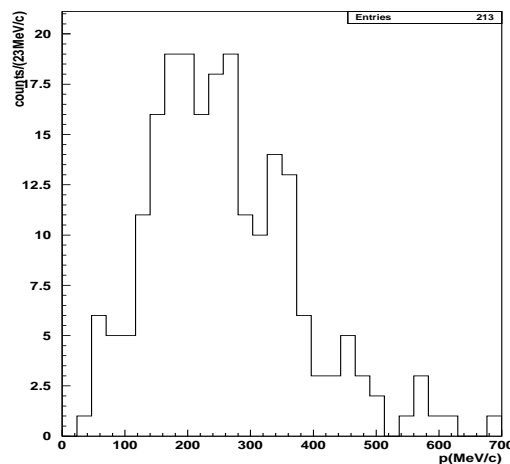


Figure 4.22: $p_{\Sigma^0\pi^0}$ spectrum for K^- absorptions in carbon target.

The preliminary analysis performed on the presently available small sample of K^- absorptions in Carbon target data, thus agrees with the interpretations outlined in the course of this Chapter concerning the kinematics of $K^- C$ interactions in the KLOE DC entrance wall.

4.10 Analysis of the background: $\Sigma(1385)$ and internal conversion events

Two main background sources can affect the final reconstructed events, namely $\Sigma(1385)$ events and internal conversion.

The $\Sigma(1385)$ can not decay into $\Sigma^0\pi^0$ for isospin conservation, but its main decay mode ($\Lambda\pi^0$, $BR = 87.0 \pm 1.5$) could constitute a source of background if the photon associated with the Σ^0 decay by the reconstruction algorithm (which was named γ_3 in 3.6) was not "genuine". The main cause for neutral cluster misidentification as a photon cluster could be a wrong track to cluster association by the standard KLOE reconstruction, even if the first χ_t^2 minimisation is expected

to drastically reduce such occurrence, selecting clusters by time of flight (in the hypothesis of light speed) as the following analysis will confirm.

Internal conversion occurs as a consequence of secondary interaction of the Σ^0 with nucleons following the reaction:

$$\Sigma^0 N \rightarrow \Lambda N' \quad (4.17)$$

which competes with the Σ^0 decay process in $\Lambda \gamma_3$.

Both processes produce the same final state particles $\Lambda \pi^0$ with a possible observable difference in the π^0 momentum, which is expected to be higher for direct $\Lambda \pi^0$ production (see for example [33] and section 1.3.2 for a detailed discussion). Background contamination was first tested by a characterization of the neutral clusters associated by the reconstruction procedure to γ_3 , and a study of the Λ momentum distribution. Then a quantitative estimate of the background contribution was obtained by using dedicated MC simulations.

4.10.1 γ_3 clusters characterisation

As described in 4.10 both $\Sigma(1385) \rightarrow \Lambda \pi^0$ and internal conversion events are characterized by the same final state topology. Consequently, a first immediate check to be performed regards the properties of the γ_3 neutral cluster. If an important background contribution would be present in the selected events, then the cluster which the reconstruction associates to γ_3 should exhibit some difference.

The available information about calorimeter clusters is the time and the energy released. First we tested the time distribution, comparing the time for prompt photons which are associated to γ_1 and γ_2 by χ_t^2 and $\chi_{\Sigma\pi}^2$ minimisations (black distribution in figure 4.23) with the time of the clusters selected as γ_3 (green curve in figure 4.23). No difference arises between photons associated to π^0 decay and γ_3 .

In figure 4.24 the energy distribution of the couples γ_1 and γ_2 is plotted in black, together with the energy spectrum of γ_3 in green. The blue curve represents the E_{γ_3} spectrum of reconstructed γ_3 s, in pure signal simulated events. K^- nuclear interactions were generated with protons in Carbon nuclei according to the following reaction:

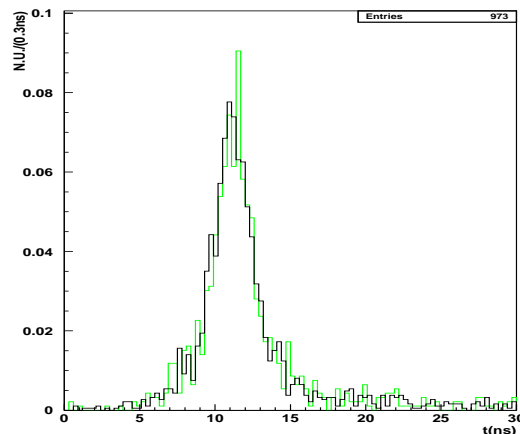


Figure 4.23: Time distribution of γ_3 (green curve), together with the same distribution for γ_1 and γ_2 (black curve).

$$K^- C \rightarrow \Lambda(1405) {}^{11}B \rightarrow \Sigma^0 \pi^0 {}^{11}B, \quad (4.18)$$

in a quasi-free fashion with the boron behaving like a spectator (secondary interactions of the produced Σ^0 and π^0 with the residual nucleus were neglected). The K^- absorptions are generated in the entrance wall of the KLOE DC and energy loss effects for charged particles, in crossing the KLOE materials, are taken into account. Both K^- interactions at rest and in flight are considered, in equal number. The agreement of MC with data is straightforward, the clusters associated to γ_3 do not show any unexpected behaviour.

In order to check possible differences arising between the LM and HM components in the observed $p_{\Sigma^0 \pi^0}$ spectrum, the whole sample of data was roughly divided into two subsamples according to $p_{\Sigma^0 \pi^0}$ greater or less than $160 \text{ MeV}/c$. No difference was found in the t_{γ_3} and E_{γ_3} distributions for the two samples.

4.10.2 Study of the Λ momentum distribution

A clear evidence for the presence of $\Sigma(1385)$ events passing the analysis cuts should be given by the study of the Λ momentum. The idea is to employ the great mass

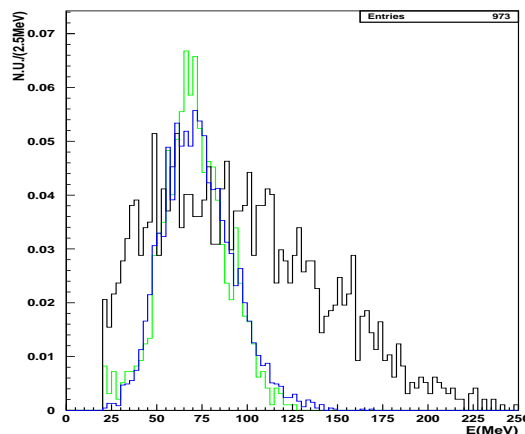


Figure 4.24: Energy distribution of the couples γ_1 and γ_2 (black) together with the energy spectrum of γ_3 (green). The blue curve represents the reconstructed E_{γ_3} distribution for pure signal MC events as described in the text.

difference between the Σ^0 ($1192.642 \pm 0.024 \text{ MeV}/c^2$) and the $\Sigma(1385)$ ($1383.7 \pm 1.0 \text{ MeV}/c^2$). The Σ^0 decays, in its rest frame, in $\Lambda \gamma_3$ couples with a momentum of $74 \text{ MeV}/c$, while the $\Sigma(1385)$ would decay into $\Lambda \pi^0$ couples characterized by a momentum of $208 \text{ MeV}/c$. As a first test we transformed the measured momentum of the Λ (p_Λ) in the Center of Mass (CM) frame of $\Lambda \gamma_3$, so assuming a correct identification of γ_3 , the obtained distribution for $p_{\Lambda \gamma_3 \text{ CM}}$ is shown in figure (4.25) in black, together with the same distribution for pure signal MC events (we refer to $K^- C \rightarrow \Lambda(1405) {}^{11}\text{B} \rightarrow \Sigma^0 \pi^0 {}^{11}\text{B}$ simulated interactions as described in section 4.10.1). A good agreement between data and simulation (background free) is evident. A Gaussian fit to the black distribution gives the mean value $p_{\Lambda \gamma_3 \text{ CM}} = (74.5 \pm 0.5) \text{ MeV}/c$.

As a cross check, the measured Λ momentum was transformed in the CM frame of $\Lambda \pi^0$, so assuming a misidentification of γ_3 . The obtained $p_{\Lambda \pi^0 \text{ CM}}$ distribution (black) is compared in figure 4.26 with the same distribution for pure $\Sigma(1385)$ background MC events (green). This time the following reaction was taken into account:

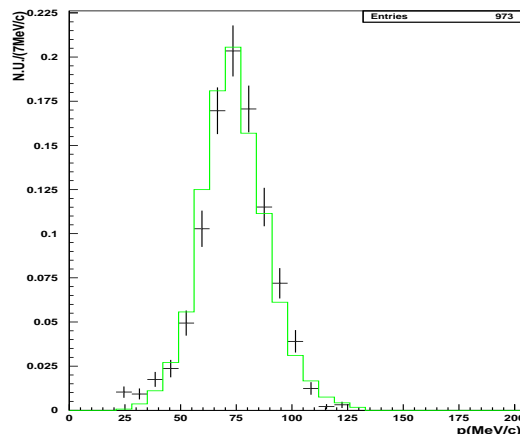


Figure 4.25: The $p_{\Lambda\gamma_3 CM}$ distribution is represented in black together with the same distribution for pure signal MC events (green) as described in the text.

$$K^- C \rightarrow \Sigma(1385) {}^{11}B \rightarrow \Lambda\pi^0 {}^{11}B, \quad (4.19)$$

in a quasi-free fashion with the boron behaving like a spectator (secondary interactions of the produced Λ and π^0 with the residual nucleus were neglected). The K^- absorptions are generated in the entrance wall of the KLOE DC and energy loss effects for charged particles, in crossing the KLOE materials, are taken into account. Both K^- interactions at rest and in flight are considered, in equal number.

In order to obtain the $p_{\Lambda\pi^0 CM}$ value for a simulated event, an algorithm was developed for the reconstruction of $\Lambda\pi^0$ events. Similar to the minimization procedure described in 3.6 a first χ_t^2 searches for two photons in time from the Λ decay vertex position. A second minimization is then based on the π^0 mass, and the event is retained if:

$$\chi_{\pi^0}^2 < 5 \quad \text{where} \quad \chi_{\pi^0}^2 = \frac{(m_{\pi^0} - m_{\gamma\gamma})^2}{\sigma_{m_{\gamma\gamma}}}. \quad (4.20)$$

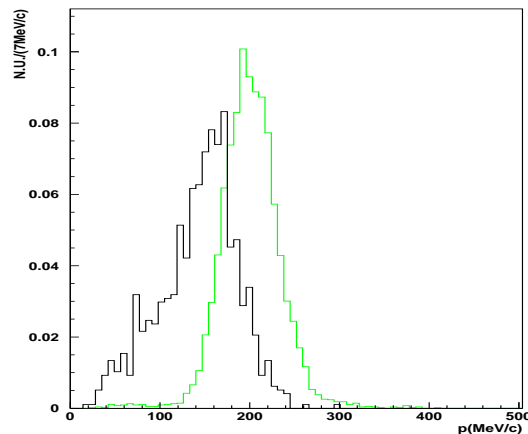


Figure 4.26: The $p_{\Lambda\pi^0 CM}$ distribution is represented in black together with the same distribution for pure $\Sigma(1385)$ background MC events (green) as described in the text.

As expected, the green curve in 4.26 is distributed around $208 MeV/c$, at higher values respect to the black distribution for data.

To conclude this set of tests, also the measured momentum of the Σ^0 was transformed in the rest frame of $\Sigma^0 - \pi^0$. According to PDG the $\Lambda(1405)$ is expected to decay in its rest frame in $\Sigma^0 - \pi^0$ pairs characterized by a momentum of $155 MeV/c$. A Gaussian fit to the obtained $p_{\Sigma^0\pi^0 CM}$ spectrum (performed neglecting the energy loss tail, entering the calculation of $p_{\Sigma^0\pi^0 CM}$ through the momenta of all the reconstructed particles) yields a mean value ($p_{\Sigma^0\pi^0 CM} = 155.6 \pm 1.6 MeV/c$, $(\sigma_{p_{\Sigma^0\pi^0 CM}} = 31.4 \pm 1.5) MeV/c$.

4.10.3 Estimate of the $\Sigma(1385)$ and internal conversion contribution to the final selected sample

In order to give a quantitative estimate of the $\Sigma(1385)$ and internal conversion contamination in the finally selected sample of events, MC simulations of pure signal and pure background (of both types) were performed. $\Lambda(1405)$ and $\Sigma(1385)$ events

were generated as described in 4.10.1 and 4.10.2 respectively. For what concerns internal conversion, $\Sigma^0\pi^0$ pairs were first produced in quasi free interactions of K^- in carbon, according to the reaction:

$$K^- C \rightarrow \Sigma^0\pi^0 {}^{11}\text{B}. \quad (4.21)$$

The K^- absorptions are always considered to occur in the DC entrance wall, with the boron behaving like a spectator. The Σ^0 is never let to decay but forced to interact with a nucleon (N) producing a ΛN phase space. Both K^- interactions at rest and in flight were generated in equal number. A total statistics of 1.5 times 10^5 events was generated for this purpose.

The following approach was then followed:

- the three samples of events were processed with the same reconstruction algorithm, according to the events selection prescription described in Chapter 3. The number of events passing the analysis cuts for the $\Sigma(1385)$ and internal conversion samples will be indicated as $n_{\Lambda\pi^0 D}$ and $n_{\Lambda\pi^0 IC}$, where D and IC stands for direct production and internal conversion respectively.
- Both $n_{\Lambda\pi^0 D}$ and $n_{\Lambda\pi^0 IC}$ were normalized to the number of generated signal events.
- $n_{\Lambda\pi^0 D}$, $n_{\Lambda\pi^0 IC}$ and the number of signal events passing the analysis cuts ($n_{\Sigma^0\pi^0}$) are also weighted with the corresponding branching ratios for $\Lambda\pi^0$ and $\Sigma^0\pi^0$ productions, following K^- absorption in Carbon. An internal conversion probability of 0.5 was assumed, and the branching fractions listened in table 4.2 according to [42] were used.

Table 4.2: Branching fraction for $\Lambda\pi^0$ and $\Sigma^0\pi^0$ production following K^- absorption in Carbon.

	$\Lambda\pi^0$	$\Sigma^0\pi^0$
<i>B.R.</i>	0.034 ± 0.010	0.100 ± 0.030

The percentage of background events entering the final selected sample can then be estimated as:

$$\frac{n_{\Lambda\pi^0 D \text{ norm}} + n_{\Lambda\pi^0 IC \text{ norm}}}{n_{\Sigma^0\pi^0} + n_{\Lambda\pi^0 D \text{ norm}} + n_{\Lambda\pi^0 IC \text{ norm}}} = 0.03 \pm 0.01 \quad (4.22)$$

As expected from the analysis described in previous sections the $\Lambda\pi^0$ contamination is small. This demonstrates that the $\Sigma^0\pi^0$ lineshape is almost free from the $I = 1$ $\Sigma(1385)$ contribution, which is one of the main strengths of this study.

Chapter 5

Study of K^- absorption in the gas filling the KLOE drift chamber

5.1 Introduction

In this section we will describe the results of the analysis of K^- nuclear interactions in the gas filling the KLOE DC, giving rise to a $\Sigma^0\pi^0$ pair in the final state. The following sections are structured to be as much as possible symmetric to Chapter 4, with the aim to put in evidence the similarities arising in the obtained results.

5.2 Composition of the gas filling the KLOE DC

The KLOE DC is filled with a mixture of Helium and Isobutane (90% in volume ^4He and 10% in volume C_4H_{10}). We then see that, besides the Helium main component, the fraction of K^- absorptions in Carbon and Hydrogen must be evaluated in order to understand their contribution to the observed spectra.

Let us first try to estimate the ratio of K^- interactions in Helium (n_{KHe}) and K^- interactions in Carbon (n_{KC}), giving rise to a $\Sigma^0\pi^0$ in the final state. Such ratio will be given by:

$$\frac{N_{KHe}}{N_{KC}} = \frac{n_{He} \sigma_{KHe} BR_{KHe}(\Sigma^0\pi^0)}{n_C \sigma_{KC} BR_{KC}(\Sigma^0\pi^0)} \quad (5.1)$$

where in formula 5.1 we mean by $\frac{n_{He}}{n_C}$ the ratio between Helium and Carbon atoms

contained in the DC volume, σ_{KHe} and σ_{KC} are the total inelastic cross sections for K^- scattering on the two different nuclei, $BR_{KHe}(\Sigma^0\pi^0)$ and $BR_{KC}(\Sigma^0\pi^0)$ are the branching ratios for $\Sigma^0\pi^0$ production, following K^- absorption in Helium and Carbon, respectively.

The ratio $\frac{n_{He}}{n_{C_4H_{10}}}$ between Helium atoms and Isobutane molecules is obtained by multiplying the volume percentages by the densities and then dividing the total masses by the single particle masses. This number is then to be divided by the number of Carbon atoms contained in each isobutane molecule to obtain:

$$\frac{n_{He}}{n_C} = 2.263. \quad (5.2)$$

The ratio between the branching fractions $BR_{KHe}(\Sigma^0\pi^0)$ and $BR_{KC}(\Sigma^0\pi^0)$ was taken according to the values reported in [42] to be

$$\frac{BR_{KHe}(\Sigma^0\pi^0)}{BR_{KC}(\Sigma^0\pi^0)} = 0.8 \pm 0.1. \quad (5.3)$$

In [42] the sum of the seven mononucleonic channels was normalized to unity, thus eliminating the influence of multinucleonic captures (similar non-pionic, i.e. multinucleonic, ratios are expected for K^- absorptions in Carbon and Helium, of the order of 0.2 as reported in [42] and [33]). The adopted branching fractions are corrected for secondary interaction probabilities.

For what concerns σ_{KHe} and σ_{KC} , experimental low energy cross section on Helium and Carbon (for K^- momentum $\sim 100 MeV/c$) are not available. We then decided to employ the theoretical values calculated for low energy K^- -nucleus scattering in the references [43; 44]. The final value obtained is:

$$\frac{N_{KHe}}{N_{KC}} = 1.6 \pm 0.2. \quad (5.4)$$

To conclude this section we will estimate the contribution of K^- -nuclear absorptions on Hydrogen from isobutane molecules. In [45] the probability of K^- absorptions on Hydrogen in a mixture of hydrocarbons was measured and found to be as low as (0.040 ± 0.004) . The mixture composition was:

$$24.7\% C_2H_6, \quad 73.9\% C_3H_8 \text{ and } 1.3\% C_4H_{10}. \quad (5.5)$$

We weighted the measured probability taking into account for the Hydrogen content of the mixture adopted in [45] with respect to the pure isobutane case, and for the volume ratio of isobutane in the KLOE DC. The probability of K^- capture on Hydrogen in the drift chamber results to be 0.0028 ± 0.0003 . The contribution of absorptions on Hydrogen is then found to be extremely small and will be neglected in the following analysis.

5.3 MC simulation of $\Sigma^0\pi^0$ production in the DC gas

In the following sections we will refer to the estimated resolutions on geometrical and kinematical variables of interest for the analysis. The resolution studies were performed, as already mentioned, employing the true MC block from the standard KLOE reconstruction software. In order to obtain model independent estimates, quasi-free (non-resonant) $\Sigma^0\pi^0$ production, following K^- absorptions in Helium and Carbon, were simulated. The interaction vertex position is generated inside the KLOE DC volume.

We will not repeat here the whole procedure (already described in section 4.3) for the KLOE MC generation, the only difference being the input file for the non-resonant absorption on Helium. The calculation of the $\Sigma^0\pi^0$ momenta is performed considering a non-resonant quasi-free K^- interaction, with a single bound proton of the ${}^4\text{He}$ nucleus, in which the residual ${}^3\text{H}$ is left in its ground state and behaves like a spectator. Final state interactions were neglected:

$$K^- He \rightarrow \Sigma^0\pi^0 {}^3H. \quad (5.6)$$

The momentum and invariant mass of the generated $\Sigma^0\pi^0$ couples were obtained by imposing momentum and energy conservation, as an example for reactions at rest

$$\mathbf{p}_{\Sigma^0\pi^0} = \mathbf{p}_{\Sigma^0} + \mathbf{p}_{\pi^0} = -\mathbf{p}_{{}^3H} = \mathbf{p}_F \quad (5.7)$$

and

$$m_{\Sigma^0\pi^0} = \sqrt{(m_k + m_{He})^2 + m_{3H}^2 - 2(m_k + m_{He})\sqrt{m_{3H}^2 + p_{3H}^2}} \quad (5.8)$$

where \mathbf{p}_F represents the Fermi momentum of the bound proton in the nucleus.

When interactions in flight are considered, the kaon momentum distribution is generated in accordance with the observed distribution. A search is made in the data events for K^- tracks tagged by dE/dx (a negative kaon is identified in about 20% of the final selected events) and the kaon momentum distribution at the last point of the track is used. The adopted distribution is shown in figure 5.1.

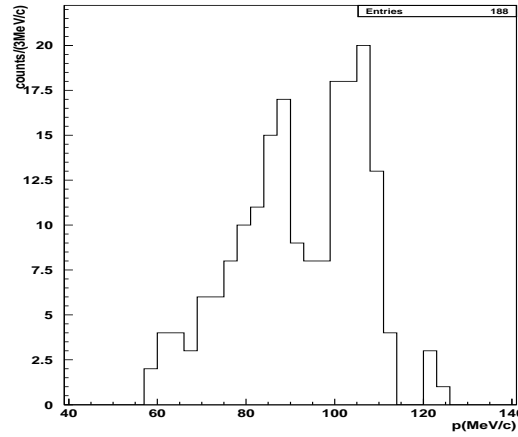


Figure 5.1: Plot representing the \mathbf{p}_k distribution at the last point of the kaon track.

The cosine directors of \mathbf{p}_F and \mathbf{p}_k are then generated randomly, and previous formulas generalise to

$$\mathbf{p}_{\Sigma^0\pi^0} = \mathbf{p}_F + \mathbf{p}_k \quad (5.9)$$

and

$$m_{\Sigma^0\pi^0} = \sqrt{(E_k + m_{He})^2 + m_{3H}^2 - 2(E_k + m_{He})\sqrt{m_{3H}^2 + p_{3H}^2}} \quad (5.10)$$

The adopted Fermi momentum distribution of protons in ^4He nuclei p_F is parametrized according to the AV18 potential model.

5.4 Resolution in ρ_Λ and p_Λ determination

The event selection described in Chapter 3 for data is applied to the non-resonant quasi-free MC generated events, to estimate the resolution in the momentum and radial decay vertex position of the reconstructed Λ s. According to the results obtained in 5.2, the adopted ratio between simulated absorptions in Helium and Carbon is $\frac{n_{KHe}}{n_{KC}} = 1.6$. An equal number of interactions at rest and in flight was considered.

The results are summarised in table 5.1, where the numbers correspond to simple Gaussian fits to the distributions of the originally generated true-MC quantities subtracted by the reconstructed ones, event by event, leaving the tails due to energy loss out of the fit. The corresponding distributions used for the fits are shown in figure 5.2 ($\rho_{\Lambda MC} - \rho_\Lambda$ left $p_{\Lambda MC} - p_\Lambda$ right).

Table 5.1: Resolutions calculated with MC. Values indicates the sigma of a Gaussian fit on the MC-REC distribution, as explained in the text.

σ_{p_Λ}	$1.9 \pm 0.2 \text{ MeV}/c$
σ_{ρ_Λ}	$0.13 \pm 0.01 \text{ cm}$

Comparing table 4.1 with table 5.1 we see the improvement in spatial and momentum resolution. The long energy loss tail (mainly due to the interaction with the material of the DC wall) in the $p_{\Lambda MC} - p_\Lambda$ distribution almost disappears for absorptions in the gas filling the chamber, this also reflects in a better ρ_Λ resolution.

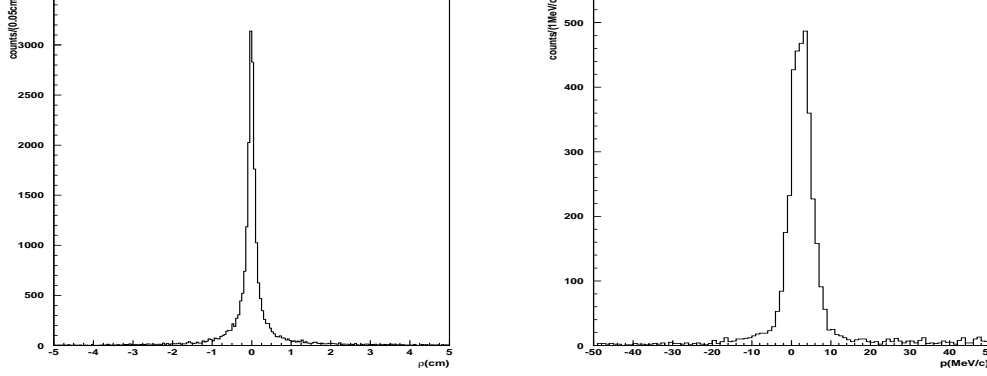


Figure 5.2: Resolution calculated for p_{Λ} (right) and ρ_{Λ} (left) with true MC information.

5.5 $\Sigma^0\pi^0$ invariant mass and momentum distributions

Energy and momentum conservation in each particle identification step is used to obtain the final invariant mass and momentum spectra for the selected $\Sigma^0\pi^0$. The same notation already introduced in the previous Chapter will be used for such variables:

$$m_{\Sigma^0\pi^0} = \sqrt{E_{\Sigma^0\pi^0}^2 + p_{\Sigma^0\pi^0}^2} \quad (5.11)$$

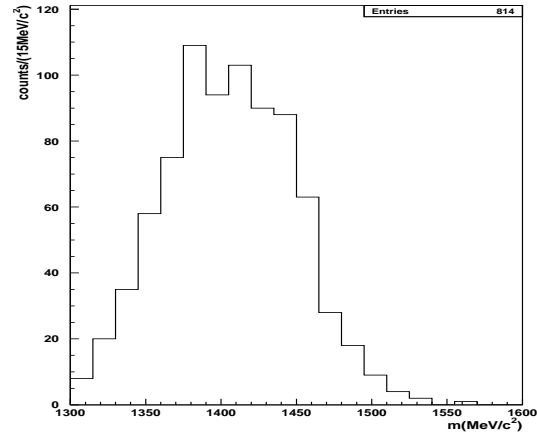
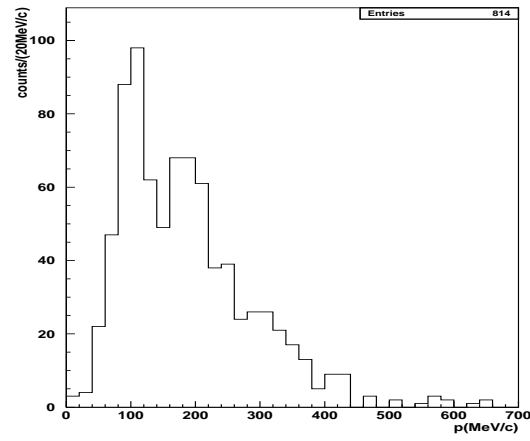
$$E_{\Sigma^0\pi^0} = E_{\Sigma^0} + E_{\pi^0} \quad (5.12)$$

$$\mathbf{p}_{\Sigma^0\pi^0} = \mathbf{p}_{\Sigma^0} + \mathbf{p}_{\pi^0}. \quad (5.13)$$

The $m_{\Sigma^0\pi^0}$ and $p_{\Sigma^0\pi^0}$ distributions are shown in figures 5.3 and 5.4 respectively.

MC simulations of quasi-free non resonant $\Sigma^0\pi^0$ production as described in 5.3 were used to check the invariant mass and momentum resolutions. The ratio between simulated absorptions in Helium and Carbon is 1.6 and an equal number of interactions at rest and in flight were considered. The results of Gaussian fits to the distributions $m_{\Sigma^0\pi^0}^{TRUEMC} - m_{\Sigma^0\pi^0}$ and $p_{\Sigma^0\pi^0}^{TRUEMC} - p_{\Sigma^0\pi^0}$ return the following standard deviations:

$$\sigma_m = 30.6 \pm 0.8 \text{ MeV}/c^2 \quad ; \quad \sigma_p = 15.1 \pm 0.5 \text{ MeV}/c, \quad (5.14)$$

Figure 5.3: $m_{\Sigma^0\pi^0}$ distribution.Figure 5.4: $p_{\Sigma^0\pi^0}$ distribution.

again each photon cluster introduces an enlargement of about $10 \text{ MeV}/c^2$ in the invariant mass distribution. The $p_{\Sigma^0\pi^0}$ resolution is improved with respect to events in the DC wall. The $m_{\Sigma^0\pi^0}$ distribution is very broad, and shows an excess of events above the kinematic limit for K^- absorptions at rest. The kinematical limit is almost the same for absorptions at rest in Carbon and Helium nuclei ($1415.9 \text{ MeV}/c^2$ in Carbon, $1412 \text{ MeV}/c^2$ in Helium) as it depends on the last nucleon binding energy which differs only of 4 MeV . The $p_{\Sigma^0\pi^0}$ distribution shows a double structure, with a lower momentum component (LM) at around $100 \text{ MeV}/c$ and a higher momentum component (HM) around $200 \text{ MeV}/c$. The structure of the $p_{\Sigma^0\pi^0}$ spectrum shows a clear analogy with the corresponding distribution for K^- absorptions in the DC entrance wall. For the events in the gas under consideration $p_{\Sigma^0\pi^0}$ is narrower. A possible reason for this evidence can be the narrower protons Fermi distribution p_F in ^4He (which accounts for most of the absorptions) respect to Carbon, which is reflected in $p_{\Sigma^0\pi^0}$.

The anticorrelation of the kinematical variables observed in section 4.7 can as well be seen in the scatterplots 5.5, $m_{\Sigma^0\pi^0}$ vs $p_{\Sigma^0\pi^0}$ top and $\theta_{\Sigma^0\pi^0}$ vs $p_{\Sigma^0\pi^0}$ bottom ($\theta_{\Sigma^0\pi^0}$ is the angle between \mathbf{p}_{Σ^0} and \mathbf{p}_{π^0} in the laboratory reference frame)

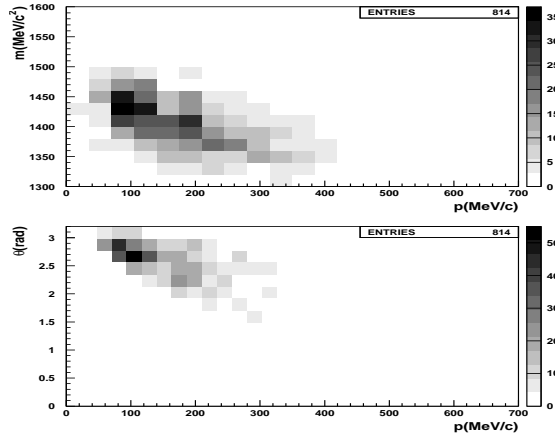


Figure 5.5: Top $m_{\Sigma^0\pi^0}$ vs $p_{\Sigma^0\pi^0}$, bottom $\theta_{\Sigma^0\pi^0}$ vs $p_{\Sigma^0\pi^0}$.

Similarly to figure 4.12 the HM component is correlated with lower masses and smaller angles, this could be kinematically interpreted as a lower mass object

corresponding to the production of higher momentum $\Sigma^0\pi^0$ couples with smaller $\theta_{\Sigma^0\pi^0}$ angles. A higher mass low momentum object is related to greater $\theta_{\Sigma^0\pi^0}$ angles. The observed relation between the kinematical variables was also tested representing $p_{\Sigma^0\pi^0}$ and $m_{\Sigma^0\pi^0}$ as a function of the pion kinetic energy T_{π^0} (figure 5.6).

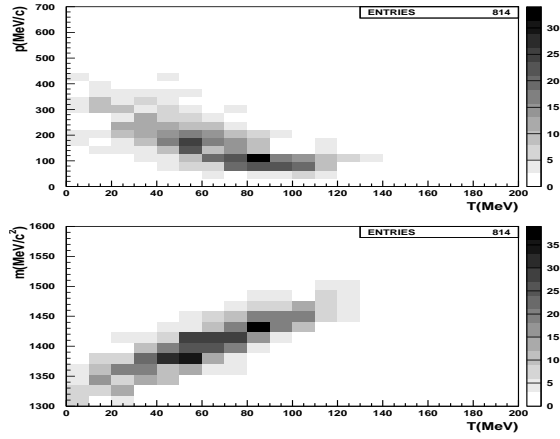


Figure 5.6: Top $p_{\Sigma^0\pi^0}$ vs T_{π^0} , bottom $m_{\Sigma^0\pi^0}$ vs T_{π^0} .

The LM $p_{\Sigma^0\pi^0}$ component is associated with an enhancement at $T_{\pi^0} \sim 80\text{MeV}$ corresponding to higher $m_{\Sigma^0\pi^0}$ values, while the HM $p_{\Sigma^0\pi^0}$ component is associated with $T_{\pi^0} \sim 50 - 60\text{MeV}$ and lower $m_{\Sigma^0\pi^0}$ values. The resolution in the kinetic energy of the pion $\sigma_{T_{\pi^0}}$ was checked by means of MC true information, and turns to be $11.7 \pm 0.2\text{MeV}$.

5.6 Comparison of the observed spectra with Helium bubble chamber experiments

When analyzing K^- absorptions in Carbon of the DC entrance wall, a contribution of in flight absorptions was first evidenced by means of a missing mass analysis (see section 4.6). Such result was then confirmed by a comparison of π^0 and $\Sigma^0\pi^0$ spectra with emulsion experiments in section 4.8, and a rough separation of in

flight from at rest reactions was achieved by selecting events based on the mass limit at rest. For what concerns K^- interactions in the DC gas a missing mass analysis can not be performed due to the important contribution of Carbon. In this section we will analyze the p_{π^0} and T_{π^0} distributions in light of the results reported in [33] and [34] and summarized in section 1.3.2, similar conclusions respect to the DC entrance wall events will be reached.

In figure 5.7 the momentum and kinetic energy distributions of the selected π^0 s are shown. No enhancement is present in p_{π^0} around $240\text{MeV}/c$ nor at $T_{\pi^0} \sim 130\text{MeV}$, this indicating that no important background of π^0 s from direct $\Lambda\pi^0$ production survives our selection. An extensive study will be described in section 5.8 confirming this qualitative observation.

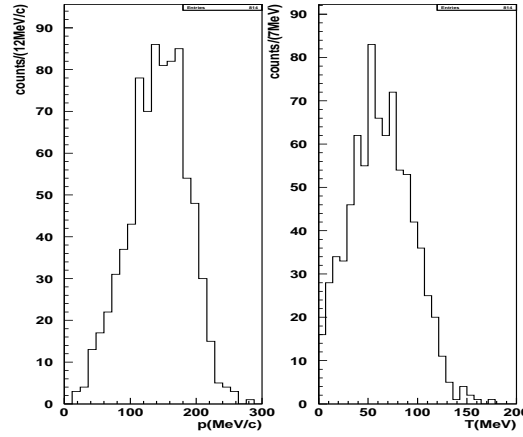


Figure 5.7: plot showing the p_{π^0} (left) and T_{π^0} (right) distributions.

In figure 1.8 the T_{π^-} distribution, for $K^- {}^4\text{He} \rightarrow \Sigma^0 \pi^- {}^3\text{He}$ events, shows a peak in the interval $40 - 70\text{MeV}$, also evident in our T_{π^0} distribution. A difference arising in 5.7 is the excess of values over the kinematical limit for absorptions at rest ($\sim 74\text{MeV}$). The observed higher T_{π^0} events are correlated with the LM $p_{\Sigma^0\pi^0}$ component and with masses above the kinematical limit for K^- absorptions at rest in Helium (see figure 5.6). In view of figure 1.9 the high T_{π^0} events can be naturally explained as $K^- {}^4\text{He} \rightarrow \Sigma^0 \pi^0 {}^3\text{H}$ productions in flight, for $p_k \sim 100\text{MeV}/c$ (corresponding to the mean p_k value at the track last point).

MC simulations support this interpretation. The whole sample of selected $\Sigma^0\pi^0$ events was divided in two subsamples, for $m_{\Sigma^0\pi^0}$ values lower or greater than the kinematical limit for K^- absorptions in Helium at rest of $1412\text{MeV}/c^2$. The corresponding T_{π^0} distributions are represented in black in figure 5.8 left for $m_{\Sigma^0\pi^0} < 1412\text{MeV}/c^2$ and right for $m_{\Sigma^0\pi^0} > 1412\text{MeV}/c^2$, compared with the relative MC spectra in green (at rest left and in flight right). The $m_{\Sigma^0\pi^0} < 1412\text{MeV}/c^2$ sample is referred to non-resonant quasi free simulated K^- absorptions at rest. The $m_{\Sigma^0\pi^0} > 1412\text{MeV}/c^2$ sample is referred to non-resonant quasi free simulated K^- absorptions in flight (both $K^- {}^4\text{He} \rightarrow \Sigma^0 \pi^0 {}^3\text{H}$ and $K^- \text{C} \rightarrow \Sigma^0 \pi^0 {}^{11}\text{B}$ interactions were generated for the two samples). The same cuts on $m_{\Sigma^0\pi^0}$ were also applied to MC events. Data and simulated events are normalized to unity.

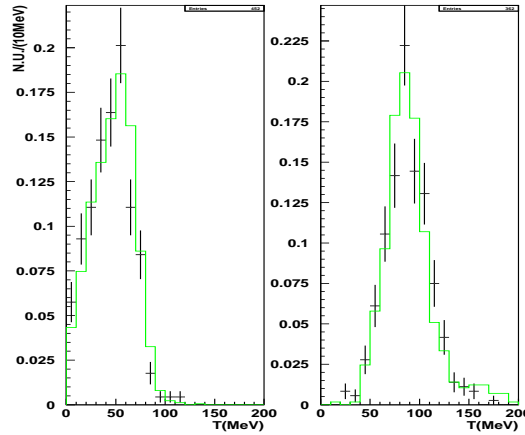


Figure 5.8: The T_{π^0} observed distribution (black) for $m_{\Sigma^0\pi^0} < 1412\text{MeV}/c^2$ (left) and $m_{\Sigma^0\pi^0} > 1412\text{MeV}/c^2$ (right) is compared to the corresponding MC distributions of pure at-rest (left) and pure in flight (right) events, as described in the text.

The reasonable agreement of data with MC confirms our interpretation of the observed correlations (simultaneously in different kinematical variable scatterplots) in complete analogy with the conclusions obtained for absorptions in the DC entrance wall. Events corresponding to the LM $p_{\Sigma^0\pi^0}$ component are characterised by higher $m_{\Sigma^0\pi^0}$ values (above the kinematical limit for absorptions at rest) and a T_{π^0} distribution compatible with absorptions in flight. The HM $p_{\Sigma^0\pi^0}$ component

is related to lower $m_{\Sigma^0\pi^0}$ values (below the kinematical limit for absorptions at rest) and the T_{π^0} characteristics of absorptions at rest.

Indicating with $m_{lim} = 1412 \text{ MeV}/c^2$ the kinematical limit, a lower limit for the ratio of in flight over at rest events can be roughly estimated:

$$\frac{n_{>m_{lim}}}{n_{<m_{lim}}} = 0.82 \pm 0.06, \quad (5.15)$$

it results to be slightly higher respect to absorptions in the wall.

To conclude this section let us describe a test performed to check a possible influence of the small ϕ boost on the $p_{\Sigma^0\pi^0}$ spectrum, investigated by using the information of the kaon momentum p_k . In each $\Sigma^0\pi^0$ selected event a K^- track was searched tagged by dE/dx . Only sufficiently long tracks are identified by the KLOE reconstruction algorithm, that is when the absorption occurs sufficiently far from the DC entrance wall. Such correlation between the distance of the $\Lambda(1116)$ decay vertex from the origin and the length of the K^- track is shown in figure 5.9.

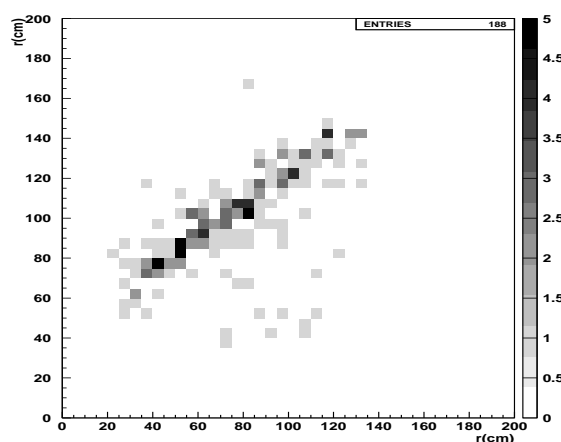


Figure 5.9: Plot representing the distance of the $\Lambda(1116)$ decay vertex from the origin as a function of the length of the K^- track.

As a consequence a kaon track is available in about 20% of total events. For such events the K^- momentum at the last point of the track is represented in figure 5.1, the p_k distribution shows a double peak (due to the ϕ boost) for about

$90\text{MeV}/c$ and $110\text{MeV}/c$. In order to check possible influences of the boost on $p_{\Sigma^0\pi^0}$ the entire sample was divided in two subsamples ($p_k > 100\text{MeV}/c$ and $p_k < 100\text{MeV}/c$). The corresponding $p_{\Sigma^0\pi^0}$ distributions for the two subsamples (black for lower momentum kaons, red for higher momentum kaons) is shown in figure 5.10. Despite the low statistics in both samples a structuring emerges corresponding to $p_{\Sigma^0\pi^0 LM}$ and $p_{\Sigma^0\pi^0 HM}$ (excluding any correlation with the ϕ boost). Moreover the $p_{\Sigma^0\pi^0 LM}$ appears shifted of about $20\text{ MeV}/c$ in the two samples (as a consequence of the p_k difference). This is exactly what is expected if the $p_{\Sigma^0\pi^0 LM}$ events are generated in flight.

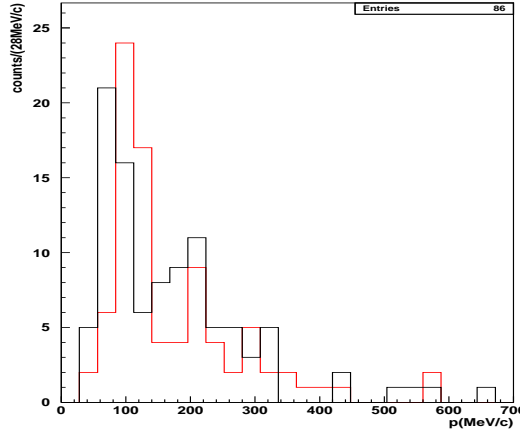


Figure 5.10: $p_{\Sigma^0\pi^0}$ distribution for lower (black) and higher (red) p_k values.

5.7 Search for an extra-track coming from the K^- interaction point

We will describe in this section an attempt to identify a further track coming from the hadronic interaction vertex of the $\Sigma^0\pi^0$ couples. Finding eventual triton tracks associated to the $\Sigma\pi$ formation and possibly the association of the track with a cluster in the calorimeter, would open the possibility of a missing mass analysis for the $\Sigma^0\pi^0$ channel.

Tracks of positive charge are searched which were not already identified as a K^+ , as positive pions or muons from tagged two body K^+ decay ($K^+ \rightarrow \pi^+\pi^0, \mu^+\nu$) or protons associated to the $\Lambda \rightarrow p\pi^-$ decay vertex.

The next step consists in a series of alternative cuts in the dE/dx vs p plane. The track is retained if the relation between the truncated mean of the energy released on the wires of the chamber and the corresponding momentum, satisfies alternatively one of the following relations:

- $\frac{dE}{dx} > 200 e^{-\frac{p}{200 (MeV/c)}} + 5$ or
- $\frac{dE}{dx} > 200 e^{-\frac{p}{350 (MeV/c)}} - 25$ or
- $\frac{dE}{dx} > 400 e^{-\frac{p}{120 (MeV/c)}} + 10$.

The previous cuts were optimized with the aim of selecting protons and nuclear fragments by using all the $\Lambda(1116)$ reconstructed events (let us notice indeed that the nuclear fragmentation is less probable in case of a $\Sigma\pi$ identification, which excludes the possibility of internal conversion and multinucleon absorption, whose branching ratio in Helium is $\sim 20\%$)

The hadronic interaction point is searched by a backwards extrapolation of the $\Lambda(1116)$ straight path, together with the charged track. The minimization procedure also takes into account (for charged particles) of eventual energy loss in the crossed materials and changes in the trajectory. If the minimization procedure succeeds and the minimum distance between the track and lambda extrapolations is smaller than $5cm$, then the extra-track is accepted.

The angular distribution $\cos(\theta_{\Sigma^0\pi^0,t})$ between the momentum of the emerging $\Sigma^0\pi^0$ couple and the momentum of the extra-track is then calculated. To this end the extrapolated \mathbf{p}_t momentum at the hadronic interaction point was used. The $\cos(\theta_{\Sigma^0\pi^0,t})$ spectrum is represented in figure 5.11.

Despite the poor statistics, a clear peak is evident around $\cos(\theta_{\Sigma^0\pi^0,t}) \sim -1$, corresponding to a back-to-back production of the extra-track with respect to the $\Sigma^0\pi^0$ couple. These can be identified as triton tracks produced at rest in $K^- + {}^4He \rightarrow \Sigma^0\pi^0 + {}^3H$ absorptions.

The back-to-back tracks ($\cos(\theta_{\Sigma^0\pi^0,t}) \leq -0.75$), all longer than $50cm$, are associated to high $p_{\Sigma^0\pi^0}$ values, and low $m_{\Sigma^0\pi^0}$ masses, as a further confirmation that this region of the $m_{\Sigma^0\pi^0} - p_{\Sigma^0\pi^0}$ plane is associated to at rest interactions.

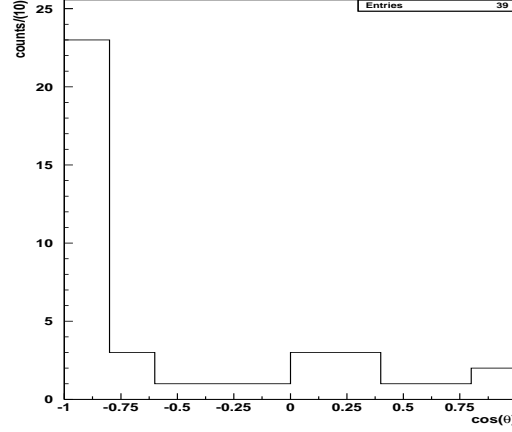


Figure 5.11: Plot representing the $\cos(\theta_{\Sigma^0\pi^0,t})$ distribution for all the identified extra-tracks.

In figure 5.12 the $m_{\Sigma^0\pi^0}$ (left black) and $p_{\Sigma^0\pi^0}$ (right black) spectra are shown for the $\cos(\theta_{\Sigma^0\pi^0,t}) \leq 0.75$ events. In the left in green is also represented the missing mass distribution (obtained assuming the interaction at rest and the triton mass hypothesis) the green points are plotted with a different binning respect to the black ones (counts/(15MeV/c²) in spite of counts/(30MeV/c²)) evidencing a much better resolution.

Even if, unluckily, only few extra-tracks (among the selected ones) are associated to a cluster in the calorimeter, this powerful tool will be useful in future higher statistics analysis. Using the momentum of the extra-track, with the triton mass hypothesis, when it fulfills the angular condition $\cos(\theta_{\Sigma^0\pi^0,t}) < -0.75$, will allow to perform missing mass studies, with higher resolution. Moreover, if the extra-track would be associated to a cluster in the calorimeter, the kinematics of the event could be closed.

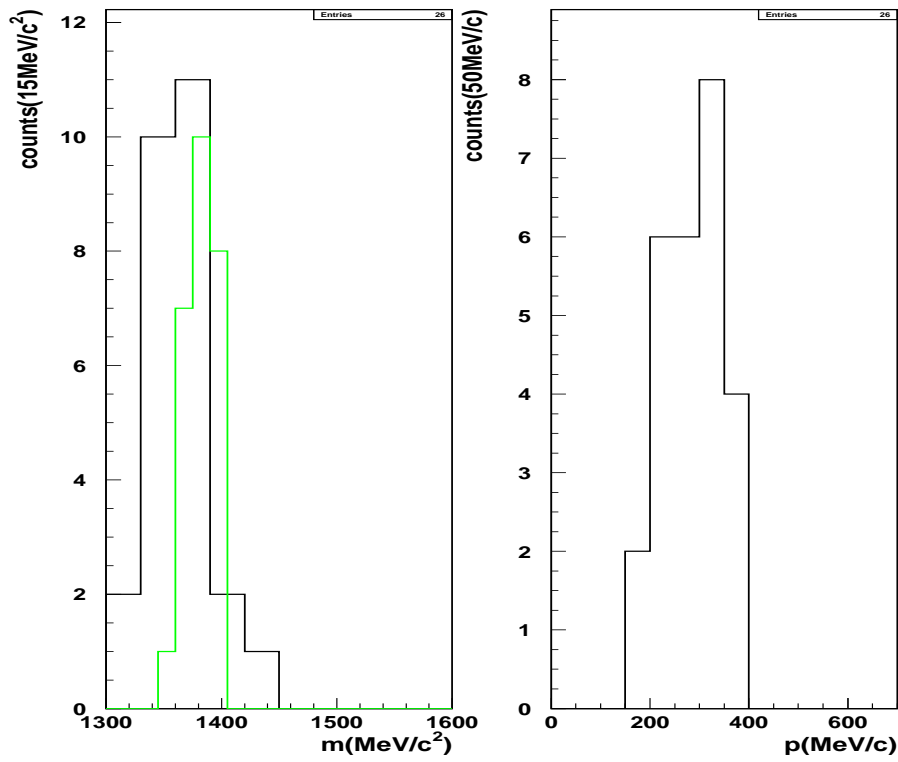


Figure 5.12: $m_{\Sigma^0\pi^0}$ (left black) (binning: counts/(30MeV/c²)), mm (left green) (binning: counts/(15MeV/c²)), $p_{\Sigma^0\pi^0}$ (right black).

5.8 Analysis of the background: $\Sigma(1385)$ and internal conversion events

As already described in 4.10, the main background sources which affect the channel under study are the $\Sigma(1385)$ events and internal conversion. In the following sections we will briefly summarise the results of the same tests outlined in section 4.10, together with a MC estimate of the background contribution.

5.8.1 γ_3 clusters characterization

The background sources, $\Sigma(1385) \rightarrow \Lambda\pi^0$ and internal conversion events, are characterised by the same final state topology and the absence of a third photon (γ_3). First we then tested differences in the characteristics of the neutral cluster which the reconstruction associates to γ_3 with respect to γ_1 and γ_2 . The time distributions for prompt photons selected by χ_t^2 and $\chi_{\Sigma\pi}^2$ minimizations does not exhibit differences.

In figure 5.13 the energy distribution of the couples γ_1 and γ_2 is plotted in black, together with the energy spectrum of γ_3 in green. E_{γ_3} is compared with the same distribution obtained for a MC simulation of pure signal events. The simulated K^- nuclear interactions with a proton in the nucleus give rise to the resonant formation of $\Lambda(1405)$ (center and width of the adopted relativistic Breit-Wigner distribution are taken in accordance with the PDG values $m_0 = 1405.1 \text{ MeV}/c^2$ and $\Gamma = 50 \text{ MeV}/c^2$) following the reactions:

$$K^- He \rightarrow \Lambda(1405) {}^3H \rightarrow \Sigma^0 \pi^0 {}^3H, \quad (5.16)$$

$$K^- C \rightarrow \Lambda(1405) {}^{11}B \rightarrow \Sigma^0 \pi^0 {}^{11}B, \quad (5.17)$$

in a quasi-free fashion with the residual nucleus (triton or boron) behaving like a spectator (secondary interactions of the produced Σ^0 and π^0 with the residual nucleus were neglected). The K^- absorptions are generated in the inner volume of the KLOE DC and energy loss effects for charged particles, in crossing the KLOE materials, are taken into account. Both K^- interactions at rest and in flight are considered. The E_{γ_3} MC distribution well reproduces the spectrum for data, similar to figure 4.24 for absorptions in the wall.

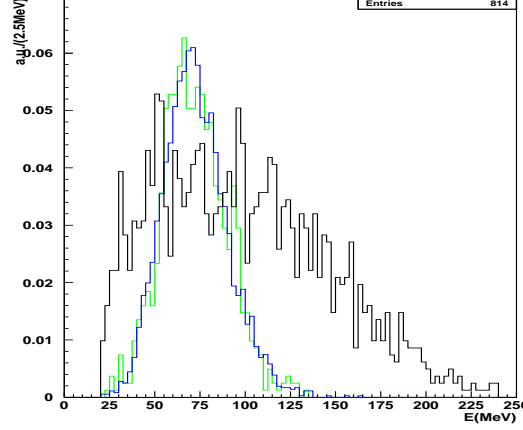


Figure 5.13: Energy distribution of the couples γ_1 and γ_2 (black) together with the energy spectrum of γ_3 (green). The blue curve represents the reconstructed E_{γ_3} distribution for pure signal MC events as described in the text.

In order to check possible differences arising between the LM and HM components in the observed $p_{\Sigma^0\pi^0}$ spectrum, the whole sample of data was roughly divided into two subsamples according to $p_{\Sigma^0\pi^0}$ greater or less than $150\text{MeV}/c$. No difference was found in the t_{γ_3} and E_{γ_3} distributions for the two samples.

5.8.2 Study of the Λ momentum distribution.

A powerful tool to evidence an eventual contribution of $\Sigma(1385)$ to the final selected events is given by the study of the Λ momentum, employing the great mass difference between the Σ^0 ($1192.642 \pm 0.024\text{MeV}/c^2$) and the $\Sigma(1385)$ ($1383.7 \pm 1.0\text{MeV}/c^2$). The Σ^0 decays, in its rest frame, in $\Lambda\gamma_3$ pairs with a momentum of $74\text{MeV}/c$, while the $\Sigma(1385)$ would decay into $\Lambda\pi^0$ pairs characterized by a momentum of $208\text{MeV}/c$. We transformed the measured p_Λ momentum in the CM frame of $\Lambda\gamma_3$, making the assumption that γ_3 was correctly identified. The obtained distribution for $p_{\Lambda\gamma_3\text{CM}}$ is shown in figure (5.14) in black, together with the same distribution for pure signal MC events in green (the simulations were performed according to the specifications given in section 5.8.1). The agreement

between data and simulation confirms the low contribution of $\Sigma(1385)$ events. A Gaussian fit to the black distribution was also performed and a mean value ($p_{\Lambda\gamma_3 CM} = 74.3 \pm 0.8$) MeV/c was found.

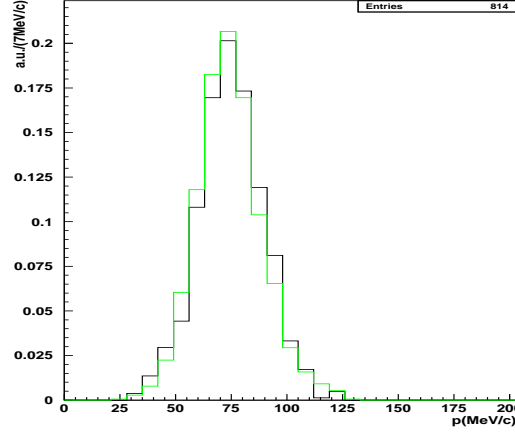


Figure 5.14: The $p_{\Lambda\gamma_3 CM}$ distribution is represented in black together with the same distribution for pure signal MC events (green) as described in the text.

Pure background MC simulations were then used to check the consistency of the previous result. In the simulation K^- nuclear absorption always gives rise to the quasi-free resonant formation of $\Sigma(1385)$ (the residual nucleus is treated as a spectator of the reaction and secondary interactions of the produced Σ^0 and π^0 with the residual nucleus were neglected). The same dedicated algorithm for the reconstruction of $\Lambda\pi^0$ events (introduced in section 4.10.2) was then applied to the MC Ntuples, and the Λ momentum was transformed in the CM frame of $\Lambda\pi^0$. The calculated distribution (shown by the green curve in figure 5.15) is peaked around the expected value of $208 MeV/c$. The black curve in 5.15 represents the same calculation performed for the measured p_Λ values (that is assuming a misidentification of γ_3 in data analysis). The data clearly differ from the MC spectrum.

To conclude this set of tests, also the measured momentum of the Σ^0 was transformed in the rest frame of $\Sigma^0 - \pi^0$. According to PDG the $\Lambda(1405)$ is expected to decay in its rest frame in $\Sigma^0 - \pi^0$ pairs characterized by a momentum

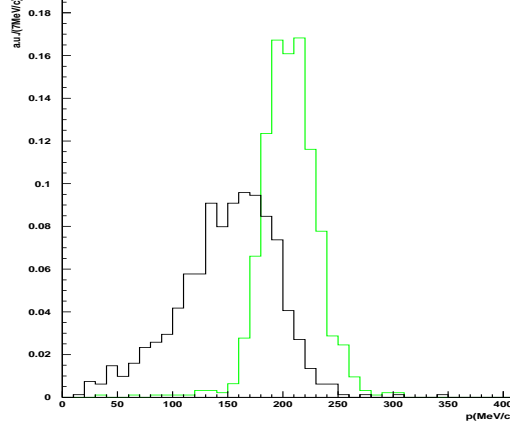


Figure 5.15: The $p_{\Lambda\pi^0 CM}$ distribution is represented in black together with the same distribution for pure $\Sigma(1385)$ background MC events (gren) as described in the text.

of $155 MeV/c$. The result of a Gaussian fit to the obtained $p_{\Sigma^0\pi^0 CM}$ spectrum is $(p_{\Sigma^0\pi^0 CM} = 154.2 \pm 1.8) MeV/c$, $(\sigma_{p_{\Sigma^0\pi^0 CM}} = 36.5 \pm 1.2) MeV/c$.

5.8.3 Estimate of the $\Lambda\pi^0$ contribution to the final selected sample.

The estimate of the $\Lambda\pi^0$ background passing the analysis cuts and contributing to the final $\Sigma^0\pi^0$ spectrum, was performed following the same procedure developed in section 4.10.3. MC simulations of pure signal and pure background events were generated as described in the previous sections. Both signal and background Ntuples were processed with the same reconstruction algorithm, following the events selection prescription described in chapter 3. The adopted branching fraction for $\Lambda\pi^0$ and $\Sigma^0\pi^0$ channels produced in $K^- He$ absorptions (according to [33]) are summarized in table 5.2.

The branching fractions reported in table 5.2 also take into account for the internal conversion probability ($\Sigma^0 N \rightarrow \Lambda N$). The weighted percentage of $\Lambda\pi^0$ contamination in the observed spectra was then estimated to be 0.03 ± 0.02 . The high error is mainly a consequence of the uncertainty in $BR(\Sigma^0\pi^0)$.

Table 5.2: Branching fraction for $\Lambda\pi^0$ and $\Sigma^0\pi^0$ production following K^- absorption in Helium, according to [33].

	$\Lambda\pi^0$	$\Sigma^0\pi^0$
<i>B.R.</i>	0.163 ± 0.023	0.062 ± 0.048

5.9 $m_{\Sigma^0\pi^0}$ spectrum obtained with mass hypothesis

In the course of the analysis presented in Chapters 4 and 5 a strict analogy was generally outlined, between the $\Sigma^0\pi^0$ production due to K^- absorption on Carbon and Helium. The features of the observed $m_{\Sigma^0\pi^0}$ and $p_{\Sigma^0\pi^0}$ spectra were interpreted, with the help of similar experimental results obtained in emulsion and bubble chamber experiments, in view of the different production mechanisms (in flight and at rest capture) contributing to the final shapes. Such interpretation is confirmed by the preliminary analysis of a subsample of the data collected by stopping negative kaons, in a high purity Carbon (graphite) target (see section 4.9). The similarity of Carbon and Helium events is not completely unexpected, especially considering the similar last nucleon binding energy (which turns in similar thresholds for the $m_{\Sigma^0\pi^0}$) (see section 1.3.1) and the possibility to describe Carbon nuclei by cluster-model wave functions, with three α clusters in the ground state. Recently light hyper-nuclei were well described based on cluster wave functions [46].

In this last section the invariant mass spectra for K^- captures in the DC wall and DC gas will be presented, obtained assuming the Σ^0 and π^0 masses according to their PDG values ($m_{\Sigma^0} = 1192.65 \pm 0.020 \pm 0.014$ and $m_{\pi^0} = 134.9766 \pm 0.0006$). As described in Chapter 3 we are rather confident to suppress any $p - \pi^-$ accidental pairing, with the subsequent identification of a π^0 and a γ in time from the interaction vertex. The mass hypothesis is then only incorrect when a misidentification of the photon triple ($\gamma_1, \gamma_2, \gamma_3$) occurs, and a misidentification probability of 0.22 ± 0.01 was estimated by MC true information. To take into account for this effect dedicated MC simulations were performed, in which the observed $m_{\Sigma^0\pi^0}$ and $p_{\Sigma^0\pi^0}$ lineshapes, determined from the data, were used as input for generating

Monte Carlo events. Distinct simulations were performed for K^- absorptions in the DC entrance wall and in the gas filling the DC volume, employing the corresponding $m_{\Sigma^0\pi^0}$ and $p_{\Sigma^0\pi^0}$ spectra. The *non resonant misidentification* distributions are then obtained selecting those simulated events in which the $(\gamma_1, \gamma_2, \gamma_3)$ triple is *not* correctly recognized (according to true MC information).

In figure 5.16 the $m_{\Sigma^0\pi^0}$ spectra, calculated with mass hypothesis for m_{Σ^0} and m_{π^0} , are shown in blue for absorptions in the DC gas, in black for absorptions in the DC wall, normalized to unity. The green and magenta points represent the non resonant misidentification spectra (normalized to 0.22) for K^- absorptions in the gas and the wall respectively.

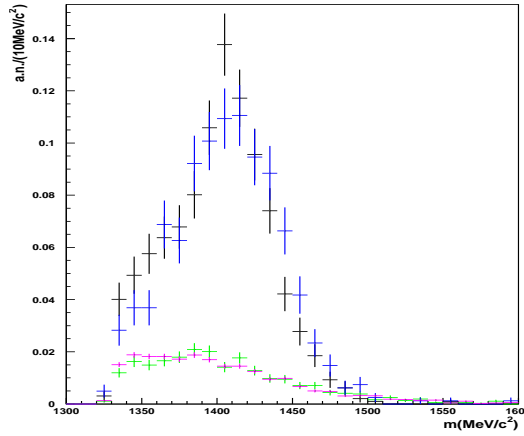


Figure 5.16: $m_{\Sigma^0\pi^0}$ spectrum calculated with mass hypothesis for m_{Σ^0} and m_{π^0} , the blue points refer to absorptions in the DC gas, the black points to absorptions in the DC wall, the green and magenta points represent the normalized non resonant misidentification contributions in the gas and the wall respectively.

The same background subtracted spectra are shown in figure 5.17. According to MC true information, the invariant mass resolution improves to $\sim 17\text{MeV}/c^2$ for absorptions in the wall and $\sim 15\text{MeV}/c^2$ for absorptions in the gas, when the mass hypothesis on m_{Σ^0} and m_{π^0} is introduced.

The blue and black spectra are consistent within the errors, except few points. Both are characterized by a lower mass enhancement and a higher mass shoulder.

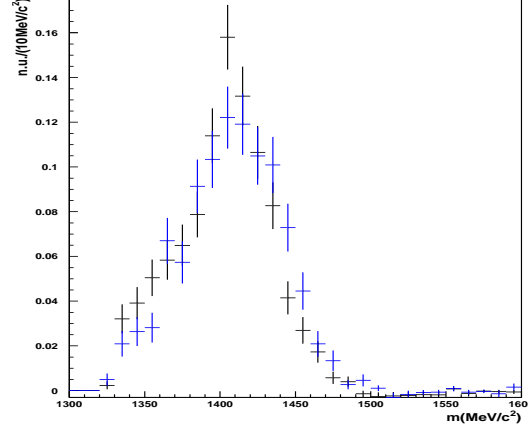


Figure 5.17: $m_{\Sigma^0\pi^0}$ spectrum calculated with mass hypothesis for m_{Σ^0} and m_{π^0} , the blue points refer to absorptions in the DC gas, the black points to absorptions in the DC wall. Both spectra are background subtracted.

The lineshapes are similar to the corresponding one obtained in the Λ^* photoproduction experiment in [22] for the $\Sigma^0\pi^0$ channel.

In figure 5.18 are represented the scatterplots $m_{\Sigma^0} - p_{\Sigma^0}$ for absorptions in the gas (top), and the wall (bottom) where $m_{\Sigma^0\pi^0}$ is obtained with mass hypothesis for m_{Σ^0} and m_{π^0} . Both are characterized by enhancements corresponding to the LM and HM $p_{\Sigma^0\pi^0}$ components.

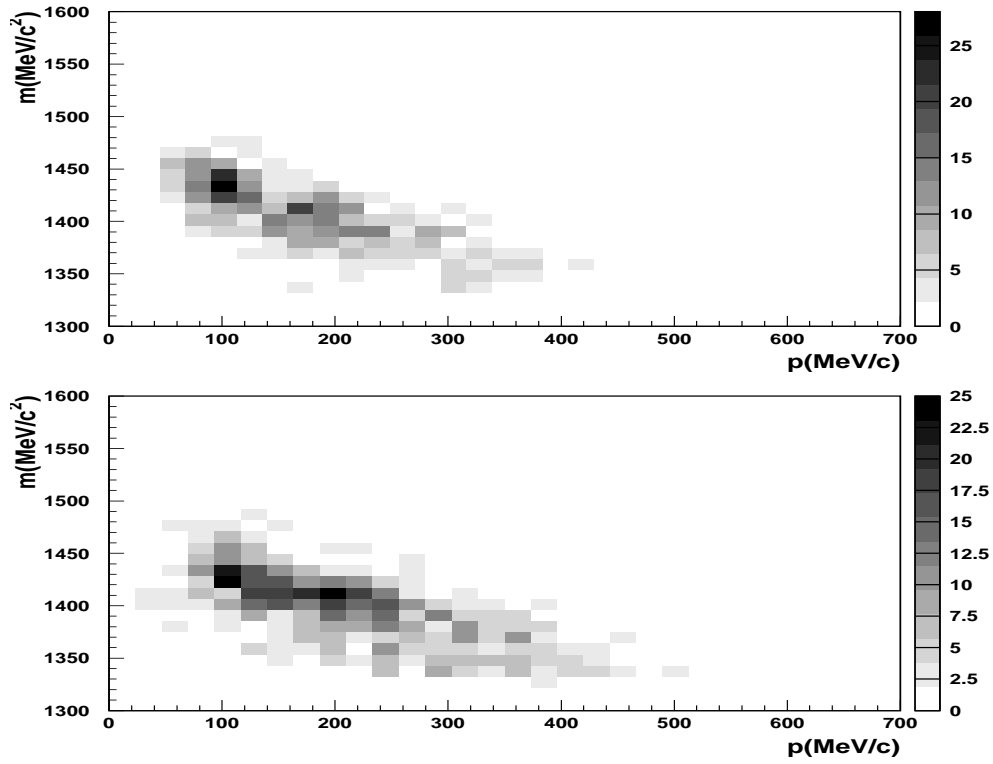


Figure 5.18: $m_{\Sigma^0} - p_{\Sigma^0}$ for absorptions in the gas (top), and the wall (bottom) where $m_{\Sigma^0\pi^0}$ is obtained with mass hypothesis for m_{Σ^0} and m_{π^0} .

Chapter 6

Fit of the observed distributions

6.1 Introduction

In the course of previous chapters a great effort was devoted to the characterization of the $\Sigma^0\pi^0$ spectra (produced in both K^- absorptions in Helium and Carbon) leading to a comprehension of the different features giving rise to the observed shapes. The upper limit of the $m_{\Sigma^0\pi^0}$ is mainly determined by the kinematical threshold characteristic of the absorbing target, as a consequence of the binding energy of the interacting nucleon (see section 4.3) and the momentum of the absorbed kaon (see sections 4.6, 4.8, 5.6 and 5.7). An unavoidable enlargement is introduced in the $m_{\Sigma^0\pi^0}$ spectrum by the instrumental resolution, whose dominant component is the energy resolution for neutral clusters in the KLOE calorimeter, as described in sections 5.5 and 4.7, together with a small energy loss effect which p and π^- undergo in crossing the DC entrance wall and the DC gas (4.4, 5.4).

The disadvantage introduced by the limiting resolution is nevertheless completely compensated by the unique opportunity to select a clean $\Sigma^0\pi^0$ $I = 0$ sample, free from the $\Sigma(1385)$ $I = 1$ contamination, and from the high probability internal conversion competing mechanism. Thanks to the good performances of the selecting algorithms, the physical $\Lambda\pi^0$ background accounts for $3\% \pm 1\%$ (for absorptions in the wall) $3\% \pm 2\%$ (for absorptions in the gas) of the selected events (sections 4.10 and 5.8), together with a $22\% \pm 1\%$ misidentification non-resonant background, to be taken into account when employing the m_{Σ^0} and m_{π^0} hypothesis for $m_{\Sigma^0\pi^0}$.

In order to perform a reliable fit of the obtained $m_{\Sigma^0\pi^0}$ spectrum, testing the theoretical predictions outlined in Chapter 1 and previous findings in similar experimental conditions, each described effect was taken into account. The kinematics of the $\Sigma^0\pi^0$ pairs was calculated for both K^- absorptions in Helium and Carbon (in the DC wall or the DC internal volume), for each component of the fit, considering both interactions at rest and in flight and is used as input for the KLOE GEANT simulation. The simulation takes into account for the energy loss of charged particles in the crossed KLOE materials. The event generation is then followed by the reconstruction of the tracks and clusters in the KLOE detector, taking into account for acceptance and resolution effects, as described in section 4.3. To conclude, the simulated events are processed by the same reconstruction algorithm (Chapter 3) optimised for data.

A second difficulty to deal with is represented by the presence of many different components to be taken into account in the fitting procedure, namely:

- different possible pole positions and resonance widths,
- the contribution of the non resonant $\Sigma^0\pi^0$ production.

As first we then decided to generate many resonant poles for the K^-p interaction, performing a mass scan from $1381 \text{ MeV}/c^2$ to $1430 \text{ MeV}/c^2$, with a step of $\sim 10 \text{ MeV}/c^2$. The important case of the $\Lambda(1406) \Gamma = 23 \text{ MeV}/c^2$ [18] was also tested. A Breit-Wigner mass distribution was assumed simulating different widths for each assumed mass value, around the expected (theoretical or experimental) value. A more refined scan was then performed between $1422 \text{ MeV}/c^2$ and $1430 \text{ MeV}/c^2$, interval in which the $\frac{\chi^2}{ndf}$ greatly improved, also attempting to estimate the uncertainty on the best fitting mass and width values. Specific algorithms were developed, interfaced to the CERN fitting package MINUIT. The presence of such a great number of components and the need to reduce the statistical error, required the simulation of several millions of MC events.

The next section is devoted to the description of the fitting algorithm.

6.2 The fitting algorithm

A multi-component fit to the observed $m_{\Sigma^0\pi^0}$ distribution, obtained assuming the correct masses for Σ^0 and π^0 was performed, the better resolution is crucial to

distinguish the similar shapes of the different components. As a first step the histograms of the distributions for data and for the simulated components are taken as input. The same binning is imposed for corresponding data and simulation plots. The limits and binning were optimised in order to have the maximum available statistics in each bin (without loosing information) compatible with the resolutions. Data input bins are required to have at least five entries. The bin content, for each distribution is then passed to the following function to be minimized

$$\chi^2 = \sum_i \frac{(\sum_{\alpha} \alpha m_{\alpha i} + \beta m_{\Lambda\pi^0 i} + \gamma m_{nrm i} - m_i)^2}{\sigma^2} \quad (6.1)$$

In 6.1 α refers to the parameters for the various fitting components (resonant/non-resonant, at-rest/in-flight, C/He). The α parameters are let to freely vary with the condition that the ratio of the resonant over non resonant contribution is equal at rest and in flight, within the errors of the fit. β is a parameter which weights the total number of $\Lambda\pi^0$ events and is let to vary around 3% of the observed events within the estimated uncertainty (see section 4.10.3). γ sets the contribution of the non resonant misidentification (*n. r. m.*) and is let to vary around 22% of the observed events within the estimated uncertainty (section 3.7). $m_{\alpha i}$ is the bin content of the i th bin of the invariant mass distribution, for the α th simulated component. $m_{\Lambda\pi^0 i}$, $m_{nrm i}$ and m_i refer the corresponding bin content for $\Lambda\pi^0$ events, *n. r. m.* and data respectively. A recursive minimization of the function introduced in 6.1 is performed using the SIMPLEX and MIGRAD routines, the minimizing α parameters will represent the best fitting component contributions to data. It is important to stress that $m_{\Lambda\pi^0 i}$ *does not* represent the $\Lambda\pi^0$ invariant mass, but instead the $\Sigma^0\pi^0$ invariant mass when a $\Sigma^0\pi^0$ pair was misidentified in pure background $\Lambda\pi^0$ events.

6.3 Single resonant pole component fits to the DC entrance wall events

We will summarize in this section the fit results for the observed K^- absorptions in the KLOE DC entrance wall. We will adopt the following convention to indicate the simulated invariant mass distributions:

$$\Lambda(1405, 50) \tag{6.2}$$

the first value in brackets representing the invariant mass of the resonance, the second value denotes the width of the corresponding adopted relativistic Breit-Wigner mass distribution.

In table 6.1 are listed the obtained results of the fit performed with a simulated resonance $\Lambda(1405.1, 50)$, as reported in [4]. The first line shows the $\frac{\chi^2}{ndf}$, the following lines of the table are the percentages of the various α components resulting from the fit, namely:

- a $\Lambda(1405.1, 50)$ resonance generated by K^- absorptions in Carbon at rest,
- a $\Lambda(1405.1, 50)$ resonance generated by K^- absorptions in Carbon in flight,
- a non resonant $\Sigma^0\pi^0$ component generated by K^- absorptions in Carbon at rest,
- a non resonant $\Sigma^0\pi^0$ component generated by K^- absorptions in Carbon in flight.
- non resonant $\Sigma^0\pi^0$ component due to photons misidentification.
- $\Lambda\pi^0$ background due to $\Sigma(1385)$ or internal conversion events.

From the values listened in table 6.1 a dominance of the non resonant component emerges. In particular the $\Lambda(1405.1, 50)$ in flight component does not reproduces the high $m_{\Sigma^0\pi^0}$ observed masses, which are better fitted by the non resonant $\Sigma^0\pi^0$ in flight component.

As mentioned in 1.2, the $\Sigma^\pm\pi^\mp$ invariant mass spectra obtained by Riley et al. [17] were fitted in [18] assuming both resonant and non-resonant $\Sigma^\pm\pi^\mp$ productions, together with a $\Sigma(1385)$ contribution. Due to the similarity of the $\Sigma^\pm\pi^\mp$ production mechanism adopted in [17], a comparison with our data is interesting. We then decided to fit our $m_{\Sigma^0\pi^0}$ distribution with a simulated resonance $\Lambda(1405.5, 23.6)$, corresponding to the best fit obtained by Esmaili, Akaishi and Yamazaki. The results are shown in table 6.2.

The narrower width, respect to the $\Lambda(1405.1, 50)$ pole, traduces in a stronger contribution of the resonant in flight contribution, nevertheless the non resonant in

Table 6.1: Fit to the DC entrance wall events with a $\Lambda(1405.1, 50)$ as described in the text.

$\frac{\chi^2}{ndf} = 4.5$	
$\Lambda(1405.1, 50)$ at rest	0.18 ± 0.04
$\Lambda(1405.1, 50)$ in flight	0.07 ± 0.05
n. r. $\Sigma^0\pi^0$ at rest	0.23 ± 0.01
n. r. $\Sigma^0\pi^0$ in flight	0.25 ± 0.04
n. r. m.	0.23 ± 0.01
$\Lambda\pi^0$	0.04 ± 0.01

flight component (which is cut just below the kinematical threshold, see figure 4.1) still gives a dominant contribution and accounts for masses above the kinematical limit at rest. A high $m_{\Sigma^\pm\pi^\mp}$ component is not present in the Riley et al. spectra, as the negative kaon is stopped in the Helium target and the energy region above $1412\text{MeV}/c^2$ is not allowed.

After the first (m, Γ) scan the best fit is obtained by assuming a $\Lambda(1426, 15)$ resonant component. We then decided to perform a finest scan varying the mass and width parameters, on a discrete grid, around the values $(m = 1426\text{MeV}/c^2, \Gamma = 15\text{MeV}/c^2)$. Each fit is performed, as described in 6.2, assuming six components:

- a $\Lambda(m, \Gamma)$ resonance generated by K^- absorptions in Carbon at rest,
- a $\Lambda(m, \Gamma)$ resonance generated by K^- absorptions in Carbon in flight,
- a non resonant $\Sigma^0\pi^0$ component generated by K^- absorptions in Carbon at rest,
- a non resonant $\Sigma^0\pi^0$ component generated by K^- absorptions in Carbon in flight.
- non resonant $\Sigma^0\pi^0$ component due to photons misidentification.
- $\Lambda\pi^0$ background due to $\Sigma(1385)$ or internal conversion events.

Table 6.2: Fit to the DC entrance wall events with a $\Lambda(1405.5, 23.6)$ as described in the text.

$\frac{\chi^2}{ndf} = 4.4$	
$\Lambda(1405.5, 23.6)$ at rest	0.06 ± 0.05
$\Lambda(1405.5, 23.6)$ in flight	0.29 ± 0.05
n. r. $\Sigma^0\pi^0$ at rest	0.03 ± 0.01
n. r. $\Sigma^0\pi^0$ in flight	0.35 ± 0.04
n. r. m.	0.23 ± 0.01
$\Lambda\pi^0$	0.04 ± 0.01

In table 6.3 are summarized the obtained χ^2 values for each simulated (m, Γ) parameters pair. The χ^2 values are plotted as a function of Γ for the different selected mass values in figure 6.1.

Table 6.3: χ^2 values obtained for different (m, Γ) parameters around $(m = 1426 MeV/c^2, \Gamma = 15 MeV/c^2)$.

$ndf = 10$ $m(MeV/c^2)$	$\Gamma(MeV/c^2)$	1	5	10	15	25	52
1422			25.9	19.4	20.0	40.6	
1426		27.7	20.3	15.1	11.6	13.9	38.2
1428		33.6			12.0	14.5	59.5
1430		34.1			14.8	18.0	

The $\chi^2 = \chi^2(\Gamma)$ curves were fitted with third degree polynomials and a global minimum was found $\chi^2_{min}/ndf = 11.6/10$ corresponding to the parameter values:

$$(m_{min}, \Gamma_{min}) = (1427, 18) MeV/c^2. \quad (6.3)$$

In order to understand the effect of the invariant mass resolution ($\sim 17 MeV/c^2$)

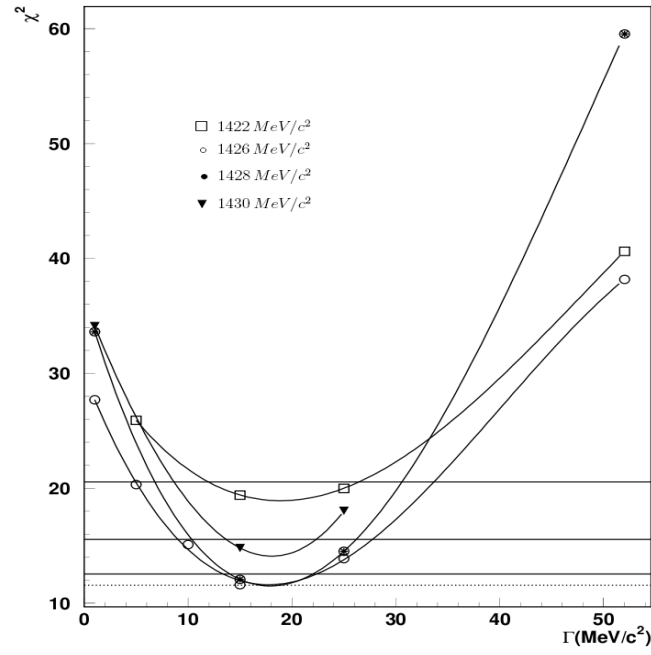


Figure 6.1: χ^2 as a function of the width Γ for the different simulated mass values: $1422 \text{ MeV}/c^2$ squares, $1426 \text{ MeV}/c^2$ open circles, $1428 \text{ MeV}/c^2$ filled circles, $1430 \text{ MeV}/c^2$ triangles. The points are fitted with third degree polynomials. Continuous lines indicate $\chi^2 = \chi^2_{min} + 1, +4, +9$, a dotted line represents $\chi^2 = \chi^2_{min}$.

on the estimated parameters and the corresponding uncertainties, the $\chi^2(\Gamma)$ curves were intersected with the lines $\chi^2 = \chi_{min}^2 + 1, +4, +9$. These are drawn as continuous lines in figure 6.1 together with a dotted line for $\chi^2 = \chi_{min}^2$. The intersection points are represented in figure 6.2 in the (Γ, m) plane. According to the maximum likelihood principle, if uniform priors were chosen for positive values of (Γ, m) and the m_i follow Gaussian distributions, then the probability distribution of the parameters is given by:

$$p(m, \Gamma | m_i) = e^{-\chi^2(m, \Gamma)}. \quad (6.4)$$

If we assume that the probability distribution for the (Γ, m) parameters is a bi-dimensional Gaussian, that is $\chi^2(m, \Gamma)$ has a parabolic shape, then the uncertainties on (Γ, m) can be estimated by the intervals on the m and Γ axis, determined by the tangents to the contour ellipses. Unfortunately only few points are available for the moment, and we are presently working to still refine the (Γ, m) grid. From the contour plot corresponding to the $\chi^2 = \chi_{min}^2 + 9$ cut we obtain:

$$m = 1427_{-6}^{+4} \text{ MeV}/c^2, \quad \Gamma = 18_{-13}^{+15} \text{ MeV}/c^2. \quad (6.5)$$

In figure 6.3 the fit to the observed $m_{\Sigma^0\pi^0}$ distribution, relative to K^- absorptions in the DC entrance wall, is shown using for the simulated resonant distributions, at rest and in flight, the parameters given in 6.5. The fractions of the various components resulting from the fit are listed in table 6.4.

Table 6.4: Fit to the DC entrance wall events with a $\Lambda(1427, 18)$ as described in the text.

$\Lambda(1427, 18)$ at rest	0.29 ± 0.05
$\Lambda(1427, 18)$ in flight	0.46 ± 0.05
n. r. $\Sigma^0\pi^0$ at rest	$0.00_{-0.00}^{+0.02}$
n. r. $\Sigma^0\pi^0$ in flight	$0.00_{-0.00}^{+0.05}$
n. r. m.	0.23 ± 0.01
$\Lambda\pi^0$	0.02 ± 0.01

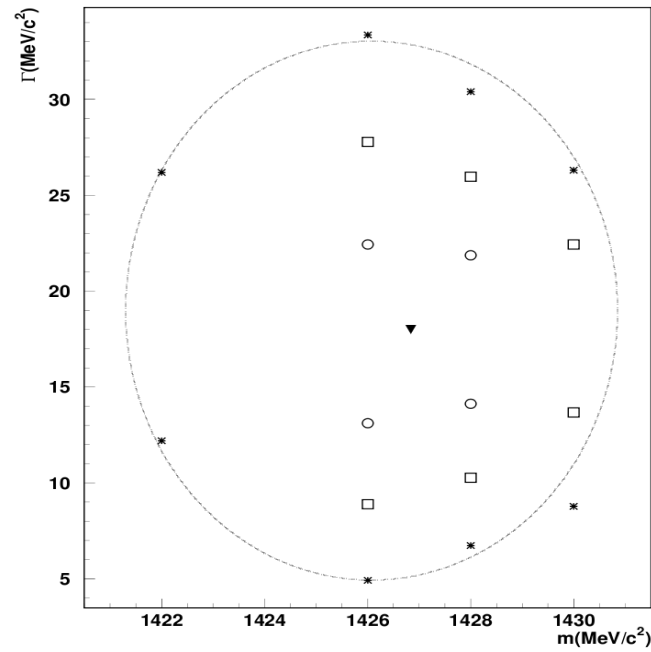


Figure 6.2: Intersection points of the $\chi^2 = \chi^2(\Gamma)$ curves with the lines: $\chi^2 = \chi_{min}^2 + 1$ circles, $\chi^2 = \chi_{min}^2 + 4$ squares, $\chi^2 = \chi_{min}^2 + 9$ asterisks. The point corresponding to χ_{min}^2 is represented as a triangle.

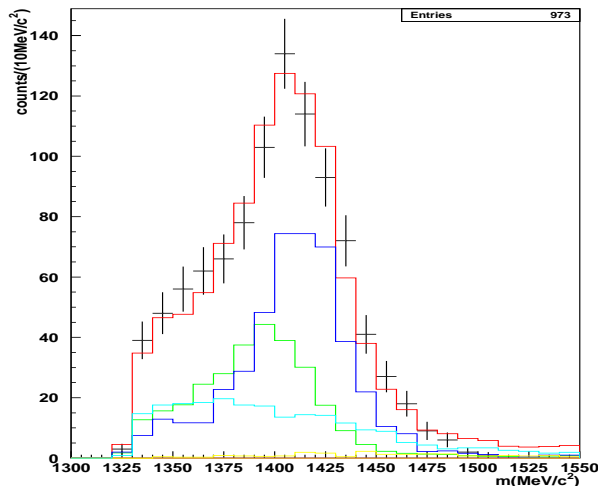


Figure 6.3: $m_{\Sigma^0\pi^0}$ fit to the DC entrance wall events with a $\Lambda(1427, 18)$. Data (black), global fit (red), $\Lambda(1427, 18)$ at rest (green), $\Lambda(1427, 18)$ in flight (blue), n. r. m. (azure) and $\Lambda\pi^0$ background (yellow).

The main difference, with respect to the $\Lambda(1405.1, 50)$ fit, consists in a good description of the high mass component generated in flight. The dominant resonant components, generated in different kinematical regimes, well reproduce the observed distribution.

In section 1.1 the emerging of two poles in the neighbourhood of the $\Lambda(1405)$ mass was described to be predicted in chiral unitary models. The following values are found [12] in a coupled-channel calculation, based on the next-to-leading order chiral $SU(3)$ meson-baryon effective Lagrangian:

$$(z_1 = 1424_{-23}^{+7} - i26_{-14}^{+3}, \quad z_2 = 1381_{-6}^{+18} - i81_{-8}^{+19}) \text{ MeV}, \quad (6.6)$$

with the higher mass pole mainly coupled to the K^-p channel. The analysis of the observed absorptions of negative kaons on bound protons in Carbon, seems to confirm the appearance of a high mass resonance pole dominating the K^-p production channel. The best fit to the data gives a mass compatible with the prediction. The narrow estimated width still have large uncertainties.

Comparing our result with the $K^-p \rightarrow \Sigma^0\pi^0\pi^0$ reaction explored in [20] with kaons in the momentum region $p_k = 514 - 750 \text{ MeV}/c$ again a similar pole position

emerges, but a narrower width respect to the $38\text{MeV}/c^2$ obtained in [21] after the non resonant $\Sigma^0\pi^0$ couples subtraction.

In [23] the Λ^* was observed, in electroproduction experiment, to exhibit a double pole structure in the $\Sigma^+\pi^-$ decay channel (mainly in the Q^2 range $1.0\text{GeV}^2 < Q^2 < 1.5\text{GeV}^2$), the best fit to the missing mass yielding the following values:

$$m_1 = 1422\text{MeV}/c^2, \Gamma_1 = 16\text{MeV}/c^2; \quad m_2 = 1393\text{MeV}/c^2, \Gamma_2 = 100\text{MeV}/c^2. \quad (6.7)$$

Our estimated mass and width parameters fairly agree with the higher mass pole (m_1, Γ_1) observed in this experiment.

6.4 Fits to events corresponding to K^- absorptions in the DC gas

The fitting procedure applied to the observed spectra for K^- absorptions in the DC gas is complicated by the contribution of K^- interactions with two different nuclei, namely Helium and Carbon, which doubles the number of components to be included in the fit. The main limit consists in the similar behaviour of the $m_{\Sigma^0\pi^0}$ spectra, for both resonant and non resonant absorptions in Carbon and Helium, as a consequence of the similar last nucleon binding energies, which renders the fit scarcely sensitive to the simulated shapes. The need to account for the Carbon contribution, and to maintain a reasonably low number of free parameters, was faced by taking advantage of the performed characterization of $K^- C$ nuclear interactions.

We decided to weight the relative contributions of $K^- He$ over $K^- C$ absorptions to the value $\frac{n_{KHe}}{n_{KC}} = 1.6 \pm 0.2$ estimated in section 5.2. For each (m, Γ) hypothesis the relative percentages of the resonant/non-resonant and at-rest/in-flight fractions, for $K^- C$ interactions, were set according to the results of the corresponding fits already performed to $K^- C$ absorptions in the wall. A first set of (m, Γ) resonances was simulated, with negative kaons absorbed in the DC inner volume according to the values given in table 6.5. A fitting algorithm was optimized which leaves the four $K^- C$ parameters to vary, within the errors, around the settled ratios. In conclusion data are fitted with the following components:

Table 6.5: Mass and width simulated values for $\Lambda(m, \Gamma)$ formation following K^- absorptions in the DC gas.

$m(MeV/c^2)$	$\Gamma(MeV/c^2)$
1390	30
1390	40
1390	100
1405	23
1405	50
1426	1
1426	15
1426	52
1430	15
1430	30

- resonant component generated by K^- absorptions in 4He at rest,
- resonant component generated by K^- absorptions in 4He in flight,
- non resonant $\Sigma^0\pi^0$ component generated by K^- absorptions in 4He at rest,
- non resonant $\Sigma^0\pi^0$ component generated by K^- absorptions in 4He in flight,
- resonant component generated by K^- absorptions in Carbon at rest,
- resonant component generated by K^- absorptions in Carbon in flight,
- non resonant $\Sigma^0\pi^0$ component generated by K^- absorptions in Carbon at rest,
- non resonant $\Sigma^0\pi^0$ component generated by K^- absorptions in Carbon in flight,
- $\Lambda\pi^0$ background.

Preliminary results from the performed fits yield a minimum $\frac{\chi^2}{ndf} = 3.0$ for the simulated resonance $\Lambda(1426, 15)$. This preliminary agreement of the fit results to the similar spectra, observed for DC wall and gas events, seems to confirm that a high mass narrow resonance produced in both in flight and at rest reactions, could be responsible for the characteristic shape of the observed distributions in $K^- C$ and $K^- He$ nuclear absorptions.

A more refined fitting scheme is presently under study, mainly concerned with a better estimate of the in-flight/at-rest ratio for $K^- C$ interactions. For consistency the ratio is presently mediated from the corresponding result for $K^- C$ absorptions in the wall, thus neglecting possible differences between K^- interactions in a solid and a gaseous target. Moreover as soon as all the Carbon target collected data will be reconstructed, the high statistics and almost purely at rest absorption spectrum, could be used to reduce the number of free parameters.

Conclusions

In this work the absorption of negative kaons on bound protons, in ${}^4\text{He}$ and ${}^{12}\text{C}$, was investigated, through an exclusive study of the $\Sigma^0\pi^0$ pairs produced in the final state. The analysis was motivated by the need of a deeper understanding of the $\Lambda(1405)$ nature and of its behaviour in nuclear environment. In this context $\bar{K}N$ is the only production channel, in which the predicted coupling with the higher mass pole of the $\Lambda(1405)$ could be evidenced. In addition, the chosen $\Sigma^0\pi^0$ decay channel, free from the dominant $\Sigma^0(1385)$ $I = 1$ background, is the most suitable for the study of the resonance lineshape.

Thanks to the good timing and energy resolutions of the KLOE detector for photon clusters, we developed a reconstruction algorithm based on time of flight and invariant mass pseudo-chi-square minimizations, achieving an efficiency of $78\pm 1\%$ in selecting and identifying the three involved photons in the reconstruction of the $\Sigma^0\pi^0$ channel.

The complex experimental condition, involving K^- nuclear absorptions on different nuclear targets (mainly ${}^4\text{He}$ and ${}^{12}\text{C}$) both at rest and in flight, was resolved by means of a careful comparative study of the relevant kinematical variables spectra, with the bubble chamber and the emulsion studies of at rest K^- interactions. The present study, supported by the simulations of K^- nuclear absorptions in the KLOE DC wall (mainly Carbon), and in the gas filling the KLOE DC (mainly Helium), lead to the comprehension of the different processes giving rise to the observed spectra. The characteristic shapes of the $p_{\Sigma^0\pi^0}$ and T_{π^0} spectra for K^- absorptions at rest, also compared with the $\theta_{\Sigma^0\pi^0}$ angular correlation, allowed, for the first time, to identify an in flight contribution to the $m_{\Sigma^0\pi^0}$ spectrum. The in flight absorptions give rise to $m_{\Sigma^0\pi^0}$ components lying above the kinematical mass limits for processes at rest, contributing for $\left.\frac{n_{>m_{lim}}}{n_{<m_{lim}}}\right|_C = 0.53 \pm 0.04$ and

$\left. \frac{n_{>m_{lim}}}{n_{<m_{lim}}} \right|_{He} = 0.82 \pm 0.06$ respectively in Carbon and in the DC gas.

This study motivated the realization of a dedicated high purity Carbon (graphite) target in summer 2012 (installed inside the KLOE DC, between the beam pipe and the DC entrance wall) an integrated luminosity of $\sim 100 pb^{-1}$ was collected in the period (6 November - 14 December) 2012. A preliminary analysis, performed on a sample of $8 pb^{-1}$ reconstructed data, confirms our interpretation.

The $\Lambda\pi^0$ background, from direct and internal conversion production mechanisms, was estimated to account for $(3 \pm 1)\%$ and $(3 \pm 2)\%$ of the final selected sample in the wall and the DC gas respectively.

A multi-component fit was performed to the $m_{\Sigma^0\pi^0}$ distributions, taking into account for both resonant and non-resonant $\Sigma^0\pi^0$ production in at rest and in flight reactions. The contributions of the $\Lambda\pi^0$ background and the non-resonant $\Sigma^0\pi^0$ background from photons misidentification, were included in the fit. The best fit, for events in Carbon, was obtained for a resonant component $m = 1427_{-6}^{+4} MeV/c^2$ $\Gamma = 18_{-13}^{+15} MeV/c^2$.

The search for charged extra-tracks from the hadronic interaction point, inside the DC volume, leads to the identification of a small sample of $K^{-4}He \rightarrow \Sigma^0\pi^0 {}^3H$ events at rest. The $m_{\Sigma^0\pi^0}$ and $p_{\Sigma^0\pi^0}$ spectra for these events agrees with the results outlined in this work. Moreover, we shown the concrete chance of a higher resolution missing mass study, employing the measured momentum of the identified triton, in the future higher statistic data campaigns.

Acknowledgements

Thanks to my tutors Dott.ssa Catalina Curceanu and Prof. Filippo Ceradini, for having been by my side everytime I needed it.

Thanks to Oton Vazquez Doce, my mentor, for patiently introducing me in the word of experimental physics.

A very special thought for Paul Kienle, who recently left us. He was constantly helping me, with many important suggestions and great ideas, till the very last days of his life. I will always remember you Paul! Rest in peace - your legacy will stay with us!

Bibliography

- [1] R. H. Dalitz, S. F. Tuan, Phys.Rev. Lett. 2 (1959) 425.
- [2] R. H. Dalitz, S. F. Tuan, Ann. Phys. 10 (1960) 307.
- [3] M. H. Alston *et al.* Phys.Rev. Lett. 6 (1961) 698.
- [4] J. Beringer et al. (Particle Data Group), Phys. Rev. D86, 010001 (2012)
- [5] R. H. Dalitz, T. C. Wong, G. Rajasekaran, Phys.Rev. 153 (1967) 1617.
- [6] N. Kaiser, B. P. Siegel, W. Weise, Nuclear Phys A594 (1995) 325.
- [7] E. Oset, A. Ramos, Nuclear Phys. A635, (1998) 99.
- [8] J. A. Oller, U. G. Meissner, Phys. Lett. B500, (2001) 263.
- [9] T. Hyodo, D. Jido, Prog. Part. Nucl. Phys. 67 (2012) 55.
- [10] J. A. Oller, E. Oset, A. Ramos Prog. Part. Nucl. Phys. 45 (2000) 157.
- [11] J. C. Nacher, E. Oset, H. Toki, A. Ramos, Phys. Lett. B455 (1999) 55.
- [12] Y. Ikeda, T. Hyodo, W. Weise, Nucl. Phys. A881, (2012) 98.
- [13] M. niyama et al., Phys. Rev. C78, (2008) 035202.
- [14] Y. Akaishi, T. Yamazaki, Phys. Rev. C65, (2002) 044005.
- [15] R. J. Hemingway, Nuclear Phys. B253, (1985) 742.
- [16] R. H. Dalitz, A. Deloff, J. Phys. G17 (1991) 289.
- [17] D. Riley et al., Phys. Rev. D11 (1975) 3065.

-
- [18] J. Esmaili, Y. Akaishi, T. Yamazaki, Phys. Lett. B686 (2010) 23.
- [19] I. Zychor et al., Phys. Lett. B660, (2008) 167.
- [20] S. Prakhov et al., Phys.Rev. C70 (2004) 034605
- [21] V. K. Magas, E. Oset, A. Ramos, Phys.Rev. Lett. 95 (2005) 052301
- [22] K. Moriya, R. Schumacher, and CLAS Collaboration, AIP Conf. Proc. (2012) 1441, 296.
- [23] H. Lu, R. Schumacher, B. Raue, M. Gabrielyan, and CLAS Collaboration, AIP Conf. Proc. 1432, (2012) 199.
- [24] J. Siebenson, L. Fabbietti, A. Schumach, E. Apple, PoS Bormio2010 (2010) 052.
- [25] AMADEUS Letter of Intent, http://www.lnf.infn.it/esperimenti/siddharta/LOI_AMADEUS_
- [26] H. Noumi, J-PARC proposal E31, http://j-parc/NuclPart/Proposal_e_.html
- [27] L. R. Staronski, S. Wycech, Nucl. Phys. 13 (1987) 1361.
- [28] G. Backenstoss, G. Egger, Nucl. Phys. B73, (1974) 189.
- [29] D. F. Keane, Thesis University College Belfield, Dublin (1981).
- [30] P. J. Carlson, O. Danielsson, A. G. Ekspong, A. Frisk, Nuclear Phys. 74 (1965) 642.
- [31] R. K. Adair, Phys. Lett. 6, (1963) 86.
- [32] A. Barbaro-Galtieri, F. M. Smith, J. W. Pareick, Phys. Lett. A Vol. 5, No. 1 (1963), 63.
- [33] P. A. Katz et al., Phys.Rev. D1 (1970) 1267.
- [34] K. Brunnel et al., Phys.Rev. D2 (1970) 98.
- [35] R. Baldini et al., Proposal for a Phi-Factory, report LNF-90/031(R) (1990).
- [36] M. Adinolfi et al., [KLOE Collaboration], Nucl. Inst. Meth. A 488, (2002) 51.

-
- [37] M. Adinolfi et al. [KLOE Collaboration], Nucl. Inst. Meth. A 482, (2002) 368.
 - [38] M. Anelli et al. Nucl. Inst. Meth. A 581, (2007) 368.
 - [39] A. Aloisio et al. [KLOE Collaboration], Nucl. Inst. Meth. A 492, (2002) 134.
 - [40] F. Ambrosino et al. [KLOE Collaboration], Nucl. Inst. Meth. A 534, (2004) 403.
 - [41] T. Kobayashi et al., Nuclear Physics A 805 (2008) 431c.
 - [42] C. Vander Velde-Wilquet et al., Nuovo Cimento 39 A, (1977) 538.
 - [43] A. Deloff et al., Phys.Rev. C (1974) 1688.
 - [44] C. Garcia-Recio et al., arXiv:nucl-th/0210030v2 21 Feb 2003.
 - [45] C. Vander Velde-Wilquet et al., Nuovo Cimento, Lett. 5, (1972) 1099.
 - [46] E. Hiyama et al., Prog. Part. Nucl. Phys. 63 (2009) 339.